Numerical Algorithms for Light Transport in Layered Turbid Media and Other Special Mathematical Functions

by

Michael C. Helton

A dissertation submitted in partial fulfillment
of the requirements for the degree of
Doctor of Philosophy
(Applied Physics)
in the University of Michigan
2023

Doctoral Committee:

Professor Mary-Ann Mycek, Chair
Professor Stephen Rand
Professor Karthik Vishwanath
Professor Kevin Ward

Michael C. Helton
heltonmc@umich.edu
ORCID iD: 0000-0002-3881-9973

ACKNOWLEDGMENTS

I want to begin by thanking my advisor, Dr. Mary-Ann Mycek. During your undergraduate career, it is almost expected that you change majors every year until you run out of time - at least I changed three times before settling on Physics. In graduate school, there is a somewhat stronger expectation that you have narrowed your interest down to spend many years studying a fairly narrow problem. At this point, I'm convinced that I changed my mind over the past six years more than I did in the previous four. Some of those were due to external circumstances while some were natural progressions that came from trying new things. The difficulty during graduate school is finding the balance between chasing down every interest and side project while pushing forward an overall dissertation of scholarly work. Mary-Ann was always there to encourage and support my changing passions at each step and was instrumental in pushing me towards becoming the researcher I am today.

I had read a paper early in my graduate career and was for some reason fascinated with the "time-domain" approach but would require additional hardware we didn't have in the lab. I'll never forget the rather flippant conversation I had with Dr. Karthik Vishwanath over four years ago who casually mentioned that he had just acquired a laser that we could probably take measurements with. This sparked a long collaboration and I am forever thankful for that opportunity and the time he provided in teaching me about computational modeling, experimental systems, and listening to all my crazy ideas while pushing me to pursue the best ones.

I would also like to thank members of my dissertation committee Dr. Stephen Rand who provided helpful feedback and discussion during the proposal and defense even during retirement. I would also like to thank Dr. Kevin Ward who gave me valuable insights into clinical translation, loaning me any equipment in his lab, and providing me the opportunity to gain experience in pre-clinical studies. I would also like to thank Dr. Alisha B. Diggs for her mentorship and friendship over the last five years. Those lengthy discussions over lunch got me through the long middle years of the PhD. I'd also like to thank Samantha Zerafa who contributed greatly to the following work and I will always strive to be as organized and on top of things as her. Additionally, I'd like to thank both Maeve Willen and Jimmy Young who provided truly excellent insight in our daily discussions and made working from home a bit more enjoyable. All of Sam, Jimmy, and Maeve have heard me ramble too long over video chat and I am thankful for them putting up with me during our remote

days. I would also like to thank the many students that I have worked with in both Dr. Mycek's and Dr. Vishwanath's labs: Didem Temeltas, Xiwen Wei, Julia Pakela, Suraj Rajesekhar, Carter McMaster, Vinoin Devpaul Vincely, and Mainul Sabbir. Additionally, I would like to thank the Julia language community who answered all my beginner questions about programming. I want to particularly acknowledge Oscar Smith who gave an enormous amount of time and effort teaching me about computer mathematical optimizations and reviewing a significant amount of code.

Finally, I would like to thank my parents for helping and supporting me throughout my graduate studies.... and the many years before that.

TABLE OF CONTENTS

LIST OF FIGURES

FIGURE

LIST OF TABLES

TABLE

LIST OF APPENDICES

LIST OF ACRONYMS

MC Monte Carlo

RTE Radiative Transport Equation

NIR Near-infrared

DOS Diffuse optical spectroscopy

SDS source-detector separation

DTOF distributions of times-of-flight

TRS Time-resolved reflectance spectroscopy

TCSPC time-correlated single photon counting

IRF instrument response function

ABSTRACT

The study of light transport is important in many applications ranging from neutron transport, gas and plasma dynamics, Brownian motion, and photon transport in biological tissues. In medicine, light can be used to investigate tissue physiology up to several centimeters below the surface without the use of harmful radiation. For example, by spectrally resolving the amount of absorbed near-infrared light, concentrations of both oxygenated and deoxygenated hemoglobin can be derived to measure tissue oxygen saturation and blood volume. On the other hand, measuring the dynamic fluctuations of scattered light from circulating red blood cells can be used to quantify the speed of blood flow. All of these techniques require an appropriate description of light transport through biological tissue that can successfully model the forward transport of light. Even more importantly, these models must also be used in inverse models to estimate probed tissue parameters from measured optical signals. Therefore, the successful translation of light based technologies to clinical medicine depend on appropriate physical forward and inverse models that can best describe the underlying tissue structure and experimental system. Because these models are often implemented in computer programs, the accuracy and performance of the translation of these models to numerical algorithms are vital.

This dissertation focuses on the intersection of the mathematical theory of light transport and subsequent numerical implementations. An important application of tissue optics is in the study of brain hemodynamics which is limited by the penetration depth of optical signals and the confounding effects of superficial tissue. The use of time-resolved measurements can improve depth sensitivity by selecting for later arriving photons that have a higher probability of probing deeper tissues. The first half of this thesis focuses on developing a time-resolved system and subsequent data analysis procedure for fast analysis of reflectance measurements. An approach using Monte Carlo lookup tables for rapid quantitation of the reduced scattering coefficient within 6-25 % of baseline values was developed. The approach has the advantage of being independent of the instrument's temporal dispersions while avoiding slower iterative data processing. This approach was further improved to include recovery of the absorption and reduced scattering coefficient within 5-15 % that combined the lookup table approach with diffusion based curve fitting. These approaches help reduce the recovered error in optical properties from over 40 % to less than 15 % when considering uncertainties in the measurement's time scale.

On the other hand, improved sensitivity to brain tissue can be achieved through more robust data analysis methods. Particular focus is given to studying layered turbid media as a higher order approximation to brain tissue. Efficient numerical approaches to solve both the photon diffusion equation and correlation diffusion equation in layered media are given in the steady-state, frequency domain, and time-domain. The developed algorithm was able to simulate the steady-state and time-domain fluence in less than 50 and 500 microseconds which is 3-4 orders of magnitude faster than current approaches allowing for real-time (< 1 Hz) data processing in both domains. Solutions and numerical algorithms were also developed to solve the correlation diffusion equation for real-time data analysis of blood flow measurements in both the steady-state and time-domain. Inverse procedures were also developed to recover flow coefficients within 5 % of baseline numerical values when using layered diffusion theory. For both the photon and correlation diffusion equation, successful validation against Monte Carlo measurements in simulated brain tissue was also shown indicating the promise of the described approaches to improve optical brain monitoring. The presented numerical algorithms and code are publicly available for the work describing diffuse optics (https://github.com/heltonmc/LightPropagation.jl), Bessel and other special mathematical functions (https://github.com/JuliaMath/Bessels.jl), and inverse Laplace transforms (https://github.com/heltonmc/Laplace.jl).

CHAPTER 1

Introduction

1.1 Overview

This thesis focuses on the study of light diffusion in biological tissue as it relates to medical diagnostics [167]. Much of the discussion is also applicable to other media of high scattering such as paints [41], clouds [77], pharmaceuticals [155], plastics [178], and food [118]. Although there exists several ways to model light transport [191, 82, 23, 1], the two most popular approaches are considered: (1) numerical methods to solve the Radiative Transport Equation (RTE) using Monte Carlo (MC) simulations [191] and (2) analytical approximations to the RTE using diffusion theory [137]. Transport theory considers a larger class of problems concerning the general transport of particles (e.g. neutrons, electrons, photons) through some background medium [22, 23, 1]. These problems have many application areas in atmospheric [162, 93, 24] and nuclear physics [26, 88], however, much of the discussion will focus on the utility of the diffusion approximation in biological media [64].

1.2 Diffuse Optical Spectroscopy

Diffuse optical spectroscopy (DOS) is a noninvasive technique to measure optical properties (i.e., scattering and absorption) of multiply scattered light which can be used to assess pathological and physiological conditions of biological tissue [53]. Near-infrared (NIR) light is most commonly used because of the relatively low background absorption of water providing better contrast to other light absorbers such as oxygenated hemoglobin ($\mathrm{HbO_2}$) and deoxygenated hemoglobin (Hb) [48, 149, 159]. Biological tissue is composed of many chromophores with distinct absorption spectra allowing for separation and quantitation of their respective concentrations. In the NIR window, the primary absorbers of light are hemoglobin, melanin, water, and lipids, however, biological tissue also strongly scatters light which dictates light propagation [80].

Chromophores are the tissue components that absorb light through either electronic or vibrational transitions while scattering is determined by the size and morphology of biological cells [5]. At small incident angles, light scattering is predominately caused by a change in the cell's index of refraction whereas the cell's nuclei are more responsible at larger incident angles [127, 126, 128]. Mie theory is a rigorous way to model light scattering in a distribution of spherical objects of varying sizes from an incident planar electromagnetic wave considering the inter particle space, scattering angle, refractive index, and spherical diameter [16, 121]. However, considering all these properties in light that has travelled several centimeters and interacted with many thousands of cells is impractical due to the limited knowledge about the underlying tissue. Therefore, it is expedient to consider the macroscopic properties of biological tissue by modelling it as a bulk material of many different types of cells and tissues [80]. A weighted sum of the contribution of each chromophore is used to quantify the bulk absorption coefficient (μ_a) of the probed medium. Likewise, the reduced scattering coefficient (μ_s'), which is typically $100\times$ larger than μ_a, represents a photon random walk with a step length of $1/\mu_s'$ where each step corresponds to an isotropic scattering event. The distinction between the reduced version μ_s' and the regular scattering coefficient, $\mu_s' = (1-g)\mu_s$, is due to the strong forward scattering nature of biological tissue ($g \geq 0.9$) where each step length only results in a small angular deflection. The anisotropy g represents the amount of forward direction retained after a single scattering event quantified by the averaged cosine angle $g =< \cos(\theta) >$ where $g = 0$ represents isotropic scattering and $g = 1$ represents total forward scattering.

Light propagation in turbid media such as biological tissue is typically described by the RTE which is a complex integro-differential equation [109]. Since much of this thesis is focused on the compromises between analysis methods, it is important to mention that the RTE is a phenomenological and heuristic theory that does not have a rigorous mathematical formulation to account for all the physical effects of light transport. The multiple scattering theory that start from Maxwell's equations can mathematically account for the effects of multiple scattering, diffraction, and interference but is not practical due to its complexity. However, under some assumptions the RTE can be derived from the more rigorous electromagnetic theory in discrete random media [109]. Therefore, the RTE is typically solved numerically using the MC method.

The Monte Carlo method provides a robust physical simulation of light propagation and can solve the RTE to any desired accuracy even when considering irregular boundary conditions and heterogeneous media [50]. The general procedure traces the random walk steps of energy packets (i.e., the trajectory of simulated photons) by sampling probability functions that govern light transport. This stochastic process requires tracing tens to hundreds of millions of photons where the standard error decreases proportionally to the inverse square root of the number of detected photons given by the central limit theorem [191]. Therefore, the MC method has several advan-

tages and disadvantages. The ability to solve the RTE in any domain (e.g., low scattering, high absorption) for complex heterogeneous media allows for its use in many areas of biophotonics. However, it requires enormous computational resources that inhibit its use for fast (< 1 Hz) data processing.

On the other hand, the RTE can be solved analytically under certain boundary conditions to give direct expressions to compute. Direct analytical solutions to the RTE have received recent attention but are difficult to express in closed form in different domains and geometries [105]. The diffusion approximation to the RTE is most commonly used as there are analytical solutions available in several geometries which are easily translated to computer code that can be solved quickly for fast data analysis [137, 85]. The compromise is that diffusion theory is limited to simple geometries with homogeneous optical properties and the assumptions of diffuse light (e.g., $\mu_s' >> \mu_a$).

1.3 Technical challenges

The problem can be reduced to estimating the optical properties μ_a and μ_s' from measured light intensities at multiple wavelengths. The properties can be used to estimate concentrations of varying chromophores using known extinction spectra to give more clinically relevant information such as the percent of oxygen saturation of underlying tissue [80]. This is usually not as simple because the effects of absorption must be uncoupled from scattering changes while making several assumptions and approximations about the underlying tissue geometry and composition. Much of this thesis is focused on the compromise between a representable and accurate physical model of light transport and the necessity to estimate important metrics quickly to be used in a clinical setting.

Spectroscopy and imaging require an understanding of the interaction between probed media and external stimuli. In most cases, we are interested in the behavior of the injected light after it has traveled some distance inside the medium before being detected. Our objective is to develop a forward model that can estimate the response of a tissue to a known optical source. Once a forward model is developed, it can be used along with experimental measurements to quantify properties of the medium. This process is known as the inverse problem where we seek parameters of the forward model that best fit measured data.

Both the inverse and forward problem present their own challenges but typically any inverse method requires evaluation of the forward model hundreds to thousands of times for different parameters. At the same time, any useful analysis method needs to be able to deliver accurate information in a timely matter. For example, brain oxygenation monitoring during surgery or in emergency care requires rapid estimates of tissue properties (> 1 Hz). The recent advances in computer hardware have made MC methods more popular which are amenable to parallel com-

puting - meaning that each trace is independent and can be simultaneously computed on different cores of a either a central processing unit (CPU) or graphics processing unit (GPU). The continued yearly technology increase in the number of cores and the ability to link multiple GPU units have provided enormous improvements in MC efficiency scaling almost linearly with the number of cores [50].

The advantage of MC over diffusion based analytical solutions is its flexibility and accuracy. Monte Carlo can be used with complex meshes to model capillary networks and the folds of brain tissue while being a solution to the RTE [187]. In other words, MC does not require that light be diffuse and can be used more generally whenever the RTE is valid. Analytical solutions often require simple boundaries, homogeneous properties, and are less accurate as they are limited by the diffusion approximation (e.g., high scattering, low absorption, far from source). However, analytical solutions are easy to set up, orders of magnitude faster, and amendable to inverse optimization. For example, state of the art MC simulations take on the order of several seconds on expensive GPUs while a solution to the diffusion equation in a homogeneous medium can be simulated on a laptop in tens of nanoseconds [183]. This is highly advantageous when quantitative data needs to be provided to clinicians every half second while having to evaluate forward models hundreds to thousands of times.

Of course, technology will continue to improve and scale where in the future MC may be able to to solve inverse problems in real-time. Approaches that leverage the continued improvement in computation power (Moore's law) are typically most effective but an important consideration is that medical systems may need to be embedded, portable, low cost, compact, robust and/or run on batteries. Ideally, the system could also not keep someone warm during a Michigan winter. The central question and main motivation in this work prods the compromise between physical accuracy and speed as it relates to studying brain hemodynamics. How can we produce accurate results while being efficient?

One of the most promising application areas for diffuse optics is monitoring the brain. The non-invasive nature of light technologies allow for continuous monitoring in a safe and practical way. Over 30 years ago, diffusion theory was shown to adequately describe light transport in biological media, providing a theoretical framework to quickly and easily quantify biological tissue [137]. Although some improvements to the boundary conditions have been made [85], that simple model which approximated biological tissue as optically homogeneous and semi-infinite is still one of the most popular methods today due to its ease of use and computational efficiency [62]. However, it has been consistently shown that the semi-infinite approximation is particularly prone to superficial contamination [133, 153]. In some applications, such as brain monitoring, the underlying tissue is not optically homogeneous causing a breakdown in the forward model's assumptions. This is exacerbated when we are more interested in deeper tissues such as the brain compared to

the superficial layers (scalp) [146].

This problem has been tackled both theoretically and experimentally. By using time-domain measurements it is possible to separate the detected photons by their arrival times [163]. Therefore, the photons that arrive later are more likely to have travelled in deeper brain tissues [186]. This allows for selection and separation of early and late arriving photons making analysis more sensitive to deeper tissues [38]. This approach is limited by more expensive hardware, more complex data analysis, limited dynamic range in experimental system, and longer data acquisition times [186]. Additionally, even late arriving photons have to travel through superficial layers twice which can significantly affect the detected light signal.

Alternatively, the forward model can consider a slightly less crude approximation where instead of optically homogeneous, the underlying tissue is modeled as a stack of finite thick media with their own optical properties [86, 84, 102]. This method has become increasingly attractive as it has been shown to match MC simulations in complex brain meshes taken from magnetic resonance imaging (MRI) data [153]. Several approaches to solve the diffusion equation in layered planar media have been presented [112, 86, 104] which increase both the complexity of the forward and inverse problems. The forward problem is now significantly more expensive taking roughly one second to compute a time-domain signal for different combinations of optical properties [59]. For reference, the time-domain signal in a semi-infinite medium can be computed in tens to hundreds of nanoseconds. The increase in computational time is due to the necessity to compute the time-domain signal (and even the steady-state signal) using numerical transforms from different domains [75]. This can also introduce numerical errors and limitations during integration of exponentially increasing terms within the integrand.

On the other hand, considering a more complicated tissue geometry increases the complexity of the inverse problem significantly. An advantage of homogeneous models in addition to the simpler and faster forward problem is that inverse optimization usually considers one or two parameters (a single μ_a and μ_s'). This has made analysis using more expensive forward solvers such as MC possible as precomputed lookup tables can be generated and stored to quickly estimate optical properties [72]. However, in more complicated geometries such as brain tissue, it may be required to consider many more parameters in the forward problem as unknown (i.e., must consider different absorption, scattering, and thickness of many layers). Recovering multiple parameters in a large scale inverse problem is one of the more computationally demanding problems in numerical computing [156]. Full and even partial lookup based approaches typically used in MC for homogeneous models are impractical from a memory perspective. In the 2D case, the entire lookup table can be stored in computer memory and each value in the problem space can be sampled in a reasonable amount of time. For larger scale parameter estimation, it becomes difficult to store a reasonably sized discrete parameter space without compromising on accuracy while not being able to iterate

quickly through every value. For example, it takes over a second to sum a $700 \times 700 \times 700$ matrix while requiring almost 5.5 GB of memory. Therefore, all of these considerations make using either MC based lookup approaches or existing layered solution unfeasible for real-time analysis limiting most of the advantages of diffusion based models over MC methods.

1.4 Objectives

The first half of this thesis investigates the experimental approach for better sensitivity to deeper absorption changes by developing and validating a time-domain optical spectroscopy system. The second half focuses on developing a forward model for layered tissues. Both of these problems have been previously studied, however, my pursuit was guided by a few overarching themes. First, I wanted to pay careful attention to the implementation and translation of these analysis methods to computer code. Therefore, the analysis methods should be easy to use, fast, correct, and well-tested. Of course, these can never be 100% verified but all code is freely available with extensive documentation online (https://github.com/heltonmc) and each algorithm is well tested with a suite of continuous integration tests to ensure that any future modification retains at least somewhat the desired functionally. All the programs are written in the Julia programming language [11]. At a minimum, the language was chosen because it is open-source, easy to write high performance code, the ability to fix bugs in the future without a license, and personal enjoyment.

The Chapters can be summarized by the following aims.

- **Aim 1:** Build and validate a time-domain diffuse optical spectroscopy system to quantify optical properties from reflectance measurements.
- **Aim 2:** Develop novel data analysis methods for analyzing time-resolved optical data considering uncertainties in measured data from the system's instrument response function.
- **Aim 3:** Develop a sufficiently fast data analysis scheme that can be used to analyze biological tissue's optical properties in complex media such as the brain in real-time.
- **Aim 4:** Extend layered analysis method to the correlation diffusion equation to quantify depth dependent blood flow rates.

The pursuit of these aims has led to many other scientific contributions outside of diffuse optics. For example, Aim 3 led to the development of a faster approach to compute the Bessel function of the first kind and zero order. This work was continued to compute the more general case of arbitrary order for Bessel and Modified Bessel functions of the first and second kind. Routines to compute other special mathematical functions such as the Spherical

Bessel functions, Hankel functions, Airy functions, and Struve functions were also developed and openly available at https://github.com/JuliaMath/Bessels.jl. Additionally, different numerical techniques to perform the inverse Laplace transform were investigated and are available at https://github.com/heltonmc/Laplace.jl. Therefore, this work led to the following aim.

- **Aim 5:** Develop fast and accurate computer algorithms for the computation of several special mathematical functions common in physics.

The main body of the dissertation will focus on the first four aims.

1.5 Thesis Organization

The thesis is organized in two halves with Chapters 2 and 3 discussing novel analysis methods and experimental results using time-resolved reflectance measurements in homogeneous media. In **Chapter 2**, we introduce time-resolved DOS and introduce novel analysis procedures for estimating the reduced scattering coefficient (μ_s') from reflectance measurements in turbid media. This is a reprint of the published article "Direct estimation of the reduced scattering coefficient from experimentally measured time-resolved reflectance via Monte Carlo based lookup tables" [70]. In **Chapter 3**, we expand on the analysis methods introduced in Chapter 2 using the standard diffusion approximation while discussing the uncertainties related to the time axis of the instrument response function. This is a reprint of the published article "Reconstruction of optical coefficients in turbid media using time-resolved reflectance and calibration-free instrument response functions" [72].

The last half of the thesis, Chapters 4 and 5, is focused on light diffusion in planar layered media. In **Chapter 4**, efficient methods for computation of light diffusion in the steady-state, frequency-domain, and time-domain are developed. This Chapter is a reprint and reorganization of the published article "Efficient computation of the steady-state and time-domain solutions of the photon diffusion equation in layered turbid media" [75]. Additional comments and expanded discussion in some areas have been added that differ from the published article. **Chapter 5** extends these computational models to solve the correlation diffusion equation in layered media in both the continuous-wave and time-domains. The model is also used in inverse problems to demonstrate the ability to quantify data in real-time. This is a reprint of the published article "A numerical approach to quantify depth-dependent blood flow changes in real-time using the diffusion equation with continuous-wave and time-domain diffuse correlation spectroscopy" [74]. A brief summary of the dissertation and prospective on future work is provided in **Chapter 6** along with a list of scientific contributions.

CHAPTER 2

Direct Estimation of the Reduced Scattering Coefficient from Experimentally Measured Time-Resolved Reflectance via Monte Carlo Based Lookup Tables

This chapter was published in [70]. It introduces time-domain diffuse optical spectroscopy and analysis methods for quantitation of the reduced scattering coefficient from Monte Carlo generated lookup tables. The chapter was prepared in collaboration with Dr. Karthik Vishwanath and Dr. Mary-Ann Mycek.

2.1 Abstract

A heuristic method for estimating the reduced scattering coefficient (μ_s') of turbid media using time-resolved reflectance is presented. The technique requires measurements of the distributions of times-of-flight (DTOF) of photons arriving at two identical detection channels placed at unique distances relative to a source. Measured temporal shifts in DTOF peak intensities at the two channels were used to estimate μ_s' of the medium using Monte Carlo (MC) simulation-based lookup tables. MC simulations were used to compute temporal shifts in modeled reflectance at experimentally employed source-detector separation (SDS) for media spanning a wide range of optical properties to construct look up tables. Experiments in Intralipid (IL) phantoms demonstrated that we could retrieve μ_s' with errors ranging between 6-25 % of expected (literature) values, using reflectance measured across 650-800 nm and SDS of 5-15 mm. Advantages of the technique include direct processing of measured data without requiring iterative non-linear curve fitting. We also discuss applicability of this approach for media with low scattering coefficients where the commonly employed diffusion theory analysis could be inaccurate, with practical recommendations for use.

2.2 Introduction

Time-resolved reflectance spectroscopy (TRS) has the potential to directly provide bulk scattering and absorbing coefficients of a turbid medium without making assumptions about the medium's composition or structure [36, 141, 2, 163]. In TRS, picosecond laser pulses (fired at MHz rates) are injected into a turbid medium and the multiply scattered and attenuated diffusely reflected pulses are detected using a fast single photon counting photodiodes that are usually coupled to time-correlated single photon counting (TCSPC) boards to measure the photon distributions of times-of-flight (DTOF) [163]. These measurements are then quantified using theoretical (or numerical) approaches to extract the absorption (μ_a) and reduced scattering (μ_s') coefficients of the medium [141, 2, 163, 140]. In biological media, accurately and efficiently recovering the optical transport coefficients can help parametrize a variety of functional and structural properties of biomedical and clinical interest [181, 25].

Uncoupling μ_a and μ_s' using experimentally measured DTOF is known to be a difficult problem that needs careful measurements and calibrations [36, 141, 2, 163, 140, 122, 142, 132]. The measured DTOF is a convolved response of the theoretical temporal point spread function (TPSF) and the instrument response function (IRF) of the experimental system [182]. The TPSF represents the (Green's function) response of the tissue medium to an incident Dirac delta pulse, while the IRF represents the finite temporal profile of the incident laser pulse measured as it propagates through the detection optics [182]. Extraction of the optical properties is typically done by iteratively convolving a theoretical TPSF with the experimentally measured IRF and fitting the convolved response via non-linear least squares to the measured DTOF [122, 174, 114]. Since the theoretical TPSF is computed from known optical properties, the process yields optical properties for the medium at convergence.

The above approach requires both having appropriate theoretical estimates to accurately model the TPSF, and accurate estimates of the system IRF. Since the IRF is a function of the laser source, fiber optics, and detection electronics used to deliver and collect signals, the IRF must be measured for all detection channels and wavelengths used experimentally [150, 131]. Curve fitting of the DTOF using diffusion theory (DT) is usually the most common method for extracting optical properties of turbid media using TRS [62]. Although the process requires iterative reconvolution based reconstructions and are usually performed off-line, growth of computational resources could render these methods to operate in real-time [62]. However, applications of such models to analyze biological tissues have shown large variance in extracted coefficients [36, 141, 2, 131, 35] particularly in scattering as reported recently [125]. Inverse methods using DT can also be computationally intensive and have been reported to show crosstalk between the derived optical coefficients [36, 2, 142, 132]. Thus, a method such as the one we have presented could potentially facilitate

improved fitting with DT.

Limiting crosstalk between recovered coefficients is critical for accurate estimation of optical properties, which in turn impact clinical and diagnostic utility of these methods. Different approaches have been described to constrain inverse fitting algorithms and increase quantitative accuracy of recovered optical parameters [33, 94, 46]. For example, measurements at multiple wavelengths were used to constrain spectral properties of the medium in order to improve the accuracy of recovered parameters [46]. Thus, methods that can extract (or even constrain) the optical coefficients of the medium can help DT based models in estimation of optical properties.

Here, we present a simple-to-use, heuristic technique that facilitates estimation of the μ_s' of a medium directly from experimentally measured DTOFs. This method uses lookup tables constructed using MC simulations and translates measured peak-to-peak time differences (Δt) in DTOF obtained at two distinct SDS into μ_s' of the medium. We describe implementation of the method and demonstrate its application to experimental data obtained from well-described tissue simulating phantoms [114, 120, 157].

2.3 Materials and Methods

2.3.1 Instrumentation

Figure 2.1(a) shows the schematic of the experimental system, where the input pulse from a supercontinuum laser (SC400, NKT Photonics, DK) was spectrally filtered via a band-pass filter (SuperK VARIA, NKT Photonics, Denmark) and coupled into one end of an optical (source) fiber (diameter = 400 μm; NA=0.22; length=1 m). The distal end of the source fiber illuminated a medium of interest and formed the sensing head of a custom-fabricated optical probe (Gulf Photonics, FL). The sensing head had three detection channels (made from three optical fibers identical to the source fiber) which were epoxied at distances of 5, 10, and 15 mm from the source fiber – thus, our sensing probe had a fixed geometry. Reflectance measured from a selected channel (identified uniquely using the SDS) was coupled into a single-photon avalanche diode (SPAD) detector (PMD-050, MPD, Italy), that was electronically coupled to a time-correlated single photon counting (TCSPC) board (SPC-130, Becker & Hickl, Germany). The laser repetition rate was 40 MHz and an electronic sync signal from the laser was used to trigger the TCSPC for signal acquisition.

Figure 2.1(b) shows representative time-resolved reflectance measurements at the three experimental SDS used. Figure 2.1(c) shows a magnified view of the DTOF peaks. The IRF was measured to ensure equality for each channel across all wavelengths by reflecting the source pulse into the detecting fiber using a mirror with a white piece of paper placed over the detecting fiber. Figure 2.1(d) shows the IRF measured at 650 nm for all three detector channels used. The average

root mean square error (RMSE) calculated over three orders of magnitude for all IRFs measured across all channels and wavelengths used was 0.008. For comparison, repeated scans from a fixed target surface had RMSE of nearly 0.001, while DTOFs at differing absorption and scattering coefficients produce RMSE values larger than 0.1. Temporal stability of the peak position was also monitored over several hours of continuous acquisition and was shown to vary less than 0.7 % per hour.

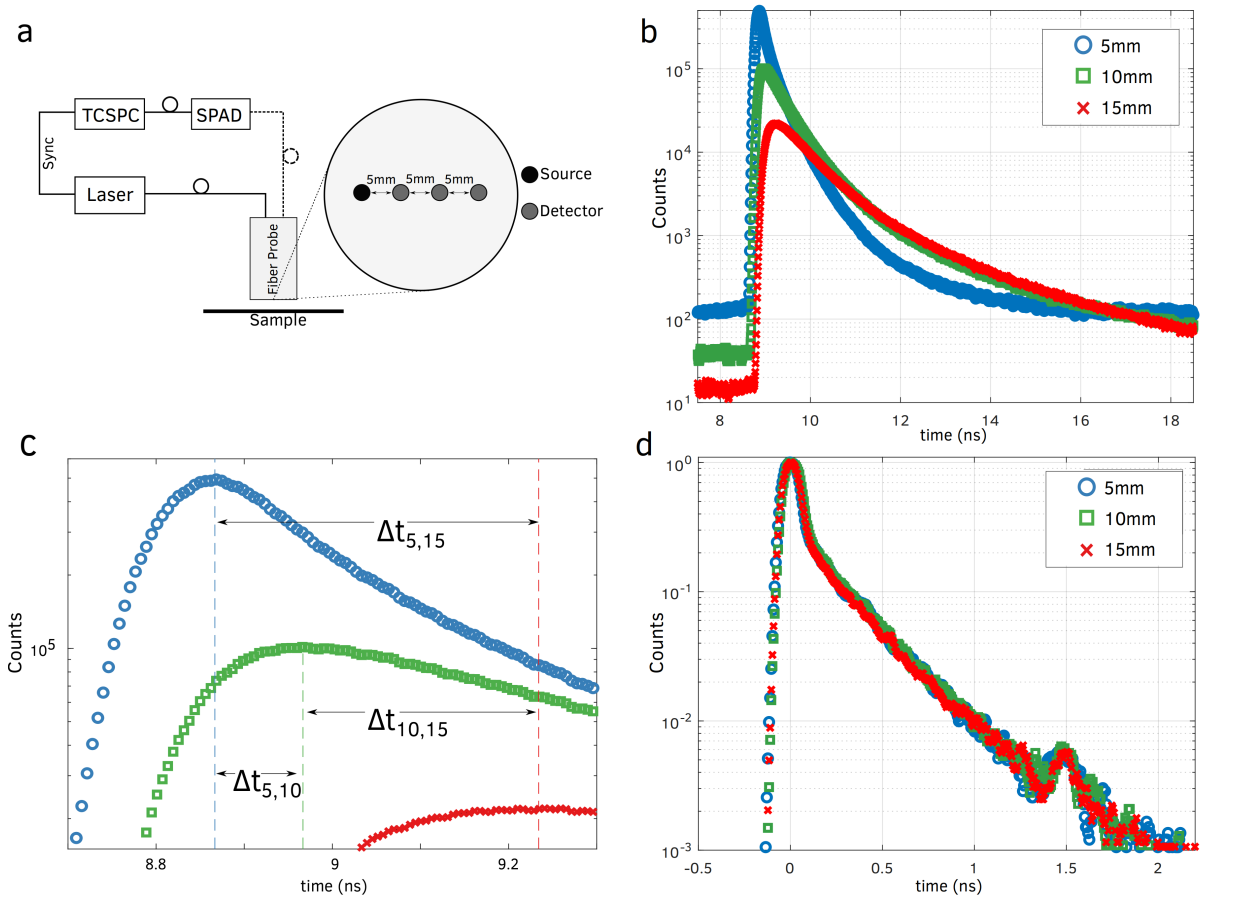

Figure 2.1: (a) Schematic of the time-resolved system used to obtain reflectance measurements. Dashed lines represent where the different detecting fibers connected to a detector (SPAD – single-photon avalanche diode; TCSPC – time-correlated single photon counter). (b) Time-resolved measurements from an Intralipid phantom at the three experimental SDS. (c) Magnified view of data in (b) to show peak-peak time differences observed between all SDS pairs. $\Delta t_{5,10}$ indicates the peak time difference between SDS of 5 and 10 mm ($\Delta t_{10,15}$: for 10 and 15 mm SDS; $\Delta t_{5,15}$: for 5 and 15 mm SDS). (d) Measured IRFs for the three SDS at 650 nm.

2.3.2 Monte Carlo simulations

Although DT can be used to model TPSF measurements at multiple SDS, it is known to be inaccurate for modeling reflectance at early times and small SDS [36, 163, 174, 114, 35]. Therefore, a previously developed time-resolved Monte Carlo (MC) model [170] was used to calculate the TPSF in a semi-infinite, homogenous geometry for 48 different tissue models. Each TPSF had distinct μ_s' and μ_a values spanning 3–18 cm^{-1} and $1 \times 10^{-3} - 0.5$ cm^{-1}, respectively. Tissue models were generated by permuting six different μ_s' values (3, 6, 9, 12, 15, 18 cm^{-1}) with eight different μ_a values (1×10^{-3}, 0.026, 0.050, 0.075, 0.18, 0.29, 0.39, 0.50 cm^{-1}). Absorption values were chosen on a log-scale to more accurately sample changes in absorption over several orders of magnitude.

Simulations were run to generate the TPSF (with photons being launched into and detected from the medium using optical fibers matching the experimental probe) at SDS of 5, 10 and 15 mm for all 48 tissue models. A temporal resolution of 2 ps was used for simulations at SDS of 5 mm, while the temporal resolution was 10 ps at SDS of 10 and 15 mm. Each MC run used 3×10^8 photons, an anisotropy equal to 0.7 (using the Henyey-Greenstein phase function), an index of refraction equal to 1.35 (to match the IL phantom) [120, 145, 54], and fiber diameters and numerical apertures of 400 μm and 0.22, respectively, to match experimental measurements. Simulated TPSF data were resampled (using a cubic spline) to have a resolution of 0.1 ps. The peak-times calculated from the cubic spline using two different temporal resolutions in generating the TPSF were compared to ensure no errors were introduced by resampling.

Representative TPSFs from MC simulations are shown at two SDS in Fig. 2.2(a) (SDS = 5 mm) and Fig. 2.2(b) (SDS = 15 mm) for three different media (circles: μ_s' = 6, μ_a = 0.18 cm^{-1}; squares: μ_s' = 9, μ_a = 0.18 cm^{-1}; triangles: μ_s' = 6, μ_a = 0.39 cm^{-1}). Vertical lines show tmax for each simulated reflectance (derived from the resampled data). These data show that in media with identical μ_s' an increase in μ_a causes a decrease in tmax (by 7 % at SDS of 5 mm and 13 % for SDS of 15 mm for media shown by circles vs. triangles), while in media with identical μ_a an increase in μ_s' causes an increase in tmax (by 11 % at SDS of 5 mm and by 35 % at SDS of 15 mm for media shown by circles vs. squares). These figures also show that at short SDS and low scattering, the absorption coefficient only weakly influenced tmax.

The difference (Δt) between tmax at SDS pairs of 5-10 mm, 10-15 mm and 5-15 mm, were obtained for each of the 48 simulations. For each SDS pair, Δt values across the 48 simulated tissue models were linearly interpolated to create 2D lookup tables of Δt values for μ_a spanning 1×10^{-3} - 0.5 cm^{-1} (in 1×10^{-3} cm^{-1} increments) and μ_s' spanning 3-18 cm^{-1} (in 0.01 cm^{-1} increments). Several interpolations methods were tested (e.g. linear, cubic, spline) to create lookup tables and showed less than 0.1 % variation in generated tables. These computed Δt distributions are shown for two different SDS pairs – in Fig. 2.2(c) (SDS pair of 5-10 mm) and Fig. 2.2(d) (SDS

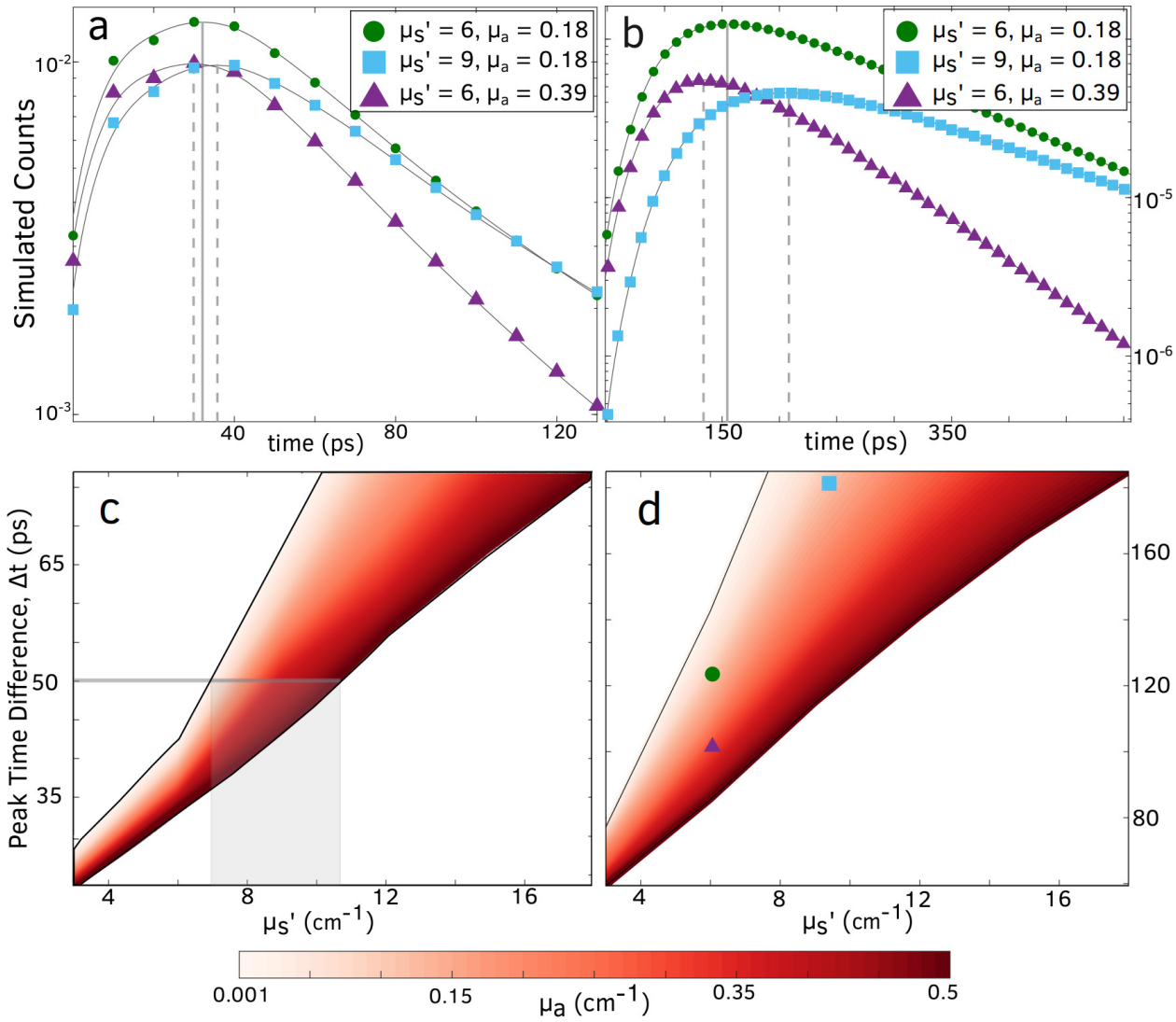

Figure 2.2: Monte Carlo simulated TPSF for three different media at SDS of (a) 5 mm and (b) 15 mm. Simulated data are shown in symbols while resampled splines (see text) are the solid lines. Vertical lines show the tmax for each simulation. Interpolated peak time differences for SDS of 5 and 10 mm ($\Delta t_{5,10}$) and for SDS of 5 and 15 mm ($\Delta t_{5,15}$) are shown in (c) and (d), respectively. Note that the time-difference scales are different in Fig. 2.2(c) and Fig. 2.2(d) with longer SDS having longer Δt. $\Delta t_{5,15}$ computed from tmax shown in Fig. 2.2(a) and 2.2(b) are marked on 2.2(d) (symbol, shape and color identify corresponding media). The grey rectangle in Fig. 2.2(c) represents how the range of μ_s' is determined by a fixed value of Δt (shown for $\Delta t_{5,10}$ = 50 ps).

pair of 5-15 mm). Symbols for $\Delta t_{5,15}$ values computed for data shown in Fig. 2.2(a) and 2.2(b) are marked on the Fig. 2.2(d) (shape and color of the marker identifies the optical properties). The horizonal grey line in Fig. 2.2(c) illustrates how a given Δt value (calculated using SDS of 5 and

10 mm) confines the range of μ_s' (shown by the shaded rectangle). In other words, $\Delta t_{5,10}$ = 50 ps could represent media with μ_s' ranging between 7.1 – 10.7 cm^{-1} and μ_a varying from 1×10^{-3} and 0.5 cm^{-1}.

2.3.3 Lookup method

Data shown in Fig. 2.2(c) and 2.2(d) form the crux of the lookup method. In the forward direction, specific values for μ_s' (x-axis) and μ_a (color) identify a single point in the shaded region – the ordinate of this point is Δt. In the inverse sense, given a Δt value (using a given SDS pair) it may be associated with several pairs of μ_s' and μ_a values (identified by the horizontal line within the shaded figure in Fig. 2.2(c)). Thus, translation of a measured Δt for a pair of SDS into μ_s' would require knowledge of μ_a, or vice-versa. As is evident from these figures, for fixed Δt, the limits on μ_s' are much more restrictive than the limits on μ_a. For the range of optical properties considered here, the required Δt for a SDS pair could be produced by media with μ_a that span the full range of simulated values (1×10^{-3} – 0.5 cm^{-1}) but had a much more confined range for possible μ_s' values. In other words, the uncertainty in estimation of μ_s' given an incorrect guess of μ_a would be much lower than the uncertainty in estimating μ_a given an incorrect guess of μ_s'. Thus, our lookup method translates the measured Δt (from a given SDS pair) directly into μ_s' via the interpolated 2D MC lookup table for the corresponding SDS, but needs an input value for the μ_a of the medium to function.

2.3.4 Estimating the absorption coefficient

Two different approaches were used to estimate the μ_a required for using the lookup method. The first approach, referred to here as the 'tail method', uses a limit derived from DT where the slope of the natural logarithm of the DTOF at long time scales is assumed to be directly proportional to μ_a (Eq. 2.1) [137]. shown in Eq. 2.1 represents the measured DTOF and for longer times, the value of the estimated absorption from Eq. 2.1 would improve. Using this technique to accurately estimate μ_a would require deconvolving the IRF from the measured DTOF and having the reflectance signal span many nanoseconds. In practice, a limited dynamic range in the detection system and the drawbacks in deconvolving the IRF from the DTOF reduces the accuracy of this approach in estimating μ_a.

However, as we expect Δt to only weakly depend on μ_a, the tail method provides a simple and direct way to extract (even if crudely) a value for use with the lookup method to estimate μ_s'. Further, due to a limited dynamic range of our instrumentation, the DTOF time scale was shifted such that the peak occurred at $t = 0$, and Eq. 2.1 was applied to analyze the measured reflectance signal from its peak value till it fell to 0.1 % of the peak value. Derivatives were numerically

calculated between successive times, smoothed and translated to calculate μ_a for each measured DTOF using Eq. 2.1 [137]. Because calculated numerical values were noisy and showed variations for different SDS (in the same media), μ_a was estimated as the averaged tail-method estimate for every scan, at all three SDS used.

$$\mu_a \approx -\frac{1}{c}\{\frac{d\ln R(r,t)}{dt} + \frac{5}{2t}\} \qquad \text{as } t \to \infty \tag{2.1}$$

In the second approach, referred to here as the 'transmittance method', the intrinsic absorption coefficient of hemoglobin was calculated by measuring the collimated transmittance using a spectrophotometer at the varying concentrations of bovine hemoglobin used experimentally (described in Sec. 2.5). μ_a was then calculated from the percent transmittance using Beer's Law for each concentration, and the intrinsic absorption coefficient () was determined from the slope of the linear fit of the calculated μ_a at each concentration. Expected (true) absorption coefficients of the medium distinct from values obtained using Eq. 2.1 were then calculated using and the mass concentration of absorber used. Dissolving large amounts of solid hemoglobin (≈ 255 mg for each concentration change) as well as uncertainties in cuvette calibrations in transmittance measurements could impact the accuracy of the estimated μ_a by this method.

2.3.5 Phantom preparation and measurements

Liquid phantoms were prepared to experimentally validate the performance of the developed method. Phantoms were prepared by mixing 40 mL of 20 % Intralipid (IL) (Sigma-Aldrich; MO, USA) with 750 mL of de-ionized water while absorption was independently introduced by serial additions of 250 mg of dry bovine hemoglobin (Hb) (H3760; Sigma-Aldrich; MO, USA) to the above solution. Liquid phantoms were prepared in a cylindrical container (radius = 6 cm, height = 12 cm) and preliminary experiments showed finite-boundary effects at low scattering solutions (¡ 1 cm^{-1}) and shallow depths (¡ 4cm). Therefore, the minimum μ_s' used for the experiments was 5 cm^{-1} and the minimum distance between optical channel and container wall was ensured to be greater than 5 cm to best approximate a semi-infinite medium as modeled by the MC lookup tables.

Phantoms were created to have constant scattering coefficient with 5 % IL by volume [169, 10]. Since the optical properties of IL have been well described to be stable and reproducible [120, 157], we could also use reference values from previous reports [114, 120, 157, 145] to directly compare the reduced scattering coefficient we estimated to those reported previously. Hb was added five times to create a set of 6 different phantom media having fixed scattering with step increases in the absorption coefficient (corresponding to hemoglobin concentrations ranging between 0-250 µM). This produced phantoms with expected μ_a values varying between 0.003-0.4 cm^{-1} for 650 nm,

and between 0.022-0.14 cm^{-1} for 800 nm.

Each phantom solution was prepared in the container and mixed gently with a magnetic stirrer during measurements. The sensing head of the probe (mounted on a custom probe holder) was lowered until the surface tension of the solution was broken. The probe was clamped in place and the following sequence of measurements was obtained for each phantom. First, the laser wavelength was set to 650 ± 5 nm, the optical fiber for the channel with SDS of 5 mm was manually coupled to the SPAD (via a standard SMA fiber socket) and three repeated scans were acquired. Next, the bandpass was adjusted to illuminate the sample at 700 ± 5 nm, 750 ± 5 nm and 800 ± 5 nm and three repeated TRS measurements were acquired. The same sequence of steps was repeated by manually coupling fibers for the 10 and 15 mm SDS channels into the SPAD, across the same four source illumination wavelengths. Each TRS acquisition was obtained by allowing the TCSPC signal to acquire the signal for 30 s.

Thus, a total of 36 TRS measurements was obtained (3 scans per wavelength, for 4 wavelengths across 3 channels), for each phantom solution. TRS scans collected at 650 nm are shown for all detection channels used (with SDS of 5, 10 and 15 mm) in Fig. 2.1(b). The difference between tmax of measured DTOF at 5 and 10 mm SDS is also shown and labelled as $\Delta t_{5,10}$ in Fig. 2.1(c). A similar naming convention was adopted when peak differences were calculated using SDS of 5 and 15 mm ($\Delta t_{5,15}$) and SDS of 10 and 15 mm ($\Delta t_{10,15}$), as denoted in Fig. 2.1(c). Experimental DTOF measurements were obtained with time-resolutions of 12 ps.

2.4 Results

As described above, the MC lookup table was used to convert the measured Δt (for a given SDS pair) into μ_s', given an estimate of μ_a. We first tested the developed method to extract μ_s' for phantom that was mostly scattering with very low absorption – i.e. a solution of 5 % IL in water. Fig. 2.3 shows extracted μ_s' as a function of illumination wavelength for the phantom with 0 µM hemoglobin (5 % IL in water) using the lookup method at all three experimental SDS pairs possible (circles: $\Delta t_{5,10}$; diamonds: $\Delta t_{5,15}$; squares: $\Delta t_{10,15}$; stars: literature average from Refs. ([114, 120, 157]). Input values for μ_a were estimated using the tail method from measured data. Derived μ_s' values in Fig. 2.3 show expected wavelength dependent decreases in scattering for all the three SDS pairs and tracked expected values from literature. Although $\Delta t_{5,10}$ produced μ_s' closest to reference values, both $\Delta t_{5,15}$ and $\Delta t_{10,15}$ showed agreement (to better than 25 %) with the reported intrinsic scattering parameters of IL [120]. Larger errors are observed at smaller SDS as the uncertainty in derived μ_s' was high due to the uncertainty in correctly estimating the peak time with the experimental temporal resolution of 12 ps (TCSPC bin-width). Error bars shown represent the standard error from three repeated measurements for each concentration at each wavelength and

SDS.

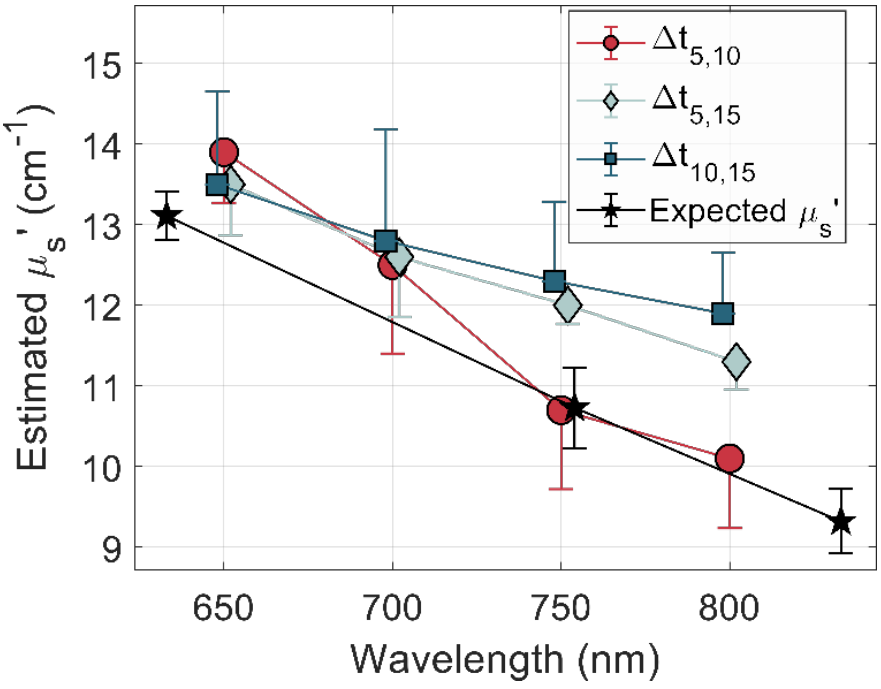

Figure 2.3: Estimated μ_s' values obtained from experimental Δt measurements in a solution of 5 % IL in water (from each SDS pair) at each wavelength, together with expected (literature) μ_s' values. Markers show the average of three repeated scans. Data obtained using $\Delta t_{5,10}$ most closely matched expected values while those obtained from using $\Delta t_{5,15}$ and $\Delta t_{10,15}$ still closely followed spectral trends predicted from literature values. The look up estimates were made by obtaining absorption using the tail method (see text). The points are jittered if they share the same independent variable. Error bars represent the standard error for the three repeated measurements at each point (only one side of the error bar is shown for the derived values in the figure for clarity).

The values of μ_a used to derive μ_s' shown in Fig. 2.3 were estimated using the tail method and could yield inaccurate results. We therefore examined the impact of changing the input μ_a on the extracted value of μ_s', for any given DTOF. This was done by first, using an initial μ_{a0} (obtained for example using the tail method) to derive the scattering coefficient μ_{s0}' using the lookup method. This value of μ_{a0} was then decreased by 20 - 100 % in five equal intervals (where a decrease of 100 % was the smallest simulated $\mu_a = 1 \times 10^{-3}$ cm^{-1}) to determine an updated absorption coefficient μ_{a1} and then using μ_{a1} as the input to the lookup method to determine the corresponding updated scattering coefficient μ_{s1}'.

Percent errors in μ_{s1}' (relative to μ_{s0}') are shown in Fig. 2.4, as a function of percent changes in input μ_{a0}, for the three experimental SDS pairs (bars) used here. Data in Fig. 2.4 represent DTOFs obtained from four different (representative) media – Medium 1 (Fig. 2.4(a)): μ_{s0}' = 10, μ_{a0} = 0.05 cm^{-1}; Medium 2 (Fig. 2.4(b)): μ_{s0}' = 10, μ_{a0} = 0.16 cm^{-1}, Medium 3 (Fig. 2.4(c)): μ_{s0}'

= 13, μ_{a0} = 0.05 cm^{-1}; Medium 4 (Fig. 2.4(d)): μ'_{s0} = 13, μ_{a0} = 0.16 cm^{-1}). DTOFs to estimate μ'_{s0} in Fig. 2.4(a) and 2.4(c) were obtained from the pure scattering phantom (no hemoglobin) for illumination with 800 and 650 nm, respectively. DTOF used in Fig. 2.4(b) corresponds to the phantom with 256 μM Hb for 800 nm illumination, while DTOF for Medium 4 (Fig. 2.4(d)) was from the phantom with 53 μM Hb with illumination at 650 nm (these phantoms were selected because their absorption coefficients for the wavelengths and concentrations used were comparable to each other).

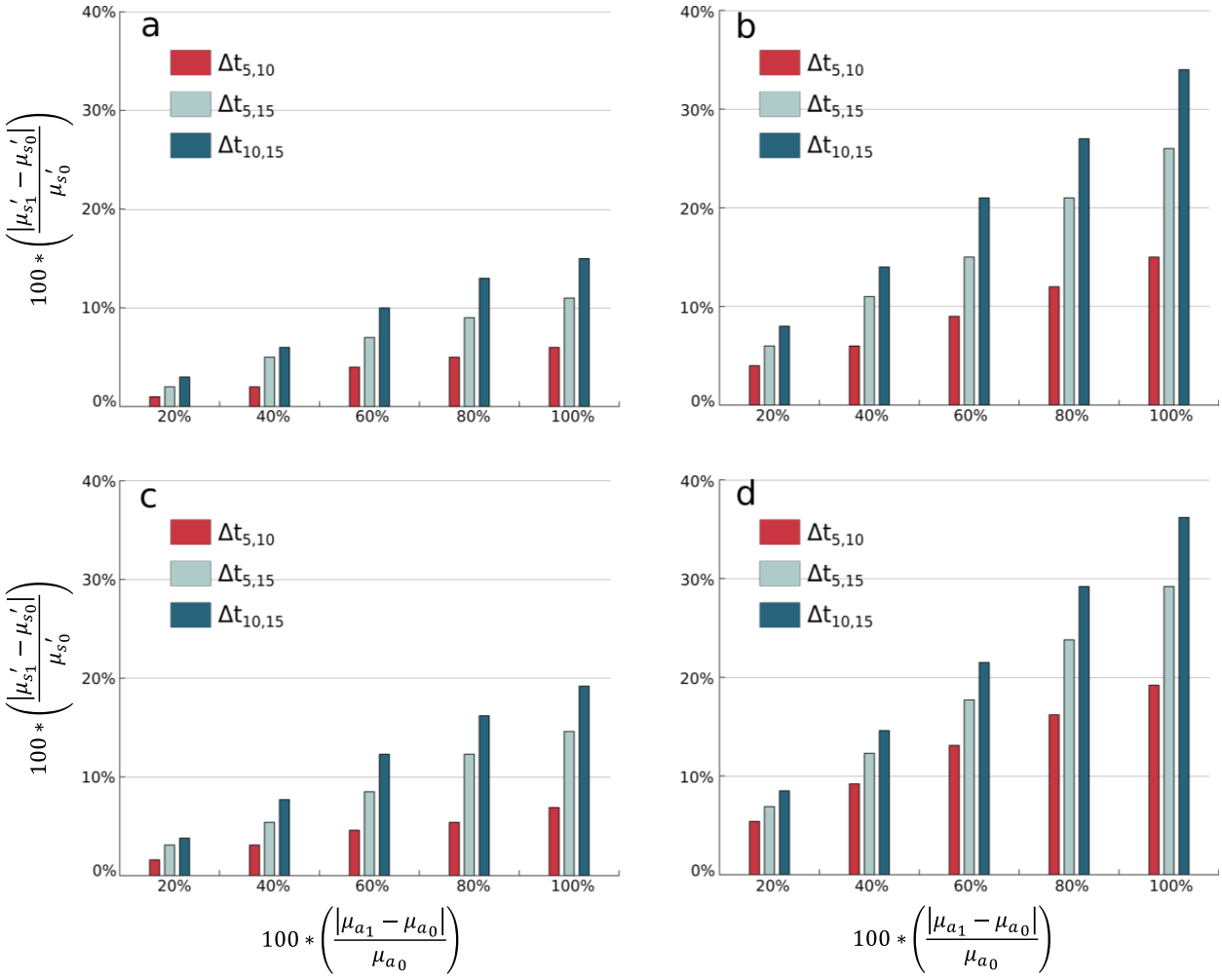

Figure 2.4: The change in the estimated scattering coefficient given a decrease in the initial absorption coefficient used in the lookup table is shown. Four different media are shown representing optical properties at 800 nm (μ'_s = 10 cm^{-1}; (a) and (b)) and 650 nm (μ'_s = 13 cm^{-1}; (c) and (d)). μ_{a0} values used as input into the lookup table was 0.05 cm^{-1} for (a) and (c) while μ_a = 0.16 cm^{-1} for (b) and (d). Input absorption coefficient were decreased by 20 % of the initial value in five steps and the percent change in retrieved μ'_s are shown.

It is clear to see from Fig. 2.4 that the derived μ'_s using $\Delta t_{5,10}$ varied less than 8 % as the input

μ_a values were varied by 100 % in media with lower absorption (Fig. 2.4(a) and 2.4(c)), as was expected from the MC simulations. Additionally, even for the longest SDS pair (10-15mm) used, the change in extracted μ_s' was lower than 20 % as the input absorption coefficients changed by 100 %. However, when μ_{s0}' was obtained with higher absorption coefficients (μ_{a0} of 0.16 cm^{-1}, Fig. 2.4(b) and 2.4(d)) the changes in the medium's absorption translated to larger variations in extracted μ_s'. In general, the larger the error (or uncertainty) in knowledge of a medium's true μ_a the larger the error in the recovered μ_s'.

Next, we tested the performance of the lookup technique to estimate μ_s' in phantoms as the absorption coefficient was varied. Acquired DTOF's using all available SDS and illumination wavelengths (with three SDS pairs and four wavelengths) were analyzed using the MC lookup method to translate the measured values of Δt into μ_s', in each of the 6 experimental phantoms prepared. Fig. 2.5(a) shows the μ_s' extracted by the lookup method (for each SDS pair) in phantoms with varying hemoglobin concentrations for illumination with 750 nm and obtaining the input μ_a coefficients from the DTOFs using the tail method. Fig. 2.5(b) shows these data for the same phantoms shown in Fig. 2.5(a) but used the transmittance method (described in Section 2.4) to determine input μ_a. Both Fig. 2.5(a) and 2.5(b) indicate that that the μ_s' values obtained from $\Delta t_{5,10}$ with the lookup method matched the expected (literature) values (shown as dashed horizontal lines [114, 120, 157]). Further, all three SDS pairs extracted consistent μ_s' values in all the six phantom media that had different absorption properties.

Table 2.1 shows the mean percent errors between lookup table derived μ_s' and literature values averaged across all wavelengths, for each SDS pair while using the tail method to determine the μ_a used in the lookup table. Percent errors reported in Table 2.1 varied lesser than 7 % of the values obtained when the transmittance method was used to estimate μ_a. Largest deviations between the two approaches were observed in media with highest absorption where the influence of the IRF impacts the derived values most significantly.

Table 2.1: Percent errors between estimated and expected (true) values of μ_s' for each source-detector pair averaged across all experimentally measured wavelengths. μ_s' was recovered using the decay rate of the DTOF tail to determine the μ_a used in the MC lookup table (see text).

Source Detector Pair	Concentration of Hemoglobin						
	0μM	0μM	0μM	0μM	0μM	0μM	mean
$\Delta_{5,15}$	8.2 % (SD = 4.2)	7.7 % (SD = 6.4)	6.4 % (SD = 4.1)	8.2 % (SD = 5.9)	10.9 % (SD = 3.3)	14.6 % (SD = 6.6)	9.4 % (SD = 5.4)
$\Delta_{5,10}$	2.9 % (SD = 3.1)	4.6 % (SD = 2.0)	2.3 % (SD = 1.8)	3.9 % (SD = 3.3)	9.3 % (SD = 8.5)	10.5 % (SD = 11.0)	5.6 % (SD = 6.6)
$\Delta_{10,15}$	10.8 % (SD = 6.5)	11.7 % (SD = 10.2)	10.4 % (SD = 7.6)	11.4 % (SD = 8.6)	13.8 % (SD = 6.7)	15.8 % (SD = 8.8)	12.3 % (SD = 6.9)
mean	7.3 % (SD = 5.6)	8.1 % (SD = 7.1)	6.4 % (SD = 5.8)	7.8 % (SD = 6.6)	11.4 % (SD = 6.2)	13.7 % (SD = 8.0)	

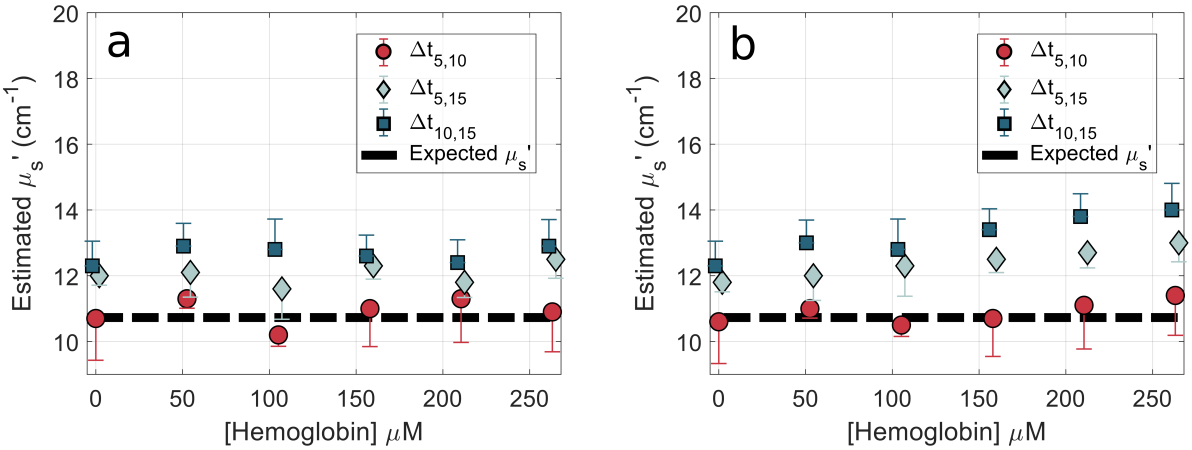

Figure 2.5: Estimated μ_s' at 750nm are shown across six concentrations of hemoglobin utilizing two separate methods to determine the μ_a used in the lookup table: (a) the slope of the DTOF tail and (b) measured transmittance of pure hemoglobin. The true (expected) μ_s' is shown as a dashed horizontal black line. Estimated values using $\Delta t_{5,10}$ most closely tracked expected values, but all three SDS pairs once again produced consistent estimates of μ_s' across the six phantoms. Points are shown as jittered if they share the same independent variable and only one side of error bar are shown here for clarity. Error bars represent the standard error of the estimated scattering coefficient by using each of the three repeated scans for each SDS (in the SDS pair) to estimate Δt.

At wavelengths of 750 and 800 nm, estimating μ_a via the tail method provided improved accuracy in estimating μ_s'. However, at wavelengths of 650 and 700 nm, calculating μ_a using the tail method decreased accuracy in estimating μ_s' (μ_a obtained via transmittance data yielded lower errors in extracted μ_s' in these cases). Best accuracy was obtained for media with low μ_a and by using SDS pairs closest to the source (these data cells are highlighted in Table 2.1).

2.5 Discussion

We have described a heuristic technique capable of assessing the reduced scattering coefficient of a homogenous medium directly from experimentally measured TRS signals. We have shown that an experimentally measured peak-time difference between DTOFs at two different SDS can be translated to obtain a robust estimate of the medium's scattering coefficient using preconstructed MC lookup tables. Although our method requires an input (estimated) value for the absorption coefficient, the derived μ_s' using our approach is only weakly dependent on the input absorption coefficient. Application to experiments with tissue phantoms showed that we could estimate the expected (true) scattering coefficients in media with errors ranging from 5 % -25 %.

A principal advantage of the presented technique is its inherent speed and simplicity of use

(i.e. directly being able to translate measurements into the reduced scattering coefficient of the medium). However, it is worth noting that there are important instrumentation calibration and prerequisite conditions that must be satisfied for it to function accurately. Although our method does not use the IRF for translating measurements into the medium's scattering coefficient, it is not independent of it. It is critical for the IRF (i.e. the intrinsic temporal shape of the incident laser pulse) to remain stable across the duration of experiments and also be identical for each measurement channel used. In our case, each channel used the same length and type of fiber and were all detected by a common detector and as shown in Fig. 2.1(c) were identical across channels for all wavelengths. Systems that use different fiber lengths and/or employ multiple photodetectors that seek to use this technique might need to consider such issues carefully during development of lookup tables.

Phantom results showed that errors between literature (expected) values and derived values were (on average) lower than 6 % when data from SDS of 5 and 10 mm were used and were as high as 25 % when data from SDS of 10 and 15 mm were used. Thus, utilizing smaller SDS would yield the best estimates of scattering, consistent with previous reports [140, 144, 164, 116]. We note that accurately resolving peak time-differences for small SDS requires higher temporal resolution of measured data. Further, non-linear distortions in tmax (from the convolved IRF response) could impact longer SDS measurements more and may explain our findings.

Our findings are consistent with previous reports showing that the peak arrival time (tmax) of the DTOF is strongly sensitive to μ_s' and only weakly to μ_a [131, 35], especially for shorter SDS. It also builds off separate work seeking to mitigate the influence of the IRF in TRS analysis [122, 182, 99]. Data shown in Fig. 2.2(a) and 2.2(b) reflect these findings, where both μ_s' and μ_a impact the peak time to varying degrees, but as denoted in Fig. 2.2(c) (shaded bar), a fixed value for Δt (for a given SDS pair) tightly binds the range of allowed μ_s' values, but not μ_a. Although the technique needs an input estimate for μ_a, this can be derived by applying Eq. 2.1 directly to the measured DTOF. Accurately using Eq. 2.1 to estimate μ_a would require a large dynamic range in the detecting system and deconvolving the IRF.

Here, we have shown (Fig. 2.4) that only a rough estimate of μ_a is needed as it weakly affects the peak position. Utilizing smaller SDS decreases the effect of absorption on the peak time difference leading to more accurate estimates of μ_s' by reducing the probed volume. Therefore, small SDS would be more sensitive to shallower layers of the medium, while longer SDS could differentially be used to probe deeper tissues. The extension of this method to inhomogeneous media will be addressed in future investigations. Although not experimentally studied here, any fiber geometry with at least two detector channels with unique SDS would be amenable for use with the lookup method presented. Further, using this method to derive the scattering by setting μ_a=0 could be used to obtain a lower bound on μ_s'.

We also note that the SDS must be well defined (within 0.5 mm) to accurately estimate μ_s'. Peak times between DTOF's at 10 and 11 mm SDS could vary by ≈ 50 % translating into recovered error of ≈ 80 % in μ_s'. Additionally, although MC simulations and experimental geometries must be matched (i.e. we need experimental measurements from large volumes to represent semi-infinite media) we note a specific advantage of this method in "finite" geometries as only the earliest arriving photons determine Δt – and thus, could be robust against boundary effects.

The described method could be used to bootstrap (or confine the range of μ_s') other analytical inverse solvers to quantify optical properties from TRS measurements, especially in weakly scattering media where DT-based approaches are typically more vulnerable to higher errors [36, 141, 2, 131, 35]. Uncertainty in the index of refraction of the medium also weakly affects the relative peak-time difference. Lastly, since this method works by establishing the temporal peak of measured DTOF reflectance profiles, it should be possible to sparsely sample the DTOF histogram to acquire data faster. These topics will be subject of future investigations.

2.6 Conclusion

An easy-to-use approach to extract μ_s' of turbid media that overcomes current limitations in TRS analysis was presented. By using a pair of short SDS (< 10 mm), we show that μ_s' can be estimated within 6 % of reference values with reasonable estimations of μ_a. The approach could be further extended to include timing differences of later arriving photons as well as aid traditional inverse solvers in further parameterizing optical properties. The method shows great promise in recovering a medium's optical transport properties via TRS in regimes where common techniques fail, while facilitating quantitation in real-time without directly measuring the IRF.

CHAPTER 3

Reconstruction of Optical Coefficients in Turbid Media Using Time-Resolved Reflectance and Calibration-Free Instrument Response Functions

This chapter was published in [72]. It introduces three approaches to reconstruct the optical properties of turbid media from time-resolved reflectance measurements considering an uncertainty in the time scale of the instrument response function. This chapter extends methods discussed in Chapter 2 [70] and was prepared in collaboration with Dr. Karthik Vishwanath and Dr. Mary-Ann Mycek.

3.1 Abstract

Measurements of time-resolved reflectance from a homogeneous turbid medium can be employed to retrieve the absolute values of its optical transport coefficients. However, the uncertainty in the temporal shift of the experimentally determined instrument response function (IRF) with respect to the real system response can lead to errors in optical property reconstructions. Instrument noise and measurement of the IRF in a reflectance geometry can exacerbate these errors. Here, we examine three reconstruction approaches that avoid requiring direct measurements of photon launch times. They work by (a) fitting relative shapes of the reflectance profile with a pre-determined constraint on the scattering coefficient, (b) calibrating launch-time differences via a reference sample, and (c) freely fitting for the launch-time difference within the inverse problem. Analysis methods that can place a tight bound on the scattering coefficient can produce errors within 5-15 % for both absorption and scattering at source-detector separations of 10 and 15 mm. Including the time-shift in the fitting procedure also recovered optical coefficients to under 20 % but showed large crosstalk between extracted scattering and absorption coefficients. We find that the uncertainty in the temporal shift greatly impacts the reconstructed reduced scattering coefficient compared to absorption.

3.2 Introduction

Time-domain diffuse optical spectroscopy (TD-DOS) measures the distribution of times-of-flight (DTOF) of photons propagating through the sample from a source to a detector [186, 140]. DTOFs are obtained statistically using time-correlated single photon counting (TCSPC) [186, 163] and several short (picosecond) laser pulses detected using a fast single photon avalanche diode (SPAD) [140, 62, 32]. TD-DOS has been widely applied for biosensing applications in diffuse optical imaging (DOI) and diffuse reflectance spectroscopy (DRS) [62, 32, 180, 92]. In most biomedical applications for in vivo tissue sensing, near-infrared (NIR) light is used to provide functional (e.g., hemodynamics) and structural (e.g., cell size/density) information about the underlying biological tissue by quantifying the medium's absorption coefficient μ_a and reduced scattering coefficient μ_s' [181, 90]. When acquired in the time-domain, experimental measurements are better able to decouple μ_a and μ_s' while also allowing for depth discrimination of absorption changes, compared to continuous wave measurements [140, 38].

To determine a medium's optical properties from a measured DTOF, a theoretical (forward) solution to the time dependent photon diffusion equation [62, 125] is used iteratively as an inverse model to fit measurements for known source-detector separations (SDS) and tissue geometries [186, 62, 125]. A Green's function approach [30, 85] is used to develop an analytical solution – the medium's temporal point spread function (TPSF) – to an idealized delta-function input, $\delta(t-t_0)$ with t_0 = 0 ns. To account for experimental temporal shapes of sources and response of detectors, the forward model is computed with a convolution of the TPSF and a measured Instrument Response Function (IRF) [62, 125]. The inverse problem is known to be significantly dependent on both the shape and temporal position of the IRF [97, 143]. Therefore, for accurate reconstructions, it is critical to carefully measure both the temporal shape and absolute temporal position of the IRF relative to the measured DTOF, for each wavelength and detector channel [97, 143].

Because experimental DTOFs are fit with a forward model comprised of the convolution of the TPSF and the IRF, it is important to know when the injected pulse enters the medium (i.e., t_0 in Fig. 3.1(a)). The difficulty in measuring t_0 is schematically illustrated in Fig. 3.1. We note that the IRF is impacted by both its temporal position t_0 and shape. Each collection geometry can also produce an IRF with a different shape due to the inclusion of a thin diffusor (Fig. 3.1(a) vs 3.1(b)) or from a larger distribution of possible photon paths (Fig. 3.1(c)). When measured with the configuration shown in Fig. 3.1(a), t_0 is taken to be the peak or barycenter of the measured IRF [143]. In practice, the configuration shown in Fig. 3.1(b) is used, where a strongly scattering and attenuation layer is placed between the source and detecting fibers which introduces some small delay Δt_1, in the barycenter of the IRF, relative to Fig. 3.1(a) [143]. However, in reflectance spectroscopy, custom probes are epoxied at the sample end leading to immovable relative configurations of the

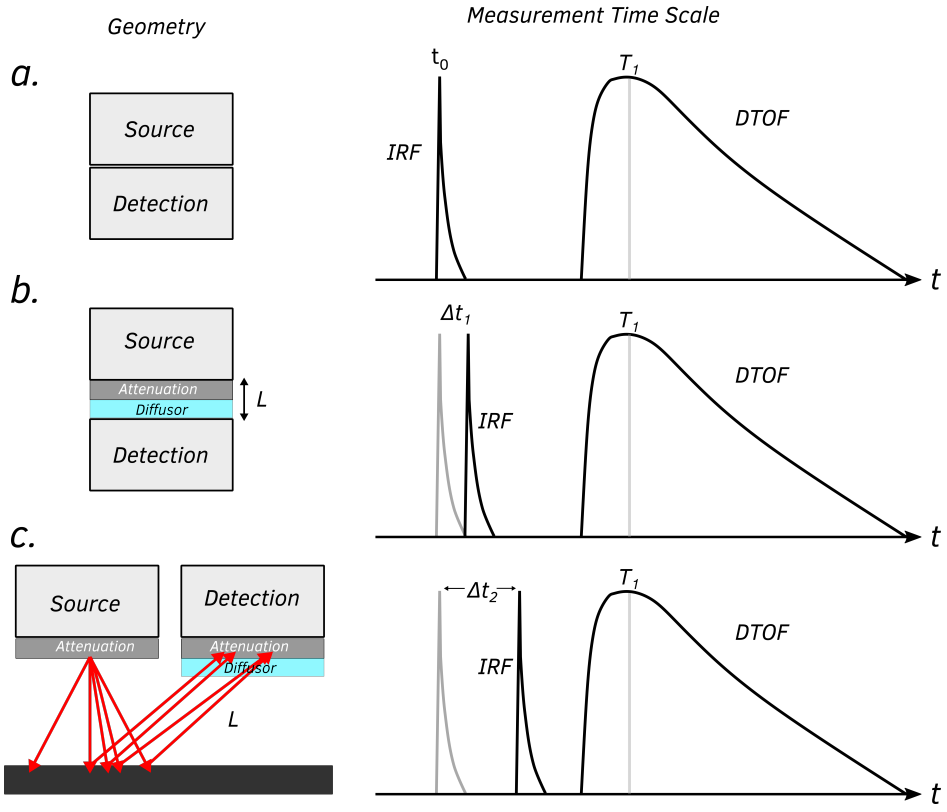

Figure 3.1: Left column: Experimental configurations for measuring the instrument response function (IRF) in different geometries. Right column: temporal relationships between the measured IRF and the distribution of times-of-flight (DTOF) for photons from an arbitrary turbid medium for each corresponding experimental configuration. (a) The ideal (best possible) geometry for measuring the IRF – by directly coupling the source and detection fiber. t_0 represents the launch time of the incident photon pulse into the medium. (b) A practically used configuration – by introducing attenuating and diffusing layers between the source and detector fiber. This introduces a time delay Δt_1 relative to the configuration in Fig. 3.1(a). (c) Reflectance configuration – by directing the incident pulse onto a surface and reflecting the incident pulse into detector. This introduces a larger time delay Δt_2, with $\Delta t_2 > \Delta t_1$.

source and detector fibers. Thus, acquisition of the IRF requires collection in reflection geometry (Fig. 3.1(c)) and from an appropriate reflecting material [62, 143]. This increases the IRF barycenter position by Δt_2 relative to Fig. 3.1(a). In order to fit a measured DTOF, knowledge of Δt_2 is needed, and thus requires careful calibration for quantitative reconstructions [143, 9].

Several approaches have been explored to analyze collected DTOFs in terms of the optical properties as well as to quantitate functional changes and depth sensitivities while limiting the contribution from the IRF [173, 100, 98, 99]. In addition to fitting the entire DTOF using a theoretical model, methods for reducing the dimensionality of the collected DTOF have been developed such

as exploiting time-dependent mean partial pathlengths [4, 39], integrated photon counts in various time windows [173, 154], moment analysis [173, 100, 99], and Fourier components of the DTOF [129]. Moment analysis has particularly been shown as a promising technique to limit the errors arising from IRF measurements, as those discussed above, while also being sensitive to identifying depth-dependent absorption changes in media [173, 100].

Here, we examine three approaches to reconstruct measured DTOFs without requiring direct experimental measurements of Δt. 1) A constrained Monte-Carlo Diffusion Theory (MC-DT) approach that operates by shifting the DTOF and the convolved TPSF and IRF to peak at t = 0 while strongly restricting μ_s' values in the inverse model. The imposed constraint on μ_s' was achieved using a recently developed technique [70] that translates the measured differences of DTOF peak times at two different SDS from Monte-Carlo lookup tables (MCLUT) into μ_s'. 2) A calibrated-DT approach that uses a reference sample to calculate Δt as described previously [62]. This calculated Δt is used to shift the IRF before inverse fitting for each target phantom. 3) A free-shift DT approach – here a third parameter t_s is included to be freely fitted with μ_s' and μ_a in the inverse procedure. A time-variable is introduced into the DT-model to provide the TPSF for a delta-function input at ts. Relative merits and drawbacks of each technique using performance metrics across a large set of tissue simulating phantoms are discussed.

3.3 Materials and methods

3.3.1 Hardware

The instrumentation used for experimental measurements is as described previously [70]. Briefly, a super-continuum laser (SC400, NKT Photonics, DK) with a pulse duration < 100 ps was spectrally filtered using a band-pass filter (SuperK VARIA, NKT Photonics, DK) with a repetition rate of 40 MHz. Laser pulses were delivered to and collected from the sample by 400- μm diameter optical fibers placed with center-center separation ρ and in contact with the sample surface. The reflectance was measured using a SPAD detector (PMD-050, MPD, IT) that was electronically coupled to a time-correlated single photonic counting (TCSPC) board (SPC-130, Becker & Hickl, DE). The IRF was obtained in reflectance geometry by reflecting the source from a mirror into the detecting fiber that was covered by a piece of paper, as described previously [70]. The full-width half maximum of the IRF for each detection channel and wavelength was measured to be less than 80 ps. A custom optical fiber probe was used that consisted of 4 colinear optical fibers (400 μm, NA 0.22) to form 3 detection channels. Each channel had a SDS of 5, 10, and 15 mm (measured from one fiber, at the edge of the collinear array, set to be the source). Because our system used a single detector, the detecting fiber head was manually switched to select for any specific SDS.

3.3.2 Phantom tests

For the measurements, a cylindrical glass container (8-cm diameter and 8-cm height) was filled with an aqueous solution of 20 % Intralipid (IL) (Sigma-Aldrich; MO, USA) and dried bovine hemoglobin (Hb) (H3760; Sigma-Aldrich; MO, USA). Optical characterization of μ_s' was taken from the average values of the intrinsic reduced scattering coefficient of 20 % IL performed by multiple independent research groups [158, 120]. The accuracy of this optical characterization was confirmed by a comparison between experimental data of pure IL solutions and Monte Carlo simulations [70]. The intrinsic absorption coefficient of Hb was calculated by measuring the transmittance at four concentrations using a spectrophotometer and then extracting the intrinsic absorption coefficient from the linear fit. The absorption coefficient of the medium was then calculated by the intrinsic absorption coefficient along with hemoglobin's relative mass fraction to water and IL [158]. Two separate phantom sets with two different scattering levels were prepared by using 20 mL of 20 % IL (set 1) and 40 mL of 20 % IL (set 2) mixed with 750 mL of deionized water. The absorption coefficients in each set were independently varied by eight serial additions of ≈ 250 mg of dry bovine hemoglobin. For each laser wavelength used, a total of 18 different samples of optical properties, combining nine values of (per set) μ_a with each set having one of two levels of μ_s'. Four laser wavelengths were used (with center wavelengths of 650 nm, 700 nm, 750 nm and 800 nm $\pm$ 5 nm) to create 72 different phantom tissue models with known optical properties. Three repeated measurements were performed on each sample, at all available SDS (ρ = 5, 10, 15 mm), and signals were acquired for 30 s per sample.

3.3.3 Data analysis

Collected DTOFs were analyzed using a known solution from diffusion theory to simulate the reflectance in a semi-infinite homogeneous medium [62, 109]:

$$R(t) = \frac{\nu}{2A}\left(\frac{1}{4\pi Dt}\right)^{\frac{3}{2}} \exp\left(-\frac{\rho^2}{4Dt} - \mu_a \nu t\right) \times \left[\exp\left(-\frac{z_+^2}{4Dt}\right) - \exp\left(-\frac{z_-^2}{4Dt}\right)\right] \tag{3.1}$$

where ν is the speed of light in the medium, D is the optical diffusion coefficient $1/(3(\mu_a+\mu_s'))$, ρ is the source-detector separation, A accounts for the index mismatch between the detector and medium [30], $z_+ = z_s$ and $z_- = -2z_e - z_s$ with $z_s = 1/\mu_s'$ and $z_e = 2A/(3\mu_s')$. Diffusion theory serves as a good approximation of photon propagation when ρ is much larger than zs and when $\mu_s' \gg \mu_a$ [186, 109]. The expression in Eq. 3.1 represents the medium's response to a source represented by a delta-function $\delta(t - t_0)$ when $t_0 = 0$, and measured as in Fig. 3.1(a). Experimentally collected DTOFs represent the phantom's response to an experimental IRF, $\tilde{R}(t)$, which is given by the convolution of Eq. 3.1 with the system's IRF, i.e., $\tilde{R}(t) = R(t) \bigotimes IRF(t, t_0 + \Delta t)$ where

t_0 represents the photon launch time and Δt represents a time delay in the measured IRF due to non-ideal measurement geometries shown in Fig. 3.1(b) and 3.1(c).

As discussed in Fig. 3.1, the time t_0 represents the photon launching time, which is typically considered as the peak or barycenter of the measured IRF when the IRF is measured by directly coupling the source and detecting fiber. Typically, the use of a t_0 parameter in Eq. 3.1 is not needed because t_0 for IRF and the DTOF measurements are equal. Thus, convolution of the IRF with $R(t)$ puts $\tilde{R}(t)$ on the correct time scale, relative to the DTOF. In our experiments, the IRF was collected as shown in Fig. 3.1(c) (in a reflection geometry) since the fiber probe was configured for reflectance measurements. This introduced a shift Δt in the IRF time scale. Thus, without knowledge of those time-shifts, $\tilde{R}(t)$ could not be directly compared to measured DTOFs. We consider three different procedures to recover both μ_s and μ_a using time-resolved reflectance obtained at one or more SDS, that do not depend on directly requiring Δt or t_0 for reconstructions and refer to them as (a) MC-DT (b) Calibrated-DT, and (c) Free-shift DT.

In the MC-DT approach, both $\tilde{R}(t)$ and the DTOF are shifted so that they peak at $t = 0$ ns. A constraint is then placed on μ_s' in the inverse model using a previously described approach to estimate μ_s' from relative peak-time differences with MCLUTs [70]. The fitting bound for μ_s' was calculated from the MCLUT using μ_a = 0.001 and 0.5 cm^{-1} as a lower and upper bound, respectively given a measured Δt_{max} at SDS of 5 and 10 mm. Such an approach does not require absolute time scales as it operates on the relative difference between peak arrival times at two SDS which is a primary requirement for this study.

The calibrated-DT approach indirectly calculates Δt by fitting $\tilde{R}(t)$ to a DTOF collected from a calibration reference phantom with known optical properties [62] for which Δt is considered a fit parameter that minimizes the least-square error between measurements and reconstructions. A Δt is estimated for each wavelength and SDS to shift the IRF time scale before fitting the DTOFs from target phantoms.

In the free-shift DT approach, Eq. 3.1 is modified by making the replacement $t \rightarrow t - t_s$ and ts is used as an additional parameter in the inverse model to optimize for along with μ_s' and μ_a. This has the effect of introducing an additional parameter in the forward model that allows for $\tilde{R}(t - t_s)$ time scale to be moved to appropriately match the DTOF. Analysis for all three methods utilized the following procedure. Collected DTOFs and $\tilde{R}(t)$ were normalized by their maximum count rate, optical properties were then determined by fitting the DTOF with $\tilde{R}(t)$ utilizing a Levenberg-Marquardt procedure to minimize the least-square error [62, 131]. The sample was considered to have a refractive index of 1.35 to match reported values for IL solutions [120] with an external index of refraction of 1.5 to match the glass optical fibers. The fitting range included all count rates higher than 60 % of the peak value on rising edge of the DTOF and 0.1 % on the tail. The range of optical properties in the fitting procedure was taken to be between $1 \leq \mu_s' \leq 60\,\mathrm{cm}^{-1}$

and $0.001 \leq \mu_a \leq 0.5\,\mathrm{cm}^{-1}$. Twenty random start values in the described ranges were utilized in the inverse procedure, and the calculated μ_a and μ_s' that showed the lowest least-square error were taken as the converged optical properties. A one-way ANOVA test was performed for the three analysis methods considering the recovered absorption and scattering coefficients separately at each SDS. Data was averaged across all experimental concentrations and wavelengths and a post-hoc Tukey honestly significant difference test was performed to indicate significant differences between analysis methods.

3.4 Results

Example fits for the three methods (a) MC-DT, (b) Calibrated DT, and (C) Free-shift DT are shown in Fig. 3.2 considering the same experimental DTOF and IRF with expected (true) optical properties of μ_s' = 11.1 cm^{-1} and μ_a = 0.19 cm^{-1}. In the MC-DT approach (Fig. 3.2(a)), the IRF, DTOF, and $\tilde{R}(t)$ are shifted to peak at $t = 0$. By constraining μ_s', the MC-DT approach had the largest residuals in fitting (R^2 = 0.94) due to the poor fit at early times (before the peak). However, it often resulted in higher accuracy in the recovered optical properties. The calibrated-DT approach is shown in Fig. 3.2(b). Δt was calculated from a solid phantom [108, 18] reference and used to shift the IRF time scale. The time scales of both the DTOF and IRF are translated so the IRF peaks at $t = 0$ as shown in Fig. 3.2(b). A main difference between the calibrated DT and free-shift DT is the time scales between Fig. 3.2(b) and 3.2(c). In Fig. 3.2(c), the time scale of the IRF and DTOF are the same as the TCSPC measurements. The difference between the IRF and DTOF peak times in Fig. 3.2(b) and 3.2(c) are due to not accounting for the Δt shift in Fig. 3.2(c).

In Fig. 3.3, we show the recovered optical properties for the three methods across the entire set of phantoms measured, at a SDS of 15 mm and illumination at 700 nm. These trends (not shown) were similar for other wavelengths used. The top and bottom row in Fig. 3.3 show the 2.5 % IL and 5 % IL scattering levels, respectively. The left and right columns show the recovered μ_a and μ_s', respectively, as functions of the true μ_a of the medium. In all three reconstructions, the recovered μ_s' showed largest variability while all three approaches consistently tracked linear recovery of μ_a. MC-DT showed the best consistency and accuracy for recovery of μ_s', given the constraints placed on reconstructions. The calibrated-DT also consistently tracked (an unchanging) μ_s' but showed a change in slope from true values in μ_a. The free-shift DT method showed considerable crosstalk between t_s and μ_s' (not shown), but this minimally impacted recovery of μ_a.

In general, all of these approaches performed better at the higher scattering level (5 % IL vs 2.5 % IL) in accordance with diffusion theory serving as a better approximation in higher scattering media. Within each scattering level, similar trends and accuracy were observed at the four wavelengths used. In total, the absolute accuracy in recovered μ_a was better (< 4 % points) at

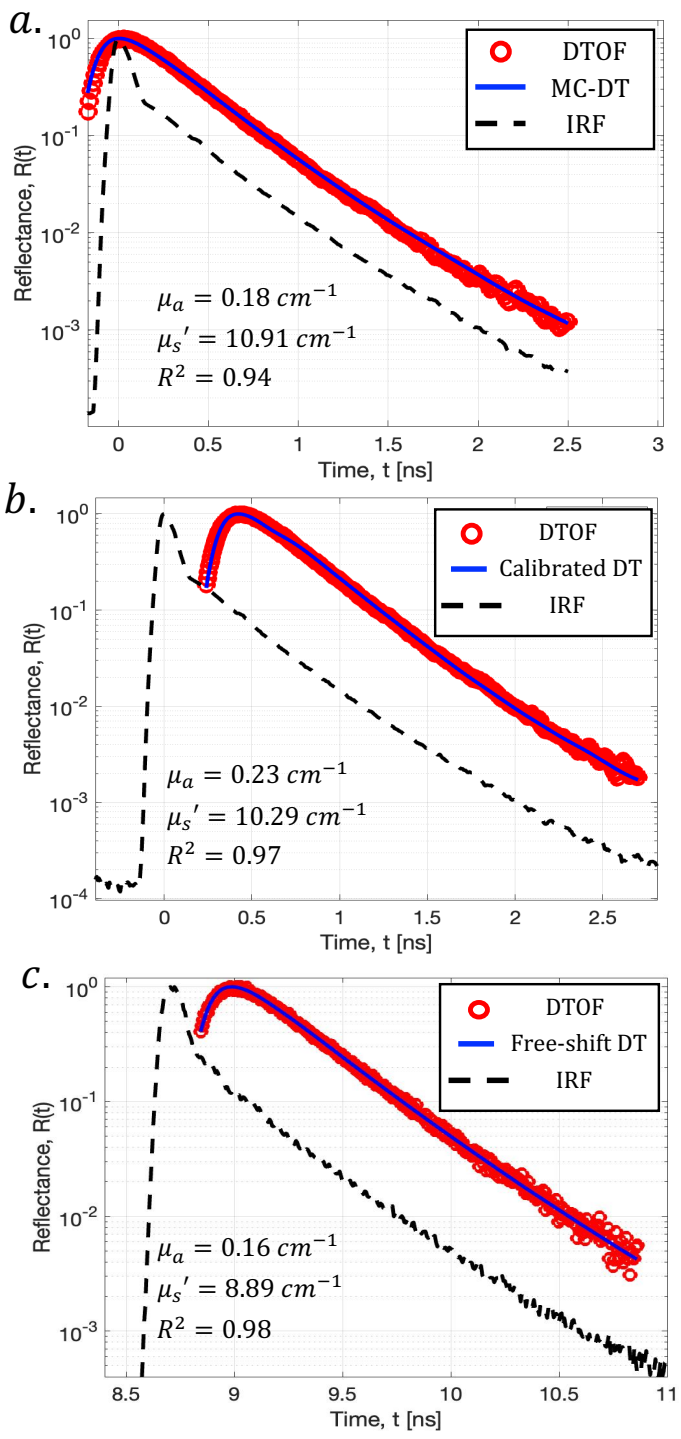

Figure 3.2: Example diffusion theory fits of an experimental DTOF using three different approaches: (a) MC-DT, (b) calibrated DT, and (c) Free-shift DT. The true optical properties are μ_s' = 11.1 cm^{-1} and μ_a = 0.19 cm^{-1}. The recovered optical properties and the sum of squares of the residuals, R^2, for each approach are listed in the figure.

750 nm than 650 nm. However, in the phantoms, the expected absorption values at 650 nm were roughly double those at 750 nm, thus impacting accuracy of DT based analysis. All approaches showed expected linear changes in absorption as shown in Fig. 3.3. The MC-DT and free-shift DT approaches increasingly underestimated μ_a for larger absorption values, whereas the calibrated DT approach systemically overestimated μ_a. Although the free-shift DT approach showed the largest errors in μ_s', this did not appear to significantly affect the recovery of μ_a. In most situations, the free-shift DT approach matched the accuracy of the MC-DT approach in recovering μ_a while being significantly more accurate than the calibrated DT approach.

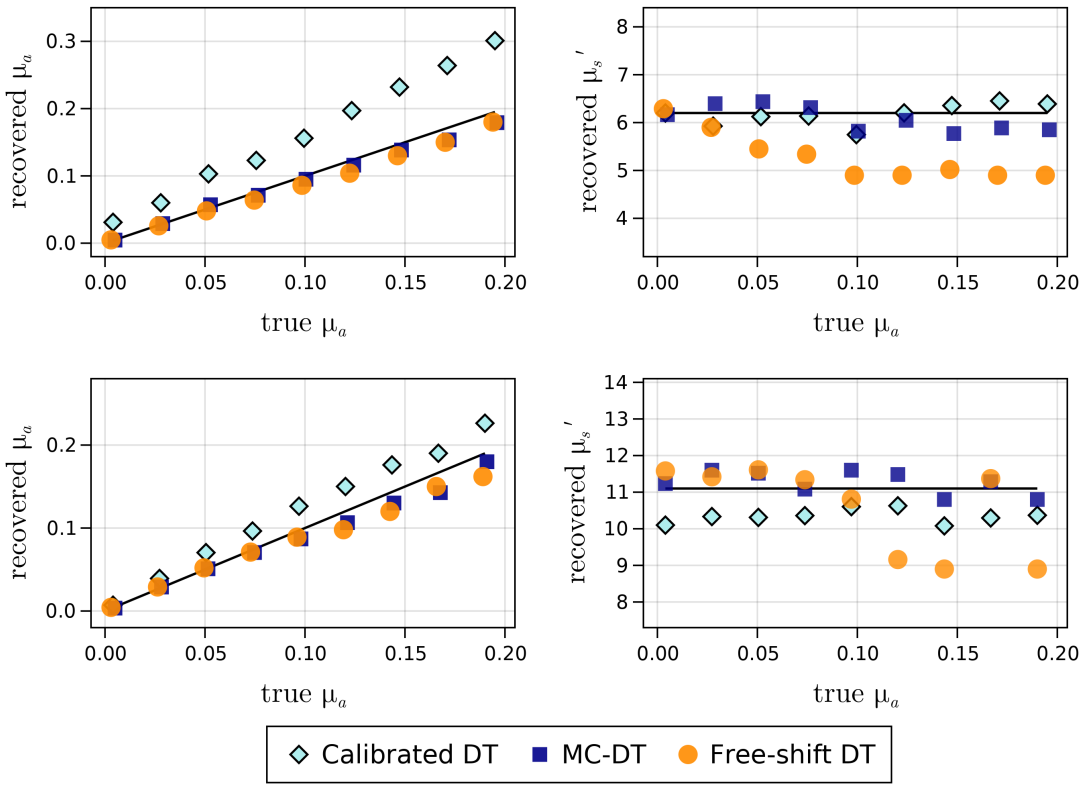

Figure 3.3: Optical properties recovered at the two scattering levels for the 15 mm SDS channel at 700 nm for the three different analysis methods. Each row represents one scattering level for a single wavelength. The left column shows the measured μ_a against the true μ_a while the right column shows the measured μ_s' against the true μ_a for the MC-DT, calibrated DT, and free-shift DT approaches. The MC-DT had the best linearity and recovery of absolute optical properties.

Percent errors in the absorption coefficient were calculated as $\delta_{\mu_a} = 100 \times |\text{true} - \text{measured}|/|\text{true}|$ and shown in Fig. 3.4 for the calibrated DT (sky blue), free-shift DT (orange), and MC-DT (navy) approaches. These values represent the mean δ_{μ_a} across all phantoms and wavelengths used and error bars represent the standard deviation in δ_{μ_a} . Large errors were noted

for short SDS (ρ = 5 mm), displaying the well-known limitation of DT at such distances. The Calibrated and Free-shift DT methods were not statistically different ($p > 0.05$) when ρ = 5 mm. However, all other groups were statistically different ($p < 0.05$) for each SDS when using a post-hoc Tukey HSD test. Errors were at nearly 10 % for ρ = 10 and 15 mm with the MC-DT, which is comparable to ranges reported previously [62]. Free-shift DT was less accurate than MC-DT with δ_{μ_a} of 15-20 % at ρ = 10 and 15 mm . The calibrated DT approach showed the largest mean errors at 40-50 %. Surprisingly, the calibrated DT approach did not show improvements in recovery of absorption when increasing SDS between 10 and 15 mm.

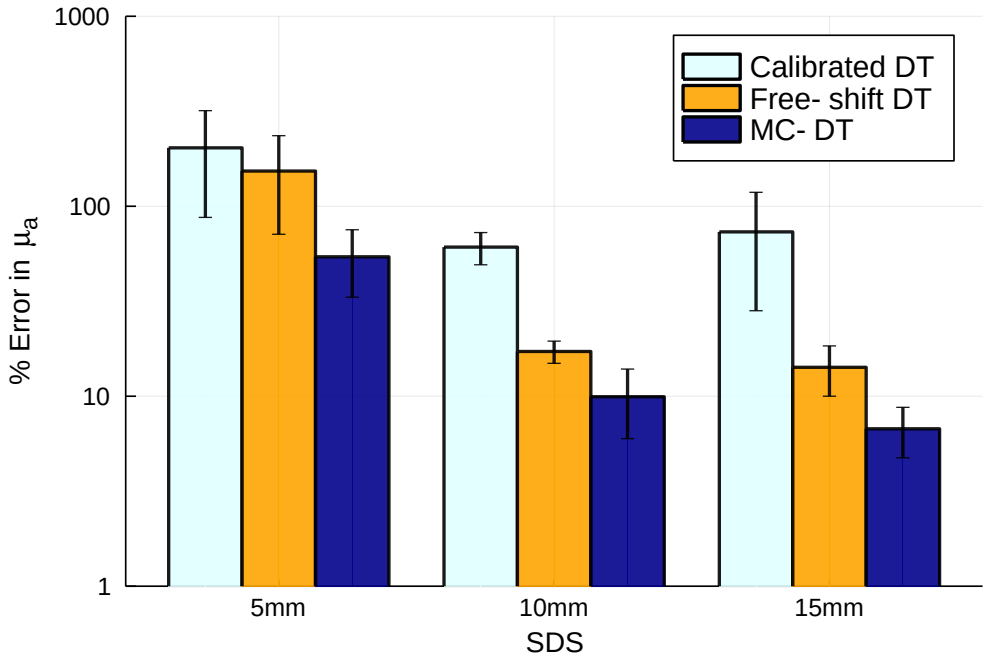

Figure 3.4: Calculated percent error in the recovered absorption coefficient (δ_{μ_a}) using calibrated DT (sky blue), free-shift DT (orange) and MC-DT (navy). δ_{μ_a} is shown for each experimental source-detector separation where error bars represent the standard deviation when averaging across all wavelengths and scattering levels. Large errors are seen when ρ = 5 mm , however δ_{μ_a} is $\approx$ 10 % when ρ = 10 and 15 mm using MC-DT and $\approx 15 - 20$ % using free-shift DT. The MC-DT approach was able to provide more accurate estimates at all SDS and wavelengths.

As noted previously, all approaches performed better at the higher scattering level (5 % IL). Although δ_{μ_a} for the two scattering groups from the MC-DT approach were not significantly different, the calibrated DT approach performed better at the higher scattering level with the free-shift approach performing similarly at each scattering level as shown in Table 3.1. For ρ = 5 mm , accurate recovery of optical coefficients was not possible from any of the approaches. Though somewhat of an improved accuracy was seen in the MC-DT approach when using lower wavelengths (higher

scattering): δ_{μ_a} = 26.1 ± 5.5 at 650 nm compared to δ_{μ_a} = 67.75 ± 6.6 at 800 nm. At ρ = 10 and 15 mm, there was no significant difference between these wavelengths.

Table 3.1: Percent error in recovered absorption coefficients (δ_{μ_a}) at two scattering levels. δ_{μ_a} in the MC-DT approach had a small dependence on scattering level, whereas calibrated DT performed significantly better at the higher scattering level (5 % IL).

SDS	MC-DT		Free-shift DT		Calibrated DT	
	$\delta_a(2.5\%IL)$	$\delta_a(5\%IL)$	$\delta_a(2.5\%IL)$	$\delta_a(5\%IL)$	$\delta_a(2.5\%IL)$	$\delta_a(5\%IL)$
5 mm	52 ± 22	57 ± 20	156 ± 73	143 ± 68	272 ± 131	132 ± 61
10 mm	11 ± 4	9 ± 4	18 ± 6	15 ± 4	58 ± 15	62 ± 11
15 mm	6 ± 2	8 ± 2	15 ± 4	11 ± 4	112 ± 25	35 ± 8

Figure 3.5 shows $\delta_{\mu_s'}$ averaged across all phantoms for the four wavelengths and two scattering levels, at each SDS using calibrated DT (sky blue), free-shift DT (orange), and MC-DT (navy). Recovered $\delta_{\mu_s'}$ was less than 8 % across all wavelengths and SDS using MC-DT with slight improvements at longer SDS: $\delta_{\mu_s'}$ = 5.6 ± 1.5 for ρ = 5 mm and $\delta_{\mu_s'}$ = 3.5 ± 0.8 for ρ = 15 mm . No differences were observed amongst wavelengths within the two scattering levels.

On the other hand, the recovered scattering coefficient using calibrated DT only produced accurate measurements (< 10 %) of μ_s' at ρ = 15 mm . The free-shift DT approach provide reasonable estimates (< 20 %) at both ρ = 10 and 15 mm . The calibrated DT and MC-DT approach were not statistically different ($p > 0.02$) for ρ = 15 mm , however, each of the remaining groups at each SDS were statistically different ($p < 0.001$). Recovered μ_s' values were not directly correlated to estimates of μ_a, as the approaches produced different estimates of μ_s' for similar values of μ_a. This is particularly highlighted in Fig. 3.3 where the free-shift DT and MC-DT approach could produce values of μ_s' 20 % apart, but still yield values of μ_a to within 3 % of each other. Additionally, the increase in the accuracy of μ_s' using the calibrated DT approach at 15 mm did not translate to any increased accuracy in recovery of μ_a, as seen in Fig. 3.4 and Fig. 3.5.

3.5 Discussion

In this work, we compared three methods: 1) MC-DT, 2) Calibrated DT, and 3) Free-shift DT to calculate both the μ_s' and μ_a from experimentally collected DTOFs. These techniques worked without knowledge of the photon launch time t_0. The metric for comparisons was gauged using percent errors of recovered optical properties from DTOFs measured in phantoms relative to their true values. All three approaches could use a system IRF that could be measured in a configuration different from that used to acquire the DTOFs. In other words, all three approaches account for an uncertainty of having a different launch time of the incident photon pulse t_0 from the IRF. The

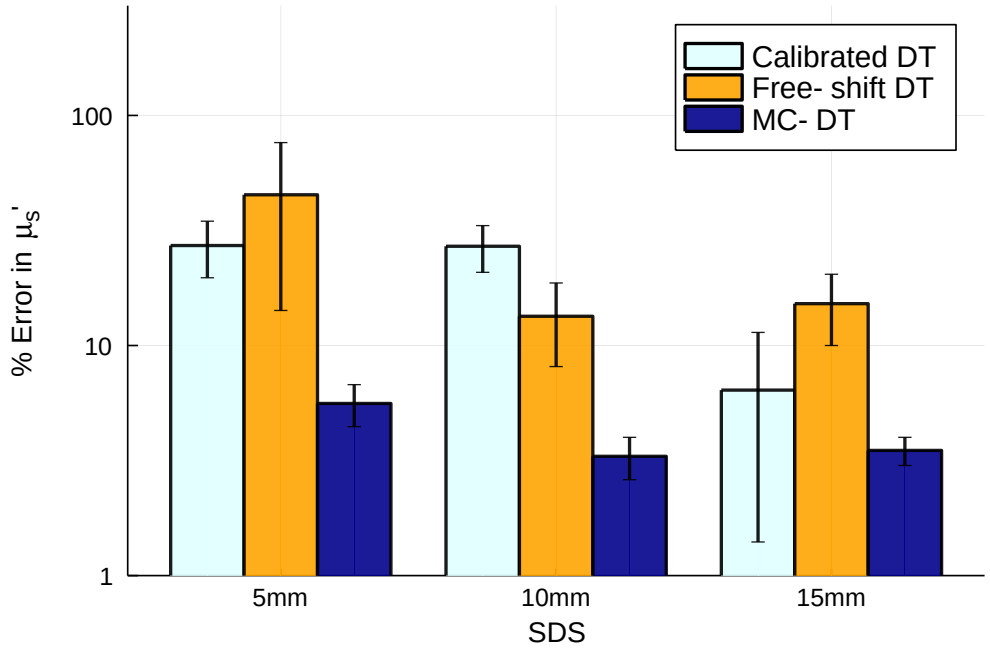

Figure 3.5: Calculated percent error in the recovered reduced scattering coefficient ($\delta_{\mu_s'}$) using calibrated DT (sky blue), free-shift DT (orange) and MC-DT (navy). $\delta_{\mu_s'}$ is shown for each experimental source-detector separation where error bars represent the standard deviation when averaging across all wavelengths and scattering levels. The MC-DT approach was able to produce accurate estimates (< 10 %) for all SDS, while the free-shift DT was able to produce estimates < 20 % when ρ = 10 and 15 mm. Calibrated DT was only able to provide accurate estimates (< 10 %) at ρ = 15 mm.

calibrated and free-shift DT approaches accounted for this uncertainty with a calibration phantom or by introducing a third time-shift t_s parameter in the inverse problem, respectively. The MC-DT approach shifted the IRF and DTOF time scale to peak at t = 0.

In Fig. 3.6, we show the nature of the ill-posed inverse problem in recovering the optical coefficients using the reduced chi-squared (χ^2_R) maps for each method. The χ^2_R maps for each method (MC-DT: Fig. 3.6(a); calibrated DT: Fig. 3.6(b); free-shift DT: Fig. 3.6(c)) were computed for an experimentally measured DTOF from a phantom with expected optical properties μ_s' = 10.2 cm^{-1} and μ_a = 0.17 cm^{-1} at ρ = 15 mm using the three analysis methods over a range of optical coefficients. For the MC-DT and calibrated DT approach, χ^2_R maps are shown as functions μ_a and μ_s'. While, for the free-shift DT approach (Fig. 3.6(c)), we show χ^2_R as a function of all three fitting parameters μ_a, μ_s', and t_s. In both Fig. 3.6(a) and Fig. 3.6(c), we can see the impact of seeking to optimize χ^2_R in the inverse space, when t_0 is unknown. In the MC-DT approach this manifests with χ^2_R showing no well-defined minimum making convergence highly dependent on the initial starting values (or constraints). In the free-shift approach, although a global minimum is present,

it shows the inherent crosstalk between t_s and μ_s'. It also shows why the crosstalk did not significantly impact recovery of μ_a (i.e., the minimum contour mainly runs along the t_s and μ_s' plane). On the other hand, knowing t_0 as with the calibrated DT approach gives a well-defined global minimum (Fig. 3.6(b)). Figure 3.6(a) also demonstrates why a constraint on μ_s' provides stability and therefore improved performance of the MC-DT approach.

Alternatively, as is done with the calibration-DT approach, the temporal position of the IRF can be determined indirectly using reference standard of known optical properties [62]. Although the approach shows clear advantage in the optimization of the inverse problem (Fig. 3.6(b)) it is limited by the accuracy of the calibrated time shift. In our analyses, the calibrated-DT approach systemically overestimated the absorption coefficient which can be explained directly as a consequence of an inaccurate time-shift calibration. These inaccuracies can arise due to differences in the optical properties of the reference phantom, or the method used to determine baseline optical properties for each phantom. In our case, we used commercially given optical properties for the reference solid phantom [18] whereas the Intralipid phantoms were determined from averaged literature values and spectrophotometer measurements. Better results were reported previously for the calibrated-DT based approach [62]. Imposing additional spectral constraints on scattering coefficients when fitting calibrated time-shifts could help improve such estimates.

Introducing a time-shift as a third (free) parameter in the fitting process offers the simplest way to account for uncertainties in t_0. However, this comes at the cost of weakening the fit (Fig. 3.6(c)), increasing computational time and potentially having significant crosstalk between recovered μ_s' and recovered time shifts [131, 36]. In this study, we did not observe notable differences in convergence time across the three methods (all three methods converged < 100 ms). For the free-shift DT approach, we allowed t_s to be shifted by a maximum of 1 ns in the modeled $\tilde{R}(t - t_s)$. Strong crosstalk between t_s and μ_s' were observed that limited the accuracy of recovered μ_s' using this approach. However, it would be possible to further constrain t_s (e.g., for known experimental configurations) that could increase accuracy of recovered μ_s'.

As shown in Fig. 3.6(a), shifting the time scales of the IRF and DTOF to peak at 0 creates a highly ill-posed inverse problem. To overcome this, a constraint on μ_s' was imposed using a previously reported technique [70]. This approach had the best accuracy in recovery of both optical coefficients. Although the performance here was good, some limitations of this technique are to be noted. The maxima of the DTOF has the highest photon count-rates, but the shot-noise contribution in detector-electronics is proportional to $\sqrt{N}$, where N is the count-rate [139]. Thus, determination of the peak time is prone to electronic noise and these could be exacerbated by having different count-rates for different SDS and/or transport coefficients. Further, timing resolutions caused by photon counting jitter, can also vary across detectors. For example, photomultiplier tubes provide timing resolutions larger than 100 ps [138] while superconducting nanowire single-photon detec-

tors can be under 5 ps [87]. Here, SPAD detectors were used and signal acquisition used long integration times (of 30 s) which typically provided timing resolutions of tens of picoseconds [17]. As the peak-time differences measured were much larger than instrument resolution, the approach worked. However, choices of different detectors and timing electronics can significantly impact the MC-DT approach. A similar approach as the MC-DT used here, but based on diffusion theory and using photomultiplier tubes has been reported previously [130]. The MC-DT approach also assumes the DTOF peak-time is equally affected by the IRF at each detecting channel (for the 2 SDS used for the peak-time difference) and thus could impact its extension to multi-channel systems. Finally, the MC-DT approach does not scale well for larger μ_s' as peak-time differences map a larger range of possible μ_s' values which necessitates the use of short SDS channels that limit the sensitivity to only superficial layers [19].

The previous discussion focused on the impact of the temporal shift of the IRF relative to the real system response, and analysis methods to account for such uncertainty. In practice, there are additional sources of error that can impact each of the three approaches. We have used the well-established diffusion approximation to analyze our results, but DT can be severely limited at the SDS studied here and at modelling early arriving photons [131]. We note that reconstructions using DT are strongly influenced by the temporal fit range due to DT not having uniform validity across each photon arrival time. Additionally, the shape of the IRF in addition to the temporal position can greatly impact recovered optical properties. Non-ideal boundary conditions between the DT modelling and the experimental system could also impact results. Specifically, the Calibrated-DT approach had different boundary conditions when collecting measurements on the reference solid phantom (epoxy on resin) compared to the experimental water-based phantoms (epoxy slightly submerged in water). Finally, the influence of using shorter integration times and therefore increasing noise levels in data was not investigated. All of these potential sources of error can impact results.

3.6 Conclusion

We investigated three approaches to overcoming the difficulties in accurately measuring the Instrument Response Function (IRF) in time-resolved reflectance spectroscopy. Particular focus was given to overcoming the uncertainties in measuring the launch time t_0 of the incident photon pulse in reflectance geometries. We compared approaches that (a) operate by shifting the peaks of both the measured DTOFs and theoretical forward model after convolution with the IRF by overlapping them at t = 0, (b) calculate t_0 from a reference standard with known optical properties, and (c) introduce t_s as a fitting parameter in the inverse problem. We find that each approach has a set of unique advantages and shortcomings. When considering the three approaches and their respective

inverse problem, having accurate knowledge of t_0 will provide the most well-posed reconstruction of optical properties (Fig. 3.6(b) vs 3.6(a) and 3.6(c)) leading to more accurate and reliable fitting procedures. As mentioned previously [131, 36], the quantification of μ_s' is more adversely impacted by uncertainties in t_0 than μ_a. We show that recovery of absolute values of optical properties is still possible from time-domain reflectance using IRF measurements that are not exactly calibrated or that become uncalibrated in the presence of instrumental drift over the course of an experiment. Depending on the experimental setup and calibrations employed, accurate results can be achieved with all three methods to varying degrees.

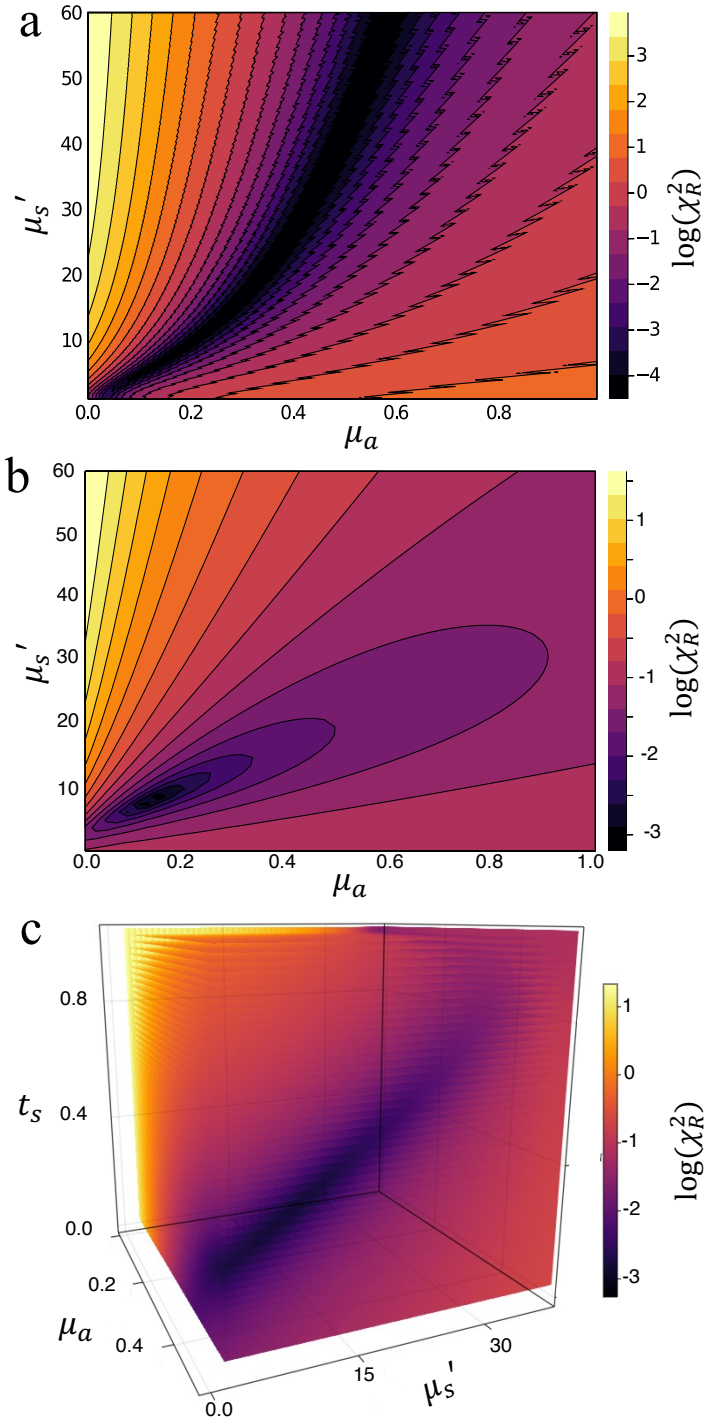

Figure 3.6: χ_R^2 distributions when fitting $\tilde{R}(t)$ to a single DTOF plotted for the three methods: (a) MC-DT, (b) Calibrated DT, and (c) Free-shift DT. A unique minimum is not observed in the MC-DT approach while the calibrated DT approach produces a well-defined minimum. Although the free-shift approach produced a minimum, there is considerable crosstalk between μ_s' and ts.

CHAPTER 4

Efficient Computation of the Steady-State and Time-Domain Solutions of the Photon Diffusion Equation in Layered Turbid Media

This chapter was published in [75]. It discusses light diffusion in a layered cylinder with an arbitrary number of layers. Particular focus is given on the numerical implementation of the solution in terms of accuracy and speed. The validity of the diffusion approximation in layered media is tested against Monte Carlo in three tissue geometries. This article was prepared in collaboration with Samantha Zerafa, Dr. Karthik Vishwanath, and Dr. Mary-Ann Mycek.

4.1 Abstract

Accurate and efficient forward models of photon migration in heterogeneous geometries are important for many applications of light in medicine because many biological tissues exhibit a layered structure of independent optical properties and thickness. However, closed form analytical solutions are not readily available for layered tissue-models, and often are modeled using computationally expensive numerical techniques or theoretical approximations that limit accuracy and real-time analysis. Here, we develop an open-source accurate, efficient, and stable numerical routine to solve the diffusion equation in the steady-state and time-domain for a layered cylinder tissue model with an arbitrary number of layers and specified thickness and optical coefficients. We show that the steady-state (< 0.1 ms) and time-domain (< 0.5 ms) fluence (for an 8-layer medium) can be calculated with absolute numerical errors approaching machine precision. The numerical implementation increased computation speed by 3 to 4 orders of magnitude compared to previously reported theoretical solutions in layered media. We verify our solutions asymptotically to homogeneous tissue geometries using closed form analytical solutions to assess convergence and numerical accuracy. Approximate solutions to compute the reflected intensity are presented which can decrease the computation time by an additional 2-3 orders of magnitude. We also compare our

solutions for 2, 3, and 5 layered media to gold-standard Monte Carlo simulations in layered tissue models of high interest in biomedical optics (e.g. skin/fat/muscle and brain). The presented routine could enable more robust real-time data analysis tools in heterogeneous tissues that are important in many clinical applications such as functional brain imaging and diffuse optical spectroscopy.

4.2 Introduction

Optical properties can be used as indicators of pathological and physiological conditions of biological tissue [80, 171]. Accurate quantitation of these properties from experimental measurements depend on analytical models that need to account for the structural complexity of the tissue system. Therefore, it is important to consider the optical heterogeneity of biological tissues, which are usually approximated as optically homogeneous to facilitate data analysis [153, 51]. Experimentally, light propagation measurements are made by illuminating the tissue surface with either a continuous, frequency modulated, or pulsed light source and collecting measurements of the scattered light after it has propagated through the tissue medium [110, 70]. Measured optical signals are translated into absorption and scattering properties of the medium by utilizing an appropriate forward model of light transport that best represents the measured data [175, 72].

Light propagation in random media such as biological tissues is theoretically modeled using the Radiative Transfer Equation (RTE) [123, 4, 52]. Due to the highly scattering nature of these media, the RTE can be reduced to the diffusion equation, which gives analytical solutions in homogeneous, semi-infinite, or infinite slab geometries [30, 85]. The RTE can also be solved by the Monte Carlo method which remains the gold-standard approach to calculate light transport in media with complex geometries [113] but is computationally expensive [191]. Although parallel implementations have significantly decreased the computational time of forward Monte Carlo simulations down to several seconds [50, 49, 188, 183], they still broadly remain non-viable as inverse solvers to obtain optical properties from experimental measurements in real-time (¡ 1 second) which require thousands of forward simulations at different modelling parameters [50, 188].

Theoretical approaches that account for structural complexity in tissues provide improved reconstruction of optical properties using diffuse optical measurements when studying brain hemodynamics [31]. Although Monte Carlo methods can simulate light propagation in realistic head geometries derived from magnetic resonance imaging (MRI) data [50], modeling the head as layered homogeneous slabs, each with their own set of optical properties, provided similar accuracy in reconstruction of optical properties [153]. Further, diffuse optical measurements are applicable to various parts of the body that exhibit a layered structure (e.g. skin over top muscle, scalp and skull surrounding brain tissue). Therefore, an accurate, versatile and efficient analytical approach to model spatially and/or temporally resolved diffuse reflectance in layered media would enhance

optical property reconstructions from diffuse optical measurements obtained in such layered media *in vivo*. [153].

Several methods to solve the diffusion equation for layered media have been reported in literature by using integral transforms [104, 103, 102, 86], method of images [166], eigenfunctions [111, 112], or finite differences [8]. These methods do not give closed-form expressions directly in the spatial or time-domains for the photon fluence. Instead, the fluence in real-space is computed using numerical transforms [86] or root-finding techniques [111] which tend to increase numerical errors and computational costs [184]. For example, the integral transform approach [86] solves the diffusion equation in the spatial-frequency domain which then must be inverse space-transformed (e.g. 2-D inverse Fourier) for real-space calculations. An additional inverse time Fourier transform is required for computation in the time-domain [86]. Both of these transforms make calculations of the steady-state and time-domain solutions difficult to compute for a wide range of optical and geometrical inputs [86, 104]. Other approaches have been developed to compute geometries with large layer thicknesses and high scattering coefficients and/or spatial frequencies but rely on approximations [59, 84, 83, 104]. Given these challenges, the fastest reported computational times for time-domain fluence in multi-layered media range between 0.5-5 seconds, depending on the number of layers and numerical accuracy required [176, 102, 111, 59]. Such computational performance would preclude direct use of such layered analytical solutions for real-time analysis as optimization of multiple parameters in layered media would take several minutes [60].

In this report, we present an accurate and efficient procedure for computing the photon fluence in a layered cylinder using solutions to the diffusion equation [102]. Our code is open-source and well documented for ease of use. We overcome the computational difficulties noted above by modifying the solutions [102] in the spatial-frequency domain for numerical stability, which allows for computation of arbitrarily sized inputs without approximations. Lastly, we use an inverse Laplace transform for better convergence in the time-domain which improved the numerical accuracy while decreasing the computational cost by several orders of magnitude [106, 177]. Below we describe: (a) implementation of the numerical solutions in the steady-state and time-domain for diffuse optical reflectance and transmittance measurements in N-layered media, (b) verification of the numerical accuracy and stability of the approach in calculating photon fluence for several source-detector configurations and tissue models, and (c) validation by direct comparisons to Monte Carlo simulations of fluence in multi-layered tissue models.

4.3 Theory

We use the integral transform approach [102] to solve the diffusion equation for a N-layered cylindrical model as shown in Fig. S4.1. A collimated source-beam is approximated by an isotropic

point source located at a distance of $z_0 = 1/\mu'_{s1}$ from the location of incidence of the beam and boundary with μ'_{s1} representing the reduced scattering coefficient in the first layer.

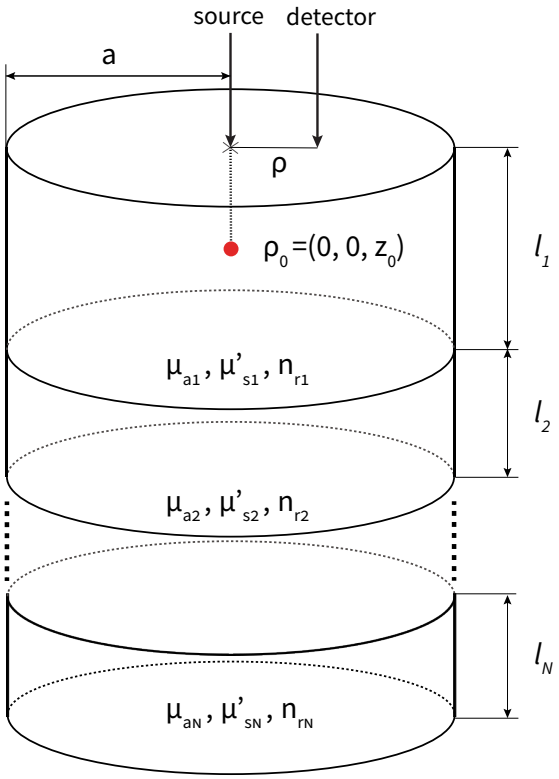

Figure 4.1: Schematic of the $N-$layered turbid medium with a source located onto the center of the cylinder top.

The steady-state diffusion equation can be given by

$$D\nabla^2\Phi(\vec{r}) - \mu_a\Phi(\vec{r}) = -S(\vec{r}) \tag{4.1}$$

where Φ, $D = 1/(3\mu'_s)$, and μ_a denote the fluence rate, the diffusion coefficient, and the absorption coefficient, respectively [102].

The source function $S(\vec{r})$ can be expressed as a Dirac delta function in cylindrical coordinates. Eq. 4.1 can then be rewritten in cylindrical coordinates as

$$\frac{\partial^2}{\partial\rho^2}\Phi + \frac{1}{\rho}\frac{\partial}{\partial\rho}\Phi + \frac{1}{\rho^2}\frac{\partial^2}{\partial\phi^2}\Phi + \frac{\partial^2}{\partial z^2}\Phi - \frac{\mu_a}{D}\Phi = -\frac{1}{D\rho}\delta(\rho-\rho_0)\delta(\phi-\phi_0)\delta(z-z_0) \tag{4.2}$$

with the abbreviation $\Phi = \Phi(\rho, \phi, z)$. The derivative with respect to ϕ in Eq. 4.2 can be elimi-

nated using a cosine transform and then reduced to an ordinary differential equation by using the finite Hankel transform of m^{th} order [101]. These two transforms can be expressed together by [102]

$$\Phi(s_n, \phi, m) = \int_0^{2\pi} \int_0^{a'} \rho \Phi(\rho, \phi') J_m(s_n \rho) \cos(m(\phi - \phi'))\, d\rho\, d\phi' \tag{4.3}$$

using an extrapolated boundary condition at $\rho = a'$ for the upper limit of the integral transform with $a' = a + z_{b1}$ where a is the radius of the cylinder. The extrapolation length can be calculated with $z_{bk} = 2AD_k$ where A is proportional to the fraction of photons that are internally reflected at the boundary [30]. The subscript k signifies the k^{th} layer of the cylinder with distinct absorption μ_{ak} and scattering μ'_{sk} in each layer. Applying Eq. 4.3 to Eq. 4.2 yields an ordinary differential equation

$$\frac{\partial^2}{\partial z^2}\Phi - (\frac{\mu_a}{D} + s_n^2)\Phi = -\frac{1}{D} J_m(s_n \rho_0) \cos(m(\phi - \phi_0))\delta(z - z_0) \tag{4.4}$$

for $\Phi = \Phi(s_n, \phi, m, z)$ after applying a finite Hankel transform relation [101]. J_m is the Bessel function of first kind and order m and each s_n is determined from the roots of J_m such that $J_m(a' s_n) = 0, \quad n = 1, 2, ...,$.

A Green's function approach is used solve Eq. 4.4 for the fluence in a specific layer assuming that the isotropic source (from an incident pencil beam) is located within the first layer ($0 \leq z_0 < l_1$). We then seek separate Green's functions in each layer where the solution for the first layer $G_1(s_n, z)$ is composed of a homogenous and particular part while the solutions for the remaining k layers have only a homogeneous solution. Therefore, the Green's function $G_1(s_n, z)$ in the top layer becomes

$$\frac{\partial^2}{\partial z^2} G_1(s_n, z) - \alpha^2 G_1(s_n, z) = -\frac{1}{D_1}\delta(z - z_0) \tag{4.5}$$

when z is within the first layer $0 \leq z < l_1$. For the N^{th} layer, $G_N(s_n, z)$ becomes

$$\frac{\partial^2}{\partial z^2} G_N(s_n, z) - \alpha^2 G_N(s_n, z) = 0 \tag{4.6}$$

when z is located in the bottom layer $\sum_{k=1}^{N-1} l_k \leq z < \sum_{k=1}^{N} l_k$. These equations can be used to reduce Eq. 4.4 to

$$\Phi_k(s_n, \phi, m, z) = G_k(s_n, z) J_m(s_n \rho_0) \cos(m(\phi - \phi_0)) \tag{4.7}$$

We use the boundary conditions previously described [102] but provide solutions for $G_1(s_n, z)$ and $G_N(s_n, z)$ purely in terms of exponentially decaying functions. This form of expression pro-

vides stability in numerical calculations and is in contrast to previously derived expressions [102] which contain hyperbolic trigonometric functions that can easily produce overflow-errors. We also note that the solutions we derive are exact and do not require any approximations for calculation, as is required by previous reports [59, 104, 84]. Expanding hyperbolic functions as exponentials also allows for simplifying several other terms that serve to reduce the computational time.

The Green's function G_1 in the first layer $(0 \leq z < l_1)$ is given by

$$G_1(s_n, z) = \frac{e^{-\alpha_1|z-z_0|} - e^{-\alpha_1(z+z_0+2z_{b1})}}{2D_1\alpha_1} + \frac{e^{\alpha_1(z+z_0-2l_1)}(1-e^{-2\alpha_1(z_0+z_{b1})})(1-e^{-2\alpha_1(z+z_{b1})})}{2D_1\alpha_1} \times \frac{D_1\alpha_1 n_1^2\beta_3 - D_2\alpha_2 n_2^2\gamma_3}{D_1\alpha_1 n_1^2\beta_3(1+e^{-2\alpha_1(l_1+z_{b1})}) + D_2\alpha_2 n_2^2\gamma_3(1-e^{-2\alpha_1(l_1+z_{b1})})} \tag{4.8}$$

where $\alpha_k = \sqrt{\mu_{ak}/D_k + s_n^2}$. In general, the quantities β_3 and γ_3 are obtained by downward recurrence relations with start values

$$\begin{aligned} \beta_N &= D_{N-1}\alpha_{N-1}n_{N-1}^2(1+e^{-2\alpha_{N-1}l_{N-1}})(1-e^{-2\alpha_N(l_N+z_{b_2})}) \\ &\quad + D_N\alpha_N n_N^2(1-e^{-2\alpha_{N-1}l_{N-1}})(1+e^{-2\alpha_N(l_N+z_{b_2})}) \\ \gamma_N &= D_{N-1}\alpha_{N-1}n_{N-1}^2(1-e^{-2\alpha_{N-1}l_{N-1}})(1-e^{-2\alpha_N(l_N+z_{b_2})}) \\ &\quad + D_N\alpha_N n_N^2(1+e^{-2\alpha_{N-1}l_{N-1}})(1+e^{-2\alpha_N(l_N+z_{b_2})}) \end{aligned} \tag{4.9}$$

with the downward recurrence given by

$$\begin{aligned} \beta_{k-1} &= D_{k-2}\alpha_{k-2}n_{k-2}^2(1+e^{-2\alpha_{k-2}l_{k-2}})\beta_k + D_{k-1}\alpha_{k-1}n_{k-1}^2(1-e^{-2\alpha_{k-2}l_{k-2}})\gamma_k \\ \gamma_{k-1} &= D_{k-2}\alpha_{k-2}n_{k-2}^2(1-e^{-2\alpha_{k-2}l_{k-2}})\beta_k + D_{k-1}\alpha_{k-1}n_{k-1}^2(1+e^{-2\alpha_{k-2}l_{k-2}})\gamma_k \end{aligned} \tag{4.10}$$

We note that we seek just the terms β_3 and γ_3 which must be determined recursively if the total number of layers N is larger than 3. In that case, Eq. 4.9 is used to generate starting values in the recurrence relation, then Eq. 4.10 is used recursively until β_3 and γ_3 are obtained. If $N = 2$, $\beta_3 = 1 - e^{-2\alpha_2(l_2+z_{b2})}$ and $\gamma_3 = 1 + e^{-2\alpha_2(l_2+z_{b2})}$. For $N = 3$, only Eq. (4.9) is needed to calculate β_3 and γ_3.

The solution to Eq. 4.6 for G_N is

$$G_N(s_n, z) = \frac{n_N^2 2^{N-2}\prod_{i=2}^{N-1}(D_i\alpha_i n_i^2)\exp(\alpha_1(z_0-l_1) + \alpha_N(L_N + z_{bN} - z) - \xi_2)}{D_1\alpha_1 n_1^2\beta_3(1+e^{-2\alpha_1(l_1+z_{b1})}) + D_2\alpha_2 n_2^2\gamma_3(1-e^{-2\alpha_1(l_1+z_{b1})})} \tag{4.11}$$

The quantity ξ_2 is computed with start values $\xi_N = \alpha_N(l_N + z_{b2})$ and with downward recurrence relations $\xi_{k-1} = \xi_k + \alpha_{k-1}l_{k-1}$ such that for $N = 2$, $\xi_2 = \alpha_2(l_2 + z_{b2})$ and for $N = 3$, $\xi_2 = \alpha_2 l_2 + \alpha_3(l_3 + z_{b2})$ and so on. We note that our routine has unrolled these relations completely for $N = 4$ to improve performance.

For solutions in real-space, $\Phi(\rho, z)$ we apply the inverse relation of Eq. 4.3 to Eq. 4.7 such that the fluence in real space can be written as [102]

$$\Phi_k(\rho, z) = \frac{1}{\pi a'^2} \sum_{n=1}^{\infty} G_k(s_n, z) J_0(s_n \rho) J_1^{-2}(a' s_n) \tag{4.12}$$

for the special case of a point source that is incident at the center top of the cylinder.

Solutions in the time-domain

Given a sinusoidally modulated source at frequency f, the real and imaginary parts of the fluence $\Phi(\rho, \omega)$ can be calculated using the same formula for $\Phi(\rho)$ and adding a complex absorption term [86]

$$\alpha_k = \sqrt{\mu_{ak}/D_k + s_n^2 + i\omega/(D_k c)} \tag{4.13}$$

where c is the speed of light in the medium and $i = \sqrt{-1}$. The real and imaginary parts are used to calculate the phase angle and modulation.

For solutions in the time-domain, the real and imaginary parts of the fluence in the frequency domain must be calculated at many frequencies (400-4,000x) [106, 86] and inverse Fourier transformed into the time-domain [101]. The Fourier integral is slowly converging and the number of frequency evaluations needed is highly dependent on ρ, μ_s' and t [106].

Alternately, an inverse Laplace transform can be applied to Eq. 4.12 [106, 177] by making the substitution $i\omega \rightarrow \bar{s}$ in Eq. 4.13 and numerically integrating the Bromwich complex contour integral

$$f(t) = \frac{1}{2\pi i} \int_B e^{\bar{s}t} F(\bar{s})\, d\bar{s} \tag{4.14}$$

In Eq. 4.14, B denotes the Bromwich path where $\bar{s}$ is a complex number along the contour. We note we use a bar $\bar{s}$ to avoid confusion with s_n. The corresponding solution for the time-domain fluence is then

$$\Phi_k(\rho, t) = \frac{1}{\pi a'^2} \sum_{n=1}^{\infty} \frac{1}{2\pi i} \left[\int_B e^{\bar{s}t} G_k(s_n, z, \bar{s})\, d\bar{s} \right] \times J_0(s_n \rho) J_1^{-2}(a' s_n) \tag{4.15}$$

The Bromwich line can be deformed into a Hankel contour that begins and ends in the left half-plane, such that $Re\, z \rightarrow -\infty$ [177]. On such a contour, the exponential in Eq. 4.14 ensures that the integrand decays rapidly and renders the integral well-suited for approximation using a simple trapezoidal rule. We utilized a hyperbola countour [177] parameterized by $s(\theta) = \mu + i\mu \sinh(\theta + im\varphi)$ where $s'(\theta) = i\mu \cosh(\theta + i\varphi)$ to evaluate the time-domain solutions. For non-complex

time-domain signals, application of the midpoint rule gives:

$$f(t) = \frac{h}{\pi}\left[\sum_{k=0}^{N-1} F(\bar{s}_k)\exp(\bar{s}_k t)\bar{s}'_k\right] \tag{4.16}$$

where $\bar{s}_k = \bar{s}(\theta_k)$ for $\theta_k = (k+1/2)h$ and h being the uniform node spacing with N being the number of nodes along the hyperbola in the upper half-plane $Re(s) > 0$.

The parameters μ and φ as well as node spacing h are obtained for computing $f(t)$ across many time values in $t \in (t_1, t_2)$ by considering a single (fixed) integration path for all time values. The time-independent parameters are expressed by:

$$\mu = \frac{4\pi\varphi - \pi^2}{A(\varphi)}\frac{N}{t_2} \tag{4.17}$$

$$A(\varphi) = \operatorname{arcosh}\left[\frac{(\pi - 2\varphi)\Lambda + 4\varphi - \pi}{(4\varphi - \pi)\sin\varphi}\right] \tag{4.18}$$

where $\Lambda = t_2/t_1$. The uniform node spacing becomes $h = A(\varphi)/N$ with the previously optimized [106] parameter $\varphi = 1.09$.

Approximate solutions for z ≈ z$_0$

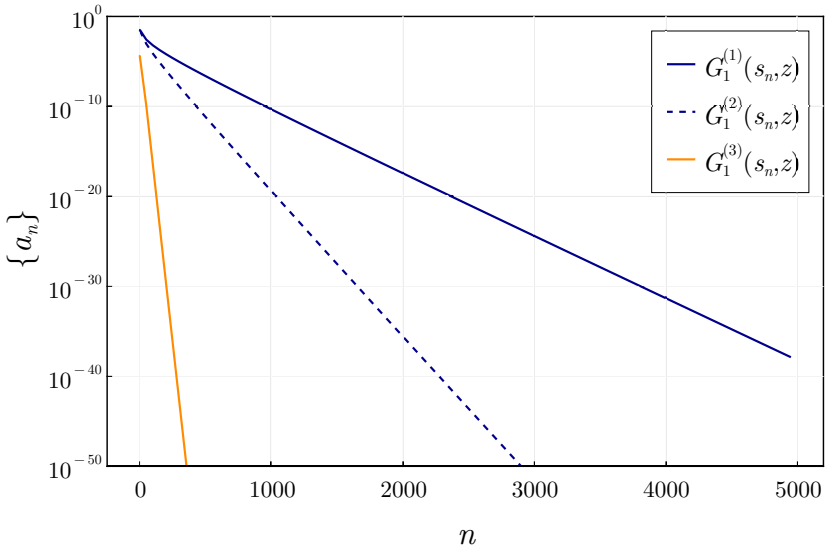

Figure 4.2: We show the convergence of three separate terms in Eq. 4.8 by showing the value of the n^{th} term in the sequence when summing over $j_{0,n}$. Each term converges at a much different rate with the overall convergence being highly dependent on μ'_{s1} when $z = 0$.

A limitation of computing $\Phi_1(\rho, z)$ using $G_1(s_n, z)$ in Eq. 4.8 is the slow convergence when $z \approx z_0$. This is of particular importance for reflectance measurements when we must compute $\Phi_1(\rho, z)$ when $z = 0$. Unfortunately, when $z = 0$ and μ'_{s1} is large, the routine is limited by slow convergence requiring thousands of terms in Eq. 4.12. The convergence of Eq. 4.12 for $\Phi_1(\rho, z)$ can be analyzed by separating Eq. 4.8 into three terms

$$G_1^{(1)}(s_n, z) = \frac{e^{-\alpha_1|z-z_0|}}{2D_1\alpha_1} \tag{4.19}$$

$$G_1^{(2)}(s_n, z) = \frac{-e^{-\alpha_1(z+z_0+2z_{b1})}}{2D_1\alpha_1} \tag{4.20}$$

$$\begin{aligned} G_1^{(3)}(s_n, z) = &\frac{e^{\alpha_1(z+z_0-2l_1)}(1-e^{-2\alpha_1(z_0+z_{b1})})(1-e^{-2\alpha_1(z+z_{b1})})}{2D_1\alpha_1} \\ &\times \frac{D_1\alpha_1 n_1^2\beta_3 - D_2\alpha_2 n_2^2\gamma_3}{D_1\alpha_1 n_1^2\beta_3(1+e^{-2\alpha_1(l_1+z_{b1})}) + D_2\alpha_2 n_2^2\gamma_3(1-e^{-2\alpha_1(l_1+z_{b1})})} \end{aligned} \tag{4.21}$$

where $G_1(s_n, z) = G_1^{(1)}(s_n, z) + G_1^{(2)}(s_n, z) + G_1^{(3)}(s_n, z)$. In Fig. S4.2, we show the value of the three terms a_n as we iterate over the n^{th} root of $j_{0,n}$. Here, we show a specific example when $\mu'_{s1} = 20$ cm^{-1}, $\mu'_{s2} = 15$ cm^{-1}, $\mu_{a1} = 0.1$ cm^{-1}, $\mu_{a2} = 0.2$ cm^{-1}, $a = 10$ cm, $l_1 = 0.5$ cm, and $l_2 = 5$ cm. We can see that $G_1^{(3)}(s_n, z)$ is rapidly decaying and just a few terms are needed for accurate computation. It should also be noted that this term is the only term affected by the optical properties of deeper layers $k \geq 2$ and therefore the dominate convergence of Eq. 4.8 is only affected by the optical properties of the first layer. However, because the three terms decay at such a different rate, for the highest numerical accuracy it is recommended to sum these terms separately and combine them once the infinite sum is terminated. As we can see, the convergence is dominated by the slow decay of $G_1^{(1)}(s_n, z)$ when $z = 0$. This convergence becomes slower as μ'_{s1} becomes larger.

However, when $z \approx z_0$ we can sum the particular solution $G_1^{(1)}(s_n, z)$ over n exactly in closed form yielding the infinite space Green's function caused by an isotropic point source. This allows us to write the fluence $\Phi_1(z \approx z_0)$ as

$$\Phi_1(\rho) = \frac{e^{-\kappa_1|\boldsymbol{r}|}}{4\pi D_1|\boldsymbol{r}|} + \Phi_1^{(h)}(\rho) \tag{4.22}$$

where $\boldsymbol{r} = \sqrt{\rho^2 + (z-z_0)^2}$ and $\kappa_1 = \sqrt{\mu_{a1}/D_1}$. The first term in Eq. 4.22 is the infinite space Green's function. The homogenous part $\Phi_1^{(h)}(\rho)$ can be computed with Eq. 4.12 and $G_1^{(h)}(s_n, z)$ computed with $G_1(s_n, z) = G_1^{(2)}(s_n, z) + G_1^{(3)}(s_n, z)$. We note that this solution is only approximate if we want to consider the fluence on the boundary $z = 0$, but to calculate the fluence inside the first layer when $z = z_0$ it represents the exact solution. This significantly reduces the number

of terms needed in Eq. 4.12, however $G_1^{(2)}(s_n, z)$ now limits the overall convergence rate which also decays at a slow rate when $z = 0$ and for increasing μ'_{s1}. However, a similar approximation can be made which allows for the exact summation of $G_1^{(1)}(s_n, z)$ + $G_1^{(2)}(s_n, z)$ in closed form which represents the steady-state solution for a semi-infinite medium. Therefore, it is appropriate to rewrite the fluence as

$$\Phi_1(\rho, z = 0) \approx \Phi^{SI}(\rho, z) + \frac{1}{\pi a'^2} \sum_{n=1}^{\infty} G_1^{(3)}(s_n, z) J_0(s_n \rho) J_1^{-2}(a' s_n) \tag{4.23}$$

where $\Phi^{SI}(\rho, z)$ is the steady-state fluence in a semi-infinite medium (Equation 3 given in Kienle and Patterson [85]). The optical properties of $\Phi^{SI}(\rho, z)$ are that of the first layer (μ'_{s1}, μ_{a1}). We test this approximation in Fig. S4.3 as a function of μ'_{s1} and ρ by summing $G_1^{(1)}(s_n, z) + G_1^{(2)}(s_n, z)$ for $n = 50,000$ in octuple precision using Eq. 4.12 and comparing the absolute and relative errors to the closed form semi-infinite Green's function. Each of these forms only contain terms that represent the top layer optical properties (μ'_{s1}, μ_{a1}). In Fig. S4.4, we compare the approximation to the exact solution for two tissue models: (a) μ'_{s1} = 10 cm^{-1}, μ'_{s2} = 13 cm^{-1}, μ_{a1} = 0.1 cm^{-1}, and μ_{a2} = 0.2 cm^{-1} and (b) μ'_{s1} = 60 cm^{-1}, μ'_{s2} = 40 cm^{-1}, μ_{a1} = 0.01 cm^{-1}, and μ_{a2} = 0.08 cm^{-1}. We use the same layer thicknesses, $l_1 = 1$ and $l_2 = 5$ cm with a cylinder radius of 20 cm.

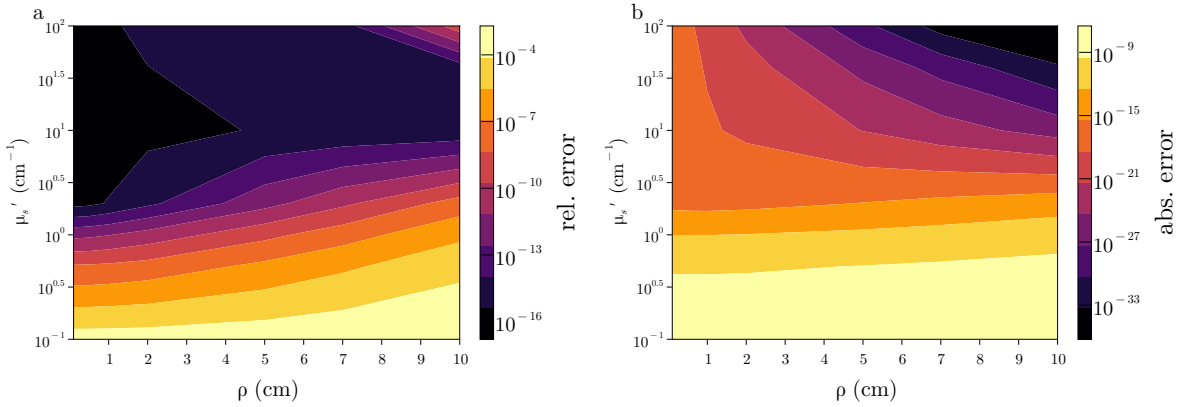

Figure 4.3: The (left) relative and (right) absolute error between the closed-form semi-infinite Green's function and $G_1^{(1)}(s_n, z) + G_1^{(2)}(s_n, z)$ when summed over 50,000 terms using Eq. 4.12. This approximation also gives absolute errors below the machine precision in double precision calculations when $\mu'_{s1} > 2\ \mathrm{cm}^{-1}$.

Theoretically, this solution becomes more accurate when $z = 0$ as $\mu'_{s1} \to \infty$. We find this approximation to be accurate for relative errors greater than 10^{-14} for $\mu'_{s1} > 2\ \mathrm{cm}^{-1}$ which is within the relative errors provided by the exact forms when double precision arithmetic is used.

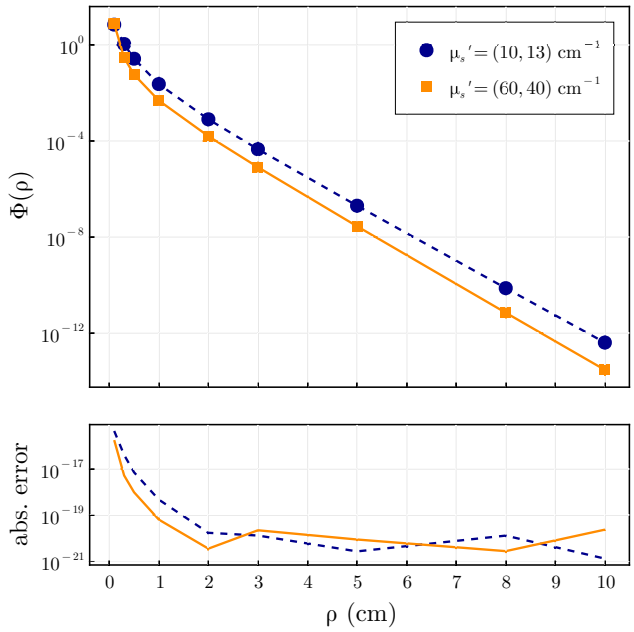

Figure 4.4: Shows the steady-state fluence calculated with the semi-infinite space Green's function (markers) compared to summing $G_1^{(1)}(s_n, z) + G_1^{(2)}(s_n, z)$ exactly using Eq. 4.12 (lines) for two different tissue geometries. The absolute error is shown in the below plot displaying that these solutions give absolute errors below the machine precision in double precision calculations. The solutions were computed in octuple precision for accurate comparison.

Even for very low $\mu_{s1}' = 0.1$ cm^{-1}, this approximation can give at least 3 digits of accuracy. The advantage of this approach is that just 150 roots were used in the approximate form when $\mu_s' = (10, 13)$ cm^{-1} where 3,500 roots were needed in the exact form. When $\mu_s' = (60, 40)$ cm^{-1} the approximation only needed 200 roots at all values of ρ compared to 20,000 roots required in the exact form. However, if only a couple digits of accuracy are needed the approximate form can give reasonable convergence in less than 50 roots even for very large scattering coefficients. This results in computational times being 2-3 orders of magnitude faster allowing for computation in less than one microsecond for a wide range of optical properties. Therefore, it is highly recommended to use such an approximation for $\mu_{s1}' > 2$ cm^{-1}.

Computational details

To efficiently compute Eq. 4.12, it is important to optimize the three terms, $G_k(s_n)$, $J_0(s_n\rho)$, $J_1^{-2}(a's_n)$. First, s_n must be determined such that $J_0(a's_n) = 0, \quad n = 1, 2, ...,$. Calculating these roots at runtime is expensive. Instead, s_n should be calculated from the precomputed roots of J_0 using the relation $s_n = j_{0,n}/a'$ where $j_{0,n}$ is the n^{th} root of $J_0(x)$. It

is then possible to remove the runtime computation of $J_1^{-2}(a's_n)$ because $a's_n = j_{0,n}$, therefore, $J_1^{-2}(j_{0,n})$ is constant and can be precomputed. A table of $j_{0,n}$ and $J_1^{-2}(j_{0,n})$ are computed up to $n = 1,000,000$ and are loaded for use during precompilation. Now, the runtime is directly proportional to the time it takes to compute $G_k(s_n)$ and $J_0(x)$. It appears that the Green's function term is the most expensive when looking at Eq. 4.8, but calls to an external special function library within a hot loop can be costly. To assess the computational cost of computing $J_0(x)$, Eq. 4.12 was timed using $n = 5,000$ before and after replacing $J_0(x)$ with $\sin(x)$. It was found that computing $J_0(x)$ instead of $\sin(x)$ took 2.6x as long meaning that the simple computation of $J_0(x)$ accounted for $\approx 58\%$ of the total runtime. The baseline implementation of $J_0(x)$ was provided by fdlibm (https://netlib.org/fdlibm).

For the calculation of $J_0(x)$, a custom optimized routine based on a previously described algorithm [66] was developed. This routine is detailed in the Appendices and can be found at https://github.com/JuliaMath/Bessels.jl. Incorporating this routine instead of using fdlibm decreased the total runtime by $\approx 54\%$. We note that the custom routine and the algorithm provided by fdlibm give similar error tolerances. Additionally, the computation of the Bessel function (in double precision) occurs in two main branches with a cutoff at $x \approx 26$. The asymptotic expansion for large arguments is over twice as fast so the dependence on the total computation on the Bessel function calculation will also be a function of how many terms are considered in the sum. For larger roots, the Bessel function will be computed at larger arguments resulting in much faster calculation compared to smaller roots. Naturally, the roots should be in order to take advantage of branch prediction during the Bessel function calculation for the best speedup. With the new routine, computing $J_0(x)$ in Eq. 4.12 accounts for just $\approx 5\%$ of the total runtime. This optimization is also crucial for fast calculation of the fluence at multiple spatial locations. However, it is important to detail a further optimization if designing the algorithm for a specific experimental system. Typically, the source-detector separation, ρ is fixed and known ahead of time allowing for the product $J_0(s_n\rho)J_1^{-2}(a's_n)$ to be precomputed for several values of ρ by approximating that $a' \approx a$ if the cylinder radius is large which avoids any Bessel function calls during the routine. Additionally, the rounding of $s_n\rho$ during the calculation of $J_0(s_n\rho)$ limits the accuracy of solutions to absolute errors around the machine precision. It could then be beneficial to precompute $J_0(s_n\rho)$ in higher precision to decrease the lower bound error tolerances.

Any optimization of the final term, $G(s_n)$, should be performed while maintaining numerical accuracy. The greatest loss of significance occurs when subtracting values with different magnitudes. Although the expressions are given to maintain numerical stability (i.e., they avoid terms overflowing to infinity), terms like $(1 - \exp(x))$ and $(\exp(-a\alpha) - \exp(-b\alpha))$ can lead to loss of precision. Therefore, it is best to express these in terms of $\exp(x) - 1$ which is typically a built in library function expm1(x) in programming languages. This has the advantage of being more

accurate and faster as it reduces the number of terms to compute and allows for easier use of SIMD instinsincs. Using fastmath flags can also decrease the total runtime by about 10 % in the steady-state and 20 % in the time-domain. These types of optimizations should be done with care to maintain accuracy, but were tested to give identicial results when used to compute $G(s_n)$. Though, they were not used for any results presented or in any benchmarks shown here. The additional gain in using fastmath in the time-domain is the faster complex arithmetic and division where both the spatial and time-domain benefit from a faster instrinsinc $\exp(x)$. Another optimization that was not yet considered is vectorizing the for loop which sums the expression over the Bessel roots. This will require a vectorized version of $J_0(x)$ which was not implemented. However, these types of optimization could result in large speed gains with the availabity of vector math libraries and proper handling of the reduction and termination criteria within the loop.

Verification of numerical algorithm and validation with Monte Carlo

To calculate the steady-state fluence in real space, a finite inverse Hankel transform (equation (4.12)) must be numerically computed. Calculations of solutions in the time-domain requires equation (4.12) to be evaluated at N complex valued absorption terms during the numerical inversion of the Laplace transform in equation (4.15). The numerical accuracy and efficiency of the procedure depend on the convergence and difficulty of computing the two sums. Since both the computation of the steady-state and time-domain fluence depends on equation (4.12), the accuracy and computational speed depend primarily on how many terms n of the infinite sum are retained in equation (4.12). To allow for computation over an arbitrary number of terms we have expanded the hyperbolic functions given previously [102] in terms of exponential functions which also reduces the computational time by simplifying the expressions. Additionally, we have precomputed the roots of J_0 and developed a custom procedure for calculation of $J_0(x)$ which reduces the computational time substantially.

As exact, closed-form solutions for the photon fluence in layered media are not available, we validate our solutions in layered media to closed-form homogeneous solutions for semi-infinite media [85]. In these validations, each layer in our tissue-model was set to have the same optical properties as the homogeneous medium along with large lateral boundaries. This allows us to precisely quantify numerical errors and determine convergence of our solutions in terms of the number of terms retained in the sum in equation (4.12). We first compare equation (4.12) evaluated with 2 and 8 layers of similar optical properties to the semi-infinite solution [85] and to Monte Carlo simulations in a semi-infinite medium. Next, we compare the accuracy of equation (4.12) as a function of the number of terms n considered in the summation for different input parameters μ'_{s1}, μ'_{s2}, μ_{a1}, μ_{a2}, z, and a. The accuracy is compared to the computation when using $n = 50,000$

terms in quadruple precision.

Solutions in the time-domain require computing both the infinite sum in equation (4.12) as well as numerically performing the inverse Laplace transform in equation (4.15). Strategies to invert the Laplace transform could allow for significantly faster convergence compared to the Fourier transform [89, 106], however the obtention of the inverse Laplace transform is not always an easy or even possible task to perform [89]. Therefore, the accuracy of the numerical approach to invert the Laplace transform must be rigorously tested. We focus on two attributes in performing the numerical integration in equation (4.15) that affect both the convergence and numerical accuracy: (a) the number of Laplace space evaluations N used to evaluate the Laplace integral in equation (4.15) and (b) the contour width determined from $\Lambda = t_2/t_1$ where $t \in (t_1, t_2)$. The effect of both of these parameters on the convergence and numerical accuracy are again examined by comparison to closed-form homogeneous analytical solutions. We show the reconstruction of the time-domain signal for high scattering and high absorbing media at short and long distances and times where the numerical reconstruction has been difficult to perform [106, 83]. We have included in Appendix A extended discussion on how to efficiently compute equation (4.12), which also directly affect the computation of equation (4.15), and the advantages compared to other routines [104]. Additionally, we give approximations for reflectance simulations ($z = 0$) that are accurate for double precision arithmetic (see Supplementary Fig. S3) which can decrease the computational time by 2-3 orders of magnitude.

All the numerical routines and figures presented here were developed using the Julia programming language (v1.7.0) [11]. Numerical simulations were performed on a MacBook Pro with an Apple M1 chip (MacOS version 11.1) and 16 GB of memory. Simulations in the steady-state utilized a single core while the inverse Laplace transform in the time-domain used multi-threaded parallelism. Here, the Laplace space evaluations were evenly distributed across the 4 cores and 8 threads of the M1 chip. All benchmarks are done in double precision arithmetic using v0.8.0 of LightPropagation.jl.

To validate the derived analytical solutions, the fluence is compared with results obtained from Monte Carlo simulations. The Monte Carlo method simulates the propagation of photons through the scattering medium using appropriate probability functions and random number generation [50, 191]. In the limit of an infinitely large number of photons used in the simulations, the Monte Carlo method is an exact solution of the RTE [191]. We utilized an independent open-source Monte Carlo code provided by the Virtual Photonics Technology Initiative [67] to validate the layered diffusion theory model. The optical properties used were taken from literature using three biologically relevant tissue models with an isotropic emitting source at a depth of $z_0 = 1/\mu'_{s1}$ and a Henyey-Greenstein phase function. The anisotropic factor was assumed to be $g = 0.8$ for all layers. The Monte Carlo simulations used 5×10^7 photons for each simulation which visually reduced the

effect of stochastic noise for all bin widths in the spatial and time domain. For all comparisons the refractive index of the medium is assumed to be $n_r = 1.4$ where the external medium is assumed to be air $n_r = 1.0$. The fluence as a function of t and/or ρ and z was recorded in discrete bin widths of $\Delta t = 0.02$ ns, $\Delta\rho = 0.99$ mm, and $\Delta z = 0.27$ mm.

4.4 Results

Numerical accuracy of the layered diffusion equation

In Fig. 4.5, the fluence on the top boundary ($z = 0$) in a semi-infinite medium with optical coefficients $\mu_a = 0.1\ \mathrm{cm}^{-1}$, $\mu_s' = 10\ \mathrm{cm}^{-1}$, $g = 0.8$, $n_r = 1.4$ is simulated using Monte Carlo methods in the steady-state and time-domain. We compare the results to solutions of the diffusion equation in a semi-infinite medium [85] and to equations (4.12) and (4.15) when solved for a 2 and 8 layered medium with the same optical coefficients in each layer. Here, we used a cylinder radius of $a = 20$ cm and a total cylinder length L of 10 cm (i.e., the thickness of each layer in the 2 and 8 layered model was 5 and 1.25 cm, respectively) to approximate a semi-infinite medium. As previously shown [85], diffusion theory exhibits excellent agreement with relative errors ($|1 - \Phi_{DT}/\Phi_{MC}|$) < 0.05 compared to Monte Carlo simulations given enough scattering events. Equation (4.12) also shows excellent agreement to the closed-form semi-infinite solution [85] in both the steady-state and time-domain giving similar relative errors to the Monte Carlo results.

In contrast to the semi-infinite solution [85], the numerical accuracy of equation (4.12) is affected by the termination of an infinite sum after n terms. For example, given a large amount of terms ($n \approx 1,500$), the layered simulations shown in Fig. 4.5 can approximate the closed-form semi-infinite solution close to the limits of the numerical precision (detailed below). In practice, the sum should be terminated once a desired precision is reached. For example, to achieve similar relative tolerances to the Monte Carlo results in Fig. 4.5a, the steady-state fluence used $n = 500$ for $\rho < 2$ cm, $n = 1000$ for $\rho < 7$ cm, and $n = 1500$ for $\rho < 10$ cm whereas in Fig. 4.5b we use just $n = 50$ for both the 2 and 8 layer simulations in the time-domain for $\rho = 1.5$ cm. In general, to simulate lower fluence values a larger number of roots in equation (4.12) will be required to achieve similar relative errors. Consequently, the number of terms n required in equation (4.12) will be dependent to varying degrees on the input optical properties and cylinder dimensions considered.

In Fig. 4.6, we investigated the convergence properties of equation (4.12) as a function of the number of terms n used in the summation. We considered an example 2-layer medium with baseline optical properties of $\mu_{s1}' = \mu_{s2}' = 10\ \mathrm{cm}^{-1}$, $\mu_{a1} = \mu_{a2} = 0.1\ \mathrm{cm}^{-1}$, $\rho = 1.0$, $l = (0.1, 20)$ cm, $z = 0$ cm, and $a = 8$ cm. The fluence was calculated as a function of summation terms $n \in (50, 3500)$ for varying ranges of 6 input parameters (μ_{s1}', μ_{s2}', μ_{a1}, μ_{a2}, z, a) while keep-

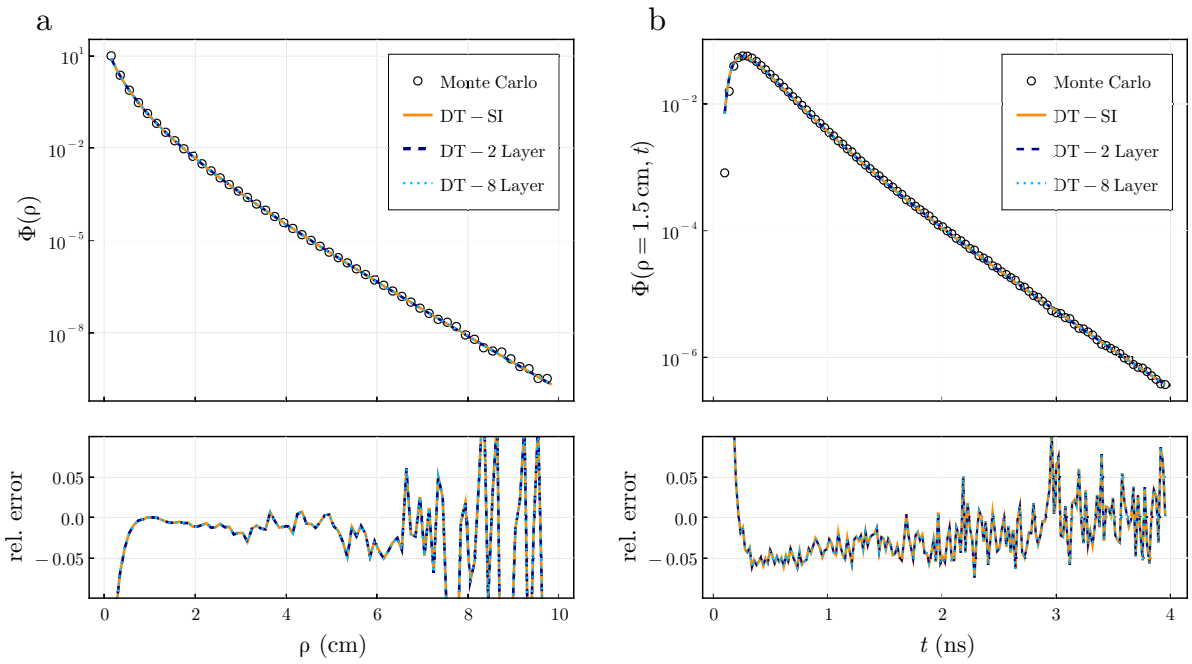

Figure 4.5: Equations (4.12) and (4.15) computed for both 2 and 8 layers agree with Monte Carlo simulations within relative errors of 0.05 which matches the errors achieved with the semi-infinite (SI) solution [85]. We show the (a) steady-state and (b) time-resolved fluence calculated with Monte Carlo simulations and diffusion theory for a semi-infinite medium with optical coefficients $\mu_a = 0.1$ cm^{-1}, $\mu_s' = 10$ cm^{-1}, $g = 0.8$, $n_r = 1.4$ and $z = 0$ cm. We considered the same optical properties in each layer and laterally infinite geometries in (4.12) and (4.15) to approximate semi-infinite media. The relative error between the diffusion theory results and Monte Carlo are shown below.

ing all other variables constant. The absolute difference between this calculation which was done in double precision and a calculation done in quadruple precision with $n = 50,000$ is shown in Fig. 4.6. The convergence of equation (4.12) is highly dependent on the scattering coefficient in the first layer μ_{s1}' as seen in Fig. 4.6a. Increasing μ_{s1}' severely diminishes the convergence of equation (4.12) when $z = 0$ (see Supplementary material in Appendix A for extended discussion). On the other hand, for the range of values shown here, μ_{a1}, μ_{a2}, and μ_{s2}' had a negligible effect on the convergence. There is a close relationship between μ_{s1}' and z as shown in Fig. 4.6a and 4.6e and their effect on the convergence of equation (4.12). When $z \approx z_0$ with $z_0 = 1/\mu_{s1}'$, equation (4.12) requires a high number of terms to converge. This is also the primary reason why increasing the scattering coefficient also requires significantly more terms when $z = 0$ as $z_0 \approx z$. Additionally, increasing a results in slower convergence due to smaller values of s_n during the sum. The routine can be made accurate down to absolute errors of the machine precision used in the calculation. For example, Fig. 4.6 was calculated using double precision arithmetic with machine precision

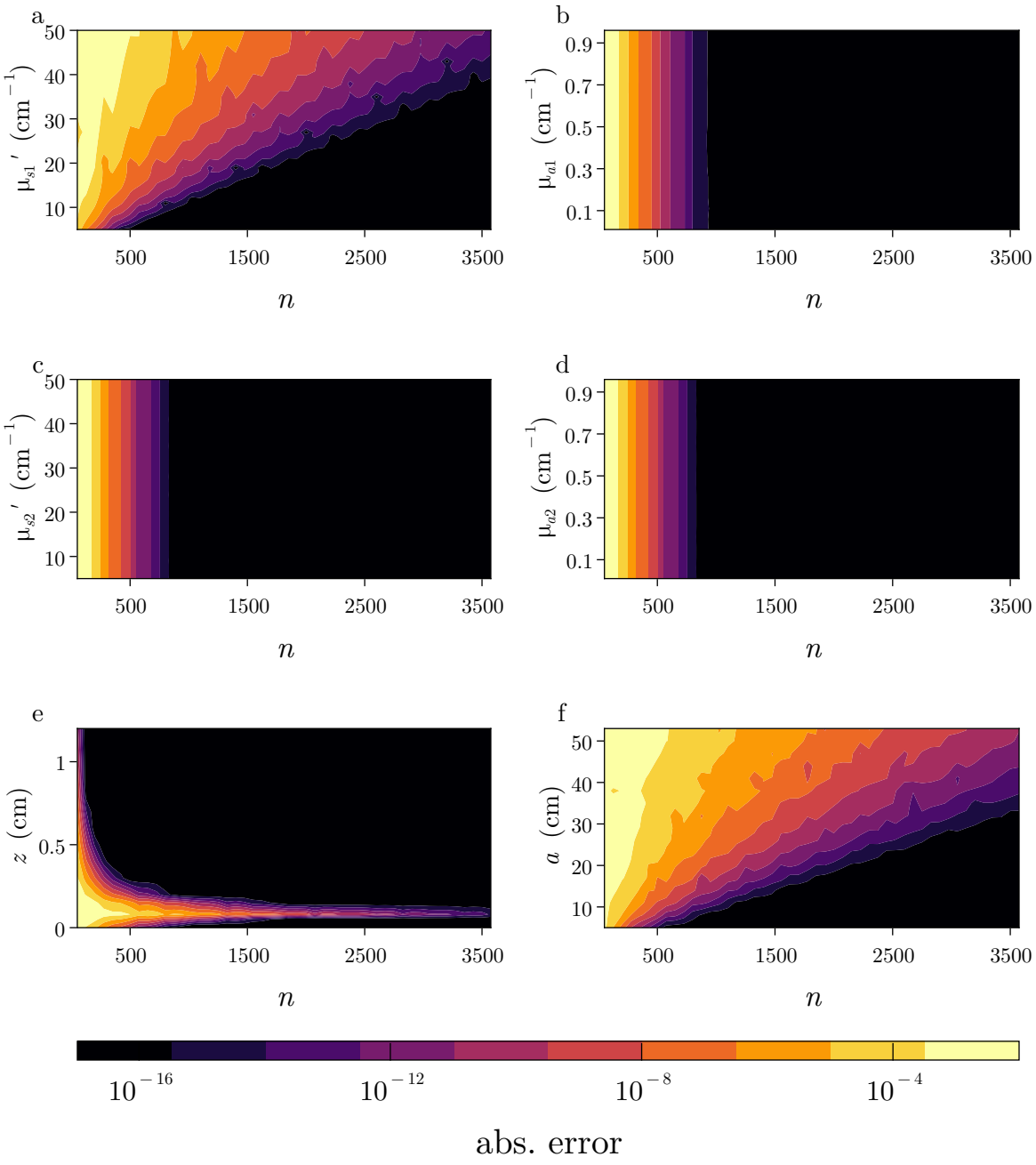

Figure 4.6: The rate of convergence of the infinite sum in equation (4.12) depends mostly on input parameters μ_{s1}', z (detector depth), and a (cylindrical radius) while showing little dependence on μ_{a1}, μ_{a2}, and μ_{s2}'. We show the absolute error between equation (4.12) when calculated in quadruple precision using $n = 50,000$ and when calculated in double precision as a function of the number of terms n used in (4.12) for different values of (a) μ_{s1}', (b) μ_{a1}, (c) μ_{s2}', (d) μ_{a2}, (e) z, and (f) a. We fix the other properties to $\mu_s' = 10$ cm^{-1}, $\mu_a = 0.1$ cm^{-1}, $l = (1.0,\ 20.0)$ cm, $a = 10$ cm, and $\rho = 1$ cm.

$\epsilon \approx 10^{-16}$. The loss of precision in calculating $J_0(s_n\rho)$ in equation (4.12) is the primary limitation of the routine. For typical μ'_{s1} found in biological tissue ($\mu'_{s1} < 50\,\mathrm{cm}^{-1}$), $n < 1,000$ is usually sufficient. For example, only 50 terms were used in Fig. 4.5b resulting in similar relative errors compared to Monte Carlo simulations when using 5,000 terms. However, the numerical procedure should check for convergence during the summation of equation (4.12) so that n can be dynamically determined during the routine.

The accuracy of the time-domain solution given in equation (4.15) is affected by both the termination of the sum in equation (4.12) as previously discussed and the numerical inversion of the Laplace integral in equation (4.15). We focus on two main attributes for the convergence of the inverse Laplace transform: (a) the hyperbola contour size (proportional to $\Lambda = t_2/t_1$) and (b) the number of Laplace space evaluations N used to evaluate the Laplace integral in equation (4.15) by comparing the time-resolved fluence simulated with equation (4.15) to the semi-infinite solution [85]. The fluence is simulated at $\rho = 1$ cm on the top boundary ($z = 0$) using a 4-layer model with layer thicknesses of $l_k = (0.5, 1.5, 3.0, 5.0)$ cm, $\mu'_s = 10\ \mathrm{cm}^{-1}$ and $\mu_a = 0.1\ \mathrm{cm}^{-1}$ with a radius of 15 cm to approximate a semi-infinite geometry. Typically, the time-domain signal is required at many values in some range $t \in (t_1, t_2)$ where it becomes significantly more efficient to use a single contour for all time points [106].

In Fig. 4.7a, we show the absolute (top) and relative (bottom) errors between equation (4.15) and the semi-infinite solution [85] at a single instant of time $t = 1.0$ ns as a function of N, for four different values of Λ. Variable values of Λ are achieved by using different t_1 values of 1.0, 0.1, 0.01, and 0.001 ns such that $\Lambda t_1 = 5$ ns is fixed and $t = 1$ ns is within the bounds of (t_1, t_2). The absolute errors were similar for any t value within $t \in (t_1, t_2)$ while the relative error was dependent on the value of t (i.e. larger relative errors are observed at long times when the fluence is lowest). Less than 20 Laplace evaluations were needed to give absolute errors $< 10^{-8}$ even for large values of Λ. We can also see that the sum exponentially converges allowing it to be accurately computed with the midpoint rule [165]. The main limitation is that the function must be evaluated at very small and large values along the contour which leads to floating point errors limiting the procedure to absolute errors approaching the machine precision. Additionally, the integration nodes along the contour depend on the total number of evaluations N which inhibits reuse of evaluations if a higher number of points are needed. Therefore, for the best computational performance N must be determined before the computation.

In Fig. 4.7b, we considered a single contour $\Lambda = 200$ to reconstruct 600 time points in $t \in (0.03, 6.0)$ and we show these for four different values of N. A larger N improved the overall accuracy and was relatively independent of the time point $t \in (0.03, 6.0)$ for a given N. For larger contours $\Lambda = t_2/t_1$ a higher number of N are needed to reconstruct the time-domain signal over the whole time window $t \in (t_1, t_2)$ for a given absolute error. For example, Fig. 4.7b shows the

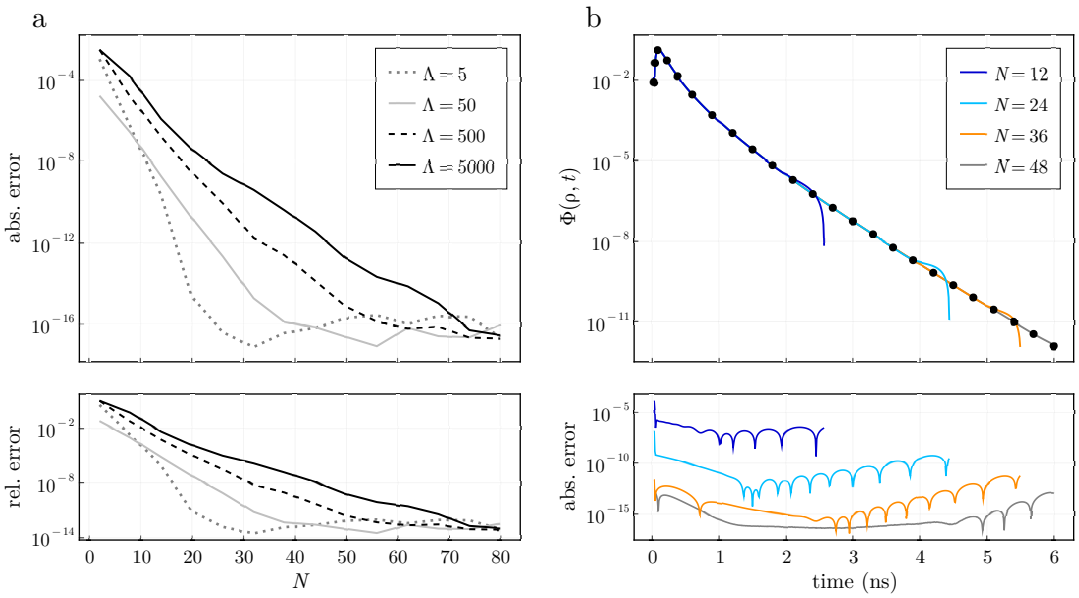

Figure 4.7: (a) The (top) absolute and (bottom) relative errors for the time-domain reconstruction at a single time value $t = 1$ ns in $(t_1, \Lambda t_1)$ between the time-domain solution in equation (4.15) and the semi-infinite solution as a function of the number of Laplace space evaluations N. Larger contour sizes ($\propto \Lambda$) require higher values of N to reach similar accuracies. (b) Reconstruction of the time-domain signal at 600 time points in $t \in (0.03, 6.0)$ corresponding to $\Lambda = 200$ considering four different values of N. The semi-infinite solution is shown as black circles with the resulting absolute error between the semi-infinite and layered solution shown in the bottom plot. The absolute error is dependent on N, which is similar for all time values considered in $t \in (t_1, t_2)$

same Λ but reconstructs the time-domain signal for different values of N. However, smaller values of N are not able to reconstruct accurately over the entire time window due to the lower fluence values $\Phi(\rho, t)$ at later times. A given N reconstructs the time-domain signal over the entire window at a relatively fixed absolute error. Therefore, larger relative errors will be observed at later times when the fluence is lowest.

We note that calculations in Fig. 4.7b are only shown up to the point where the time-domain signal is not accurately reconstructed. Therefore, it is recommended to use a t_1 as late as possible and choose N based on the dynamic range of time-domain signal required. For example, 12 Laplace evaluations were typically required to reconstruct the time-domain signal with a dynamic range of 3 orders of magnitude where 24 evaluations can provide roughly 6 orders of magnitude which represent typical dynamic ranges of time-domain systems [72, 62]. Increasing the number of evaluations does not decrease absolute errors once the errors reach the machine precision. Coincidentally, we have found that the numerical inversion of the Laplace transform is also limited by absolute errors approaching the machine precision, similar to the numerical computation in the

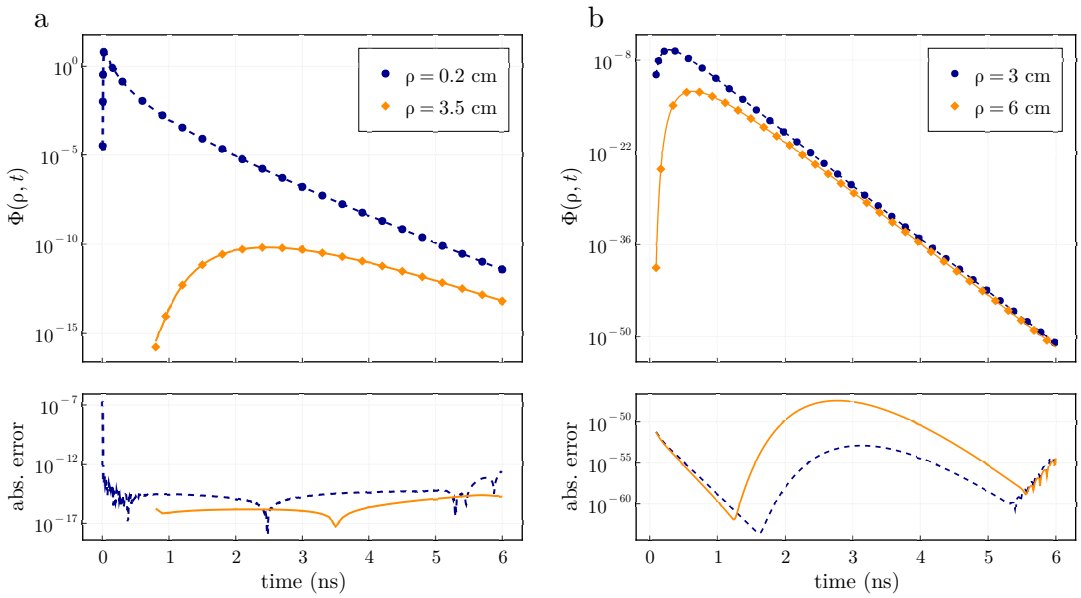

Figure 4.8: Equation 4.15 can be computed to absolute errors up to the machine precision compared to homogeneous closed form models at high scattering over a wide range of times and distances away from the source. (a) Time-resolved fluence from a 4-layered highly scattering media with optical properties μ_s' = 80.0 cm^{-1} and μ_a = 0.1 cm^{-1} at ρ = 0.2 and ρ = 3.5 cm. Computation was performed using double precision arithmetic. (b) Time-resolved fluence at the top boundary of a 4- layered media with optical properties μ_s' = 10.0 cm^{-1} and μ_a = 0.6 cm^{-1} at ρ = 3 and ρ = 6 cm. Computation was performed using octuple precision arithmetic. The semi-infinite solution is shown as markers with the absolute error between the two solutions shown below.

spatial domain.

The previous examples have focused on modest values of μ_s', μ_a, ρ, and layer thicknesses. In Fig. 4.8, we reconstruct the time-domain signal for high scattering media and large layer thicknesses over a wide range of times which has previously been previously difficult due to numerical overflow [184, 59, 84]. In Fig. 4.8a, the time-domain signal on the top boundary ($z = 0$) for a high scattering medium $\mu_s' = 80\ \mathrm{cm}^{-1}$ and $\mu_a = 0.1\ \mathrm{cm}^{-1}$ at ρ = 0.2 and ρ = 3.5 cm is shown. We considered a 4-layered medium with the same optical properties in each layer with layer thicknesses $l_k = (0.5, 1.5, 3.5, 30.0)$ cm and a cylinder radius of 15 cm for comparison to a semi-infinite model [85]. We used $n = 1,000$ roots in equation (4.12) with $N = 24$ Laplace evaluations at ρ = 3.5 cm and $N = 72$ evaluations at ρ = 0.2 cm. Although the fluence at ρ = 0.2 cm is significantly larger, we considered $t \in [0.004, 6.0]$ resulting in a $\Lambda = 1500$ whereas at ρ = 3.5 we considered $t \in [0.8, 6.0]$ giving $\Lambda = 7.5$. This again highlights that the number of Laplace space evaluations is highly dependent on Λ. Even considering a very large layer thickness $l_4 = 30$ cm and large reduced scattering coefficient $\mu_s' = 80\ \mathrm{cm}^{-1}$, the time-resolved fluence can be easily simulated in

double precision arithmetic, very close to the source, and at both early and late times.

In Fig. 4.8b we show calculation of the time-domain fluence at the surface ($z = 0$) for very low fluence values from a high absorption medium ($\mu_s' = 10.0\ \mathrm{cm}^{-1}$ and $\mu_a = 0.6\ \mathrm{cm}^{-1}$) at two detector locations of ρ = 3.0 cm and 6.0 cm and for $t \in [0.1, 6.0]$. These calculations were performed in octuple precision using $N = 168$ Laplace evaluations and only $n = 600$ roots in equation (4.12) which reconstructed the time-domain signal over 50 orders of magnitude in dynamic range with high numerical accuracy. The absolute error is relatively constant for $t \in (t_1, t_2)$ which leads to a higher relative error at lower fluence values. An increase in amount of Laplace evaluations is needed for very low fluence values and can also be observed by extrapolating the asymptote of convergence in Fig. 4.7 to very low absolute errors. Lastly, the roots of J_0 must be calculated in higher precision to achieve the shown absolute errors.

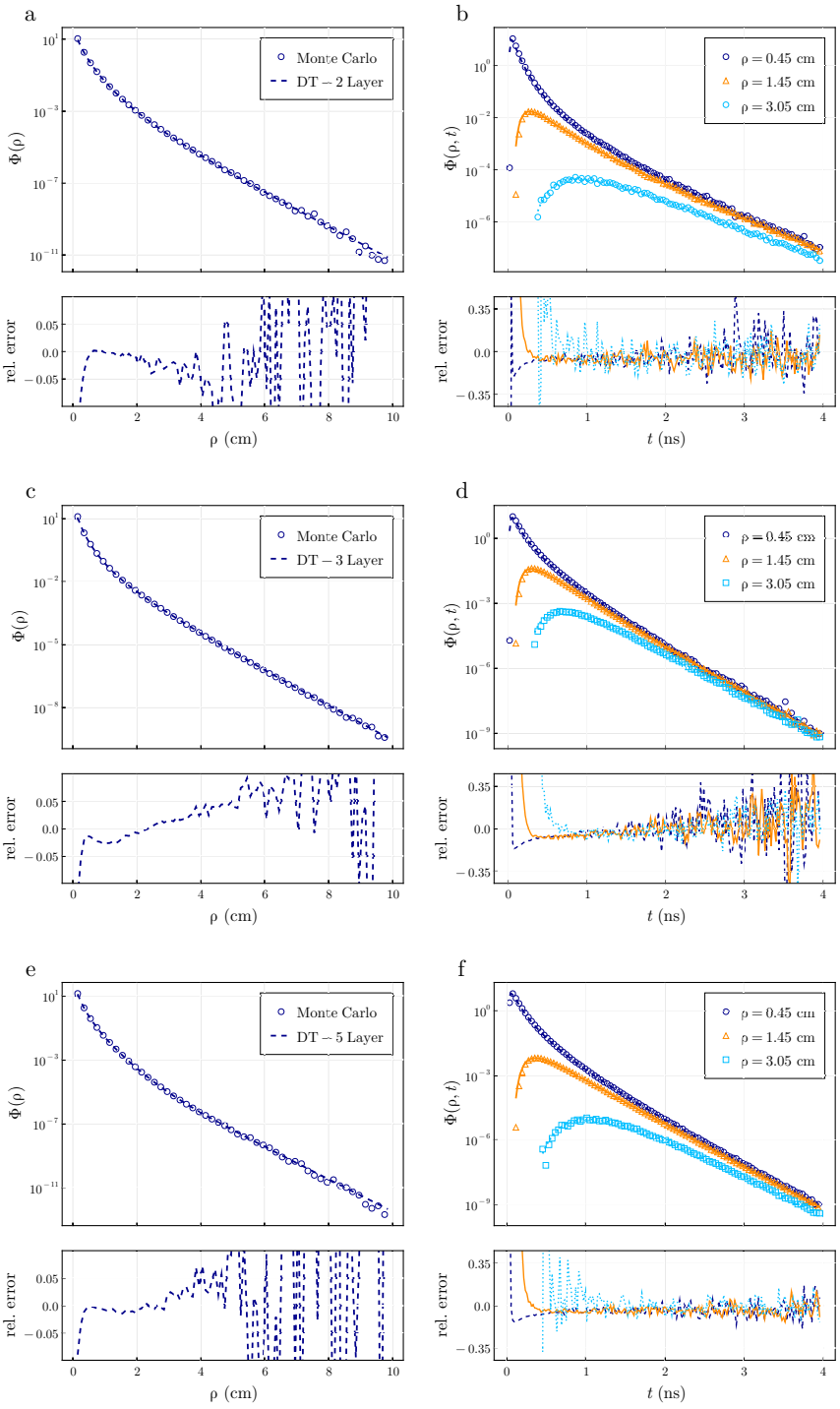

Figure 4.9: Comparison of the (left column) steady-state and (right column) time-domain fluence using diffusion theory (lines) simulated using equations (4.12) and (4.15) and the Monte Carlo method (symbols) for the tissue geometries representing a (top row) 2-layer, (middle row) 3-layer muscle, and (bottom row) 5-layer brain tissue models. The relative error between the Monte Carlo results and diffusion model are shown in the plots below. The diffusion approximation displayed relative errors less than 0.1 over a large domain of arguments suggesting it could be used in a variety of diverse tissue geometries.

Comparison to Monte Carlo Simulations

Next, we compared the solutions obtained from equations (4.12) and (4.15) to Monte Carlo simulations for both the steady-state and time-domain. We consider three different tissue geometries that are of high clinical interest and have been extensively used to model light propagation in different organ systems previously: a 2-layer model [86], a 3-layer model representing a skin/fat/muscle layer[83], and a 5-layer brain model [56] representing a scalp, skull, cerebrospinal fluid (CSF), and a gray and white matter layer.

The optical properties considered in the 2-layer model are $\mu_{a1} = 0.2\ \mathrm{cm}^{-1}$, $\mu_{a2} = 0.1\ \mathrm{cm}^{-1}$, $\mu'_{s1} = 13\ \mathrm{cm}^{-1}$, and $\mu'_{s2} = 12\ \mathrm{cm}^{-1}$ with layer thicknesses of $l_1 = 6$ mm and $l_2 = 90$ mm. We report the optical properties of the 3-layer muscle and 5-layer brain model in Table 4.1. For all tissue models, we consider the index of refraction for each layer to be $n_r = 1.4$ with the external index of refraction being air ($n_r = 1$). The anisotropy $g = 0.8$ was consistent for all layers in the Monte Carlo simulations. In all cases we compare the fluence on the top boundary ($z = 0$) as a function of ρ for the steady-state calculations and as a function of t in the time-domain for $\rho = 0.45, 1.45$, and 3.05 cm.

Table 4.1: Optical properties and layer thicknesses for the 3 layer skin/fat/muscle [83] and 5 layer brain tissue used in the Monte Carlo simulations [56]. The diffusion model utilized the same parameters except a $\mu'_s = 3.5\ \mathrm{cm}^{-1}$ was used in the CSF layer [37].

Skin, Fat, Muscle Model [83]				Brain Model [56]			
	$\mu_a\ \mathrm{cm}^{-1}$	$\mu'_s\ \mathrm{cm}^{-1}$	l (cm)		$\mu_a\ \mathrm{cm}^{-1}$	$\mu'_s\ \mathrm{cm}^{-1}$	l (cm)
skin	0.15	15	0.12	scalp	0.18	19	0.5
fat	0.02	12	0.38	skull	0.16	16	0.8
muscle	0.2	5	10.0	CSF	0.04	0.25	0.2
-	-	-	-	Gray	0.36	22	0.5
-	-	-	-	White	0.14	9.1	4

In Fig. 4.9, we compare the steady-state and time-domain fluence when simulated using the Monte Carlo method and diffusion theory. The left column shows the steady-state fluence $\Phi(\rho)$ for $\rho \in (0.15, 10)$ cm simulated using equation (4.12). Excellent agreement (relative errors < 0.1) is observed for all three tissue models, however the agreement is not uniform. The 2-layer model showed the best agreement for all values of ρ where the results asymptotically agreed with the Monte Carlo method. The 3-layer muscle model showed good agreement for $\rho < 5$ cm, but

did not asymptotically agree. These results are consistent with recent reports [107] that showed a breakdown in diffusion theory when the mean free path approaches the thickness of the top layer. Here, a top layer thickness of 1.2 mm was used. Although the significance of these errors were not studied on the reconstruction of optical properties, the relative errors between Monte Carlo solutions are less than 0.1 for $\rho < 6$ cm. Diffuse optical measurements are not usually collected at such large distances due to low signal to noise. A similar effect is observed in the brain model Fig. 4.9e where agreement (relative error < 0.1) is observed for $\rho < 6$ cm, however longer distances show higher errors. These errors can be mostly attributed to the limitations of diffusion theory to accurately model the low scattering CSF layer [37]. Our analytical solutions utilized $\mu_s' = 3.5\,\mathrm{cm}^{-1}$ to most accurately model the low scattering CSF layer with diffusion theory as previously suggested [37], though the choice of μ_s' significantly affects the resulting fluence calculated with diffusion theory for $\rho > 6$ cm. If μ_s' is less than 4 cm^{-1}, a severe overestimation of the fluence is seen. Practically, for $\rho > 6$ cm it may become unrealistic to consider the CSF and other brain layers as parallel planes. We note that all models had similar disagreements for $\rho < 0.5$ cm which is a known limitation of diffusion theory [85].

In the right column of Fig. 4.9, we show the time-domain fluence for $\rho = 0.45,\ 1.45,\ 3.05$ cm simulated using equation (4.15) and compare to Monte Carlo results. The 2-layer model is well approximated by diffusion theory in the time-domain for each value of ρ given enough scattering events illustrated by the uniform agreement across a wide range of time values. As in the spatial domain, the time domain results for the 3-layered model do not asymptotically converge to Monte Carlo simulations due to the small top layer thickness. The agreement is not uniform for each value of ρ as shorter distances are better approximated until much later arrival times. This is in contrast to the 5-layer model where the errors are relatively flat at all times and distances. This could be attributed to only presenting results in the time-domain for $\rho < 3.05$ cm, whereas the effect of the low scattering CSF layer is more significant for $\rho > 6$ cm. We note that the precise choice of μ_s' in the CSF layer for the distances and times shown do not significantly affect the time-domain simulations compared to the steady-state results. Additionally, decreasing the discretization of $t,\ \rho$ and z and simulating for more photons in the Monte Carlo method will reduce the noise, however, smaller discretization will not improve agreement between diffusion and Monte Carlo where they do not asymptotically agree.

Computational Time

In Table 4.2, we show the amount of time in microseconds to compute the steady-state fluence in the top layer, $\Phi_1(\rho, z = 0)$, for a given number of terms n considered in the sum in equation (4.12) for 2, 4, 8 and 16 layers. Different values of optical properties do not significantly affect the

computation time (when n is fixed), which is instead dependent on the number of roots n used in the sum. Though, increasing n does not linearly increase the computational time as shown in Table 4.2 because it is faster to compute $J_0(s_n\rho)$ at large arguments with asymptotic expansions. This affects the total run time because the calculation of $J_0(s_n\rho)$ accounts for nearly 40 $\%$ of the run time where the computation of $G_1(s_n, z)$ takes most of the remaining time. For realistic applications where less than 1,000 roots are needed, the fluence can be calculated in less than $\approx$ 100 μs for up to 8 layers.

Table 4.2: MacOS M1 CPU: Number of microseconds to compute steady-state fluence where n is number of roots in equation (4.12).

Layers	n = 100	n = 500	n = 1,000	n = 5,000
2	6	25	47	215
4	8	32	55	225
8	11	40	70	280
16	16	65	110	470

Table 4.3: Intel CPU: Number of microseconds to compute steady-state fluence where n is number of roots in equation (4.12).

Layers	n = 100	n = 500	n = 1,000	n = 5,000
2	6	30	55	240
4	8	35	65	275
8	12	50	85	370
16	19	80	140	620

Table 4.4: Mac M1: Number of microseconds to compute the time-domain fluence where N is the number of Laplace space evaluations.

Layers	N = 8	N = 16	N = 32	N = 64
2	250	470	920	1,840
4	320	600	1,100	2,300

The time-domain routine must compute the steady-state routine for N ($\approx 12 - 24$) complex absorption values. This procedure lends itself well to parallelism as each computation is independent

Table 4.5: Intel CPU: Number of microseconds to compute the time-domain fluence where N is the number of Laplace space evaluations.

Layers	N = 12	N = 24	N = 36	N = 72
2	270	540	800	1,600
4	340	695	1,030	2,090

and can be used at each time point needed. Therefore, performance is limited by the runtime listed in Table 4.2, however using a complex absorption term increases the runtime by 2.5x. In Table 4.2, we show the runtime in microseconds for the time-domain fluence as a function of the Laplace space evaluations N for 2 and 4 layered media considering $n = 600$ roots in equation (4.12) and 1024 time points. We note that the time values do not have to be linearly spaced as when using the Fast Fourier Transform.

If a dynamic range of 3 orders of magnitude is needed ($N \approx 12$), the fluence can be simulated in less than 300 μs. The performance in the time-domain is highly dependent on the CPU used and its multi-core performance. When using an Intel CPU 8700k with 6 cores and 12 threads the runtimes can be decreased by 30% compared to using a MacBook Pro M1 as shown in Tables 4.4 and 4.5. The number of Laplace evaluations used should be in multiples of the available number of threads. We note that the load times for multi-threaded applications represent a significant portion of the total runtime. For a low number of Laplace evaluations (¡16) these computational times can be reached within 2x using a single core. The advantage of these procedures is that rapid simulation can be performed on a personal laptop while allowing for time-domain runtimes to be significantly reduced with higher end CPUs.

4.5 Conclusion

Limitations of homogeneous tissue-models to describe light transport in layered biological media have been discussed previously [51, 55]. Although analytical models that incorporate heterogeneous optical properties are becoming more frequent, [65, 59, 13] their use, particularly in inverse calculations, is limited by their floating point accuracy accuracy and efficiency [184]. Therefore, homogeneous models are typically used given their simplicity and efficiency in solving inverse problems that require 100-1,000 evaluations of the forward model to reach convergence. Neural networks can also be used to quickly ($\approx$ 50 milliseconds) estimate tissue optical properties in inverse problems [78]. However, they require long training times and are roughly 1,000x slower than the presented analytical model for forward calculations [78, 61]. Several solutions for photon diffusion in layered media have been reported, but present technical difficulties for numerical com-

putation. We have investigated a previously developed model [101, 102] that has received wide interest [65, 59, 13, 58]. However, the model relies on numerical inverse transforms for obtaining the photon fluence for both steady-state and time-domain simulations which limits the numerical accuracy and speed. For example, the computation of the steady-state fluence requires the inversion of a Bessel-type 1-D inverse transform (equation 4.12) over the k^{th} root of the zeroth order Bessel function J_0. The discrete version has several advantages compared to using Gaussian integration [86, 104] as the roots can be precomputed to improve the overall speed of the routine and can be implemented with strict convergence criteria for accurate computation over a wide range of input arguments using a variable number of roots. This is important because the convergence of equation (4.12) is highly dependent on the model inputs (Fig. 4.6), where different optical properties and tissue geometries require a different number of roots to be used. However, these expressions require numerical integration over hyperbolic functions that can numerically overflow for large input arguments or at large roots of J_0.

In this work, we provide numerically stable expressions for the Green's functions in terms of exponentially decaying functions, which facilitates accurate computation for large input arguments (e.g., scattering, layer thickness, spatial frequency) over any root of J_0 without approximations or loss of generality that are usually required to numerically compute equation (4.12) [59, 84]. As shown in Fig. 4.6, the accuracy and speed of computed solutions is determined by the number n of roots used in the sum in equation (4.12) which is most dependent on μ_{s1}', a, and z. In practice, the values used for the cylindrical radius of the tissue-model a (Fig. 4.6f) should be kept as small as possible to increase convergence but should be large enough to accurately represent lateral boundary conditions. Although the total number of n largely dictates the speed and accuracy of the routine, the algorithm is limited to simulating equation (4.12) with absolute errors up to the machine precision in the calculation. This is largely due to the finite precision used in the calculation of $J_0(s_n\rho)$ in equation (4.12) which is limited to absolute tolerances approaching the machine precision. For higher precision calculations, it is important to calculate the roots of J_0 in the desired precision to simulate fluence values down to the machine precision. For experimental measurements with background noise, fluence values below the epsilon value of double precision ($\epsilon \approx 10^{-16}$) are rarely needed. Additionally, computing J_0 accounts for the majority of the routine's runtime especially when the fluence is required at multiple spatial locations, as is the case in many tomography [47] or functional imaging [163] applications. New numerical routines for the computation of J_0 were developed that decrease computational time by at least 3x [66] compared to using standard routines [3]. An advantage of the routine presented is that computing the fluence at 10 arbitrarily specified spatial locations takes only 3x longer than the times reported in Table 4.2. Although it can be difficult to directly compare computational times of different routines, as they depend highly on the computational resources and effort put into them, we were able to simulate

the steady-state fluence 500-1,000x faster than previously reported [104, 58]. We note that these times are achieved on a personal laptop using a single core.

Computation of the time-domain signal requires an additional inverse time transform which is usually performed with the Fourier Transform [59]. Here, we have used the inverse Laplace transform [106, 177] for faster and more accurate reconstructions of the time-domain signal. We have found that 12-24 terms in the Laplace integral are needed in equation (4.15) to reconstruct the time-domain signal with dynamic ranges of 3-6 orders of magnitude, which is the range of current experimental systems [72, 62]. Due to the decreased number of evaluations needed in the inverse time transform, the computational times for time-domain simulations are 1,000-10,000x faster than what is usually reported depending on the number of layers considered and accuracy required [176, 111, 102]. Most of the performance gain can be attributed to utilizing the faster converging Laplace transform instead of the Fourier transform [106] while other improvements come from other numerical optimizations for the steady-state calculation and threaded parallelism as further discussed in Appendix A in the Supplementary material. The Laplace transform can also evaluate the time-domain fluence up to absolute errors approaching the machine precision as shown in Fig. 4.7. The number of terms needed in the Laplace transform for adequate convergence will depend highly on the contour size $\Lambda = t_2/t_1$ which is recommended to be kept as small as possible for faster reconstructions.

A primary limitation of the layered solutions presented here is that a large amount (500-5,000x) of terms are required in the computation of equation (4.12) when $z = 0$ which is required for reflectance calculations. As seen in Fig. 4.6, increasing the top layer scattering coefficient will significantly increase the number of terms required in equation (4.12), while the convergence is mostly independent of deeper layer optical properties. This can be explained by the slow convergence of the particular solution of the Green's function when $z \approx 1/\mu'_{s1}$. When z is farther away from the source depth z_0 as seen in Fig. 4.6e, only a few terms are needed. However, if we approximate that $z \approx z_0$, it becomes possible to sum the particular solution of the Green's function exactly which improves convergence significantly. We present detailed derivations of this approximation in Appendix A in the Supplementary material and show that such an approximation when $\mu'_{s1} > 2$ cm^{-1} and $z = 0$ can simulate the fluence with relative errors down to 10^{-14} (Supplementary Fig. S3), which is as accurate as the exact forms in double precision arithmetic due to floating point errors. Therefore, it is highly recommended to use such an approximation in double precision arithmetic which can decrease computational times by 2-3 orders of magnitude depending on the input μ'_{s1}, allowing for computation of the steady-state fluence in less than a microsecond ((Supplementary Fig. S4). This approximate form also allows for very accurate simulation for large scattering coefficients where it is difficult for the exact expressions to converge due to the slow exponential decay of the sum.

Finally, in addition to testing the numerical accuracy and efficiency, we have tested the physical approximation of diffusion theory compared to the Monte Carlo method by using three previously reported layered tissue models that approximate several different organ systems [86, 83, 56]. We note that solutions to the RTE in layered media have been presented which are more accurate than the diffusion approximation but, like Monte Carlo methods, come at increased computational cost [107]. Additionally, the situations presented in Fig. 4.9 represent the simplest forms of heterogeneous media consisting of layered slabs which may be a rather crude approximation of complex biological media. Though, the use of such a simple approximation has been shown to provide similar accuracy to more realistic tissue geometries in a brain model using atlas based meshes [153]. The primary disadvantages of diffusion theory are the inability to correctly predict photon fluence for short time scales and source-detector separations and the requirement that $\mu_s' >> \mu_a$ [4, 52]. A recent report also indicated that the diffusion approximation could increase inaccuracies far away from the source in layered models where layer thicknesses are small compared to the mean scattering length [107]. We found that for a top layer thickness of 1.2 mm, these predictions were in agreement with the results reported in Fig. 4.9, but we also find that such errors were only significant at distances of $\rho > 5$ cm for steady-state calculations. These errors were not apparent in the time-domain for $\rho = 0.45, 1.45, 3.05$ cm when $t < 4$ ns (Fig. 4.9). We also find that our solutions from diffusion theory agree well with Monte Carlo simulations for a 5-layer model of the brain even when considering a thin CSF layer of low scattering (Fig. 4.9).

In conclusion, we have developed and verified an open-source, easy-to-use numerical algorithm to accurately and efficiently compute solutions of the diffusion equation in layered media. The absolute errors of the routine can be made arbitrarily accurate and can simulate both the steady-state and time-domain fluence 3 to 4 orders of magnitude faster than previously reported. Therefore, the routine could be used in inverse procedures to recover optical properties of measured data in real-time (1-10 Hz). It can also be employed for rapid generation of the intensity profile in layered media at multiple spatial locations and varying optical properties, as required in tomography and functional imaging applications. These solutions are also easily amendable to solve the correlation diffusion equation in layered media. An additional advantage of the routine is that the computational time marginally increases with the addition of a new layer, as a 4-layered medium can be computed within 10% of the time to compute 2-layers. This could allow for more accurate simulations in highly layered media such as the brain at little cost to total run times. Additionally, we showed good agreement between diffusion theory and Monte Carlo simulations in three separate tissue geometries of clinical interest.

CHAPTER 5

Numerical Approach to Quantify Depth-Dependent Blood Flow Changes in Real-Time Using the Diffusion Equation with Continuous-Wave and Time-Domain Diffuse Correlation Spectroscopy

This chapter was published in [74]. It discusses solutions to the correlation diffusion equation in layered media in both the continuous wave and time-domain using the methods described in Chapter 4. Focus is also given to the inverse problem and comparing diffusion theory with Monte Carlo. This chapter was prepared in collaboration with Suraj Rajasekhar, Samantha Zerafa, Dr. Karthik Vishwanath, and Dr. Mary-Ann Mycek.

5.1 Abstract

Diffuse correlation spectroscopy (DCS) is a non-invasive optical technique that can measure brain perfusion by quantifying temporal intensity fluctuations of multiply scattered light. A primary limitation for accurate quantitation of cerebral blood flow (CBF) is the fact that experimental measurements contain information about both extracerebral scalp blood flow (SBF) as well as CBF. Separating CBF from SBF is typically achieved using multiple source-detector channels when using continuous-wave (CW) light sources, or more recently with use of time-domain (TD) techniques. Analysis methods that account for these partial volume effects are often employed to increase CBF contrast. However, a robust, real-time analysis procedure that can separate and quantify SBF and CBF with both traditional CW and TD-DCS measurements is still needed. Here, we validate a data analysis procedure based on the diffusion equation in layered media capable of quantifying both extra- and cerebral blood flow in the CW and TD. We find that the model can quantify SBF and CBF coefficients with less than 5% error compared to Monte Carlo simulations using a 3-layered brain model in both the CW and TD. The model can accurately fit data at a rate of ¡10 ms for CW

data and < 250 ms for TD data when using a least-squares optimizer.

5.2 Introduction

Adequate cerebral blood flow (CBF) is required for delivery of oxygen and other nutrients to brain tissue, allowing CBF to serve as a biomarker for brain function and health [44]. The quantitation of CBF is therefore important for managing and diagnosing brain injury or other diseases associated with ischemia or inadequate vascular autoregulation [20]. Diffuse correlation spectroscopy (DCS) is an optical technology that noninvasively measures blood flow by quantifying temporal speckle fluctuations of a coherent light field illuminating the tissue surface, usually in the near-infrared spectrum [43, 92, 181]. Detected photons in such applications must propagate through the extracerebral scalp and skull layers to reach brain tissue [152, 184]. The backscattered light intensity temporally fluctuates and is quantified via its temporal autocorrelation function [14, 20]. Analytical solutions of the correlation equation are then obtained using diffusion theory and are used to fit measured autocorrelation functions to extract a quantitative blood flow index (BFi, cm^2/s), which has been shown to be a good surrogate for CBF measured *in vivo* [20, 189, 43, 15, 21].

Traditionally, DCS systems have used continuous-wave (CW) light sources which require long source-detectors separations to increase sensitivity to CBF [147, 151] as the CW-DCS signal is significantly impacted by shallower extracerebral scalp blood flow (SBF) changes [20, 152]. More recently, using picosecond pulsed lasers as sources has allowed DCS to operate in the time-domain (TD), which can increase sensitivity to deeper tissues by gating the photons time of flight to measure the autocorrelation at different time windows [160, 134, 29, 115]. Several studies have demonstrated the potential advantage of TD-DCS compared to CW-DCS for measuring deeper flow changes at shorter source-detector separations [161, 115, 29, 160]. However, although TD-DCS signals can select for longer pathlengths, these photons still traverse the superficial layers at least twice which must be accounted for in data analysis [148].

A major challenge in using DCS for neuromonitoring is that the detected light intensity interacts with all of the tissue layers in the propagation path (e.g., scalp, skull, cerebrospinal fluid (CSF), brain) [184, 189, 57, 147]. Homogeneous diffusion models are typically used for their simplicity and speed, but extracted BFi metrics have been shown to non-linearly depend on the flow properties of each layer [147]. Several analysis methods have been developed to account for these partial volume effects by using differential path-length factors [42, 45, 168], selecting longer photon pathlengths by weighting fits to shorter correlation times [152, 45], or by using pressure modulation procedures [7, 119]. Although useful for enhancing sensitivity to CBF, these methods do not eliminate top layer flow contributions as they still assume some level of tissue homogeneity [168]. Alternatively, using heterogeneous brain models simulated with Monte Carlo

(MC) methods [152, 184] or analytical solutions to the multi-layered correlation diffusion equation [45, 81, 95, 57, 189, 168] have shown promise for more robustly separating SBF from CBF [57, 184, 189].

The increase in available computational resources has led to the MC approach becoming more popular due to its higher accuracy at short source-detector separations and ability to accommodate complex tissue geometries [184, 148, 185]. Additionally, the MC method may be more robust than layered analytical models which can be numerically unstable [184]. However, for DCS to be employed to monitor patients in clinical settings, data analysis tools must be able to continuously and accurately quantify CBF changes for rapid treatment in the clinic [184]. A major limitation of MC is its high computational cost which mostly precludes its use in real-time data analysis [191, 50, 184].

Layered analytical models can provide a good compromise between reconstructive accuracy [153] and computational speed, yet they still remain significantly slower to compute than homogeneous models and are not typically used in inverse problems [184]. Forward models for TD-DCS in layered media have also been derived [96], but to the best of our knowledge have not yet been applied as inverse solvers, as TD solutions require orders of magnitude higher computational effort than CW approaches [60]. Currently, most applications employ homogeneous tissue models with diffusion theory for both CW- and TD-DCS [160], or use heuristic exponential based fitting for quantifying the BFi [148].

In this report, we develop and apply diffusion theory based analytical solutions of DCS signals in layered media to overcome existing challenges and validate its: (1) physical accuracy compared to MC simulations, (2) numerical stability and computational speed, and (3) use in inverse solutions to recover BFi from signals measured in layered head-tissue models. We present the theoretical framework for both CW- and TD-DCS based on the diffusion equation for an N-layered turbid medium [102, 75]. The model's performance is verified by comparisons to MC simulations across a range of source-detector separations for both the CW and TD. We examine using the forward model as an inverse solver and benchmark quantitative recovery of both SBF and CBF from a 3-layered brain model. We conclude by discussing the advantages of CW and TD systems from the results, establishing the sensitivities of CW- and TD-DCS in recovery of SBF and CBF, and investigating the impact of source-detector separations and delay times on these sensitivities.

5.3 Methods

5.3.1 Diffusion theory in layered media

The motion of scattering particles is associated with the unnormalized electric field temporal autocorrelation function G_1 which in highly scattering turbid media such as biological tissue can be approximated with the correlation diffusion equation [43]. Solutions to the correlation diffusion equation can be obtained by first solving the regular photon diffusion equation

$$D\nabla^2\Phi(\vec{r}) - \mu_a\Phi(\vec{r}) = -S(\vec{r}) \tag{5.1}$$

and then replacing the absorption coefficient with a dynamic absorption term $\mu_a^d \rightarrow \mu_a + 2\mu_s' D_B k_0^2 \tau$ [14]. Φ, D , $S(\vec{r})$ and μ_a denote the fluence rate, the photon diffusion coefficient, the source configuration, and the absorption coefficient, respectively, where $D = (3\mu_s')^{-1}$ and μ_s' the reduced scattering coefficient. D_B is the Brownian flow-diffusion coefficient, $k_0 = 2\pi n/\lambda$ is the wavenumber and λ is the wavelength of the light source [79]. It is assumed that the mean-square displacement of the scattering particles over time τ undergoes Brownian motion (i.e., $\langle \Delta r^2(\tau) \rangle = 6D_B\tau$).

Because solutions to the photon diffusion equation can be used to calculate G_1 by a simple replacement, existing methods to solve the diffusion equation for specific geometries and boundary conditions can be extended for calculating autocorrelation using diffusion theory [14, 160]. Here, we extend our computationally efficient method [75] to solve the diffusion equation using extrapolated boundary conditions for fast calculation of the autocorrelation function in an N-layer tissue model made up of axially layered cylinders, each with independent μ_a, μ_s', and thickness l [102]. Assuming an incident beam onto the center of the topmost cylindrical layer can be approximated by an isotropic point source located at a distance of $z_0 = 1/\mu_s'$ from the incident surface, Eq. 5.1 can be solved in real space [75] by

$$\Phi(\rho, z=0) \approx \Phi^{SI}(\rho) + \frac{1}{\pi a'^2} \sum_{n=1}^{\infty} \hat{G}(s_n, z) J_0(s_n\rho) J_1^{-2}(a' s_n) \tag{5.2}$$

where J_m is the Bessel function of first kind and order m and s_n is determined from the roots of J_m for $J_m(a's_n) = 0$ where $n = 1, 2, ...$ is the n^{th} root of J_m. z is the location of the detector within the medium in cylindrical coordinates and $\Phi^{SI}(\rho)$ is the steady-state fluence for a semi-infinite medium [85]. An extrapolated boundary is determined using $a' = a + z_b$ where a is the radius of the cylinder and $z_b = 2AD$ where A is proportional to the fraction of photons that are internally reflected at the boundary [30]. For clarity on nomenclature, G_1 represents the unnormalized temporal autocorrelation function whereas $\hat{G}$ represents the Green's function in the top layer due to an isotropic source located in the top layer.

For the solutions presented here, we utilize the approximate forms in Eq. 5.2 given previously [75] which are accurate when $z \approx z_0$. We have shown that given $\mu'_{s1} > 2\,\mathrm{cm}^{-1}$ and $a >> \rho$ at $z = 0$ these forms are accurate to at least 16 digits which is exact in double precision arithmetic [75]. The expression for the Green's function $\hat{G}$ in the top layer in Eq. 5.2 is

$$\begin{aligned}\hat{G}(s_n, z) = &\frac{e^{\alpha_1(z+z_0-2l_1)}(1-e^{-2\alpha_1(z_0+z_{b1})})(1-e^{-2\alpha_1(z+z_{b1})})}{2D_1\alpha_1} \\ &\times \frac{D_1\alpha_1 n_1^2\beta_3 - D_2\alpha_2 n_2^2\gamma_3}{D_1\alpha_1 n_1^2\beta_3(1+e^{-2\alpha_1(l_1+z_{b1})}) + D_2\alpha_2 n_2^2\gamma_3(1-e^{-2\alpha_1(l_1+z_{b1})})}\end{aligned} \tag{5.3}$$

where $\alpha_k = \sqrt{(\mu_{ak} + 2\mu'_{sk}D_{Bk}k_0^2)/D_k + s_n^2}$. The subscript k signifies the k^{th} layer of the cylinder with distinct absorption μ_{ak} and scattering μ'_{sk} in each layer. In general, the quantities β_3 and γ_3 are obtained by downward recurrence relations with start values

$$\begin{aligned}\beta_N = &D_{N-1}\alpha_{N-1}n_{n-1}^2(1+e^{-2\alpha_{N-1}l_{N-1}})(1-e^{-2\alpha_N(l_N+z_{b_2})}) \\ &+ D_N\alpha_N n_n^2(1-e^{-2\alpha_{N-1}l_{N-1}})(1+e^{-2\alpha_N(l_N+z_{b_2})}) \\ \gamma_N = &D_{N-1}\alpha_{N-1}n_{n-1}^2(1-e^{-2\alpha_{N-1}l_{N-1}})(1-e^{-2\alpha_N(l_N+z_{b_2})}) \\ &+ D_N\alpha_N n_n^2(1+e^{-2\alpha_{N-1}l_{N-1}})(1+e^{-2\alpha_N(l_N+z_{b_2})})\end{aligned} \tag{5.4}$$

with the downward recurrence given by

$$\begin{aligned}\beta_{k-1} &= D_{k-2}\alpha_{k-2}n_{k-2}^2(1+e^{-2\alpha_{k-2}l_{k-2}})\beta_k + D_{k-1}\alpha_{k-1}n_{k-1}^2(1-e^{-2\alpha_{k-2}l_{k-2}})\gamma_k \\ \gamma_{k-1} &= D_{k-2}\alpha_{k-2}n_{k-2}^2(1-e^{-2\alpha_{k-2}l_{k-2}})\beta_k + D_{k-1}\alpha_{k-1}n_{k-1}^2(1+e^{-2\alpha_{k-2}l_{k-2}})\gamma_k\end{aligned} \tag{5.5}$$

We note that we seek just the terms β_3 and γ_3 which must be determined recursively if the total number of layers N is larger than 3. In that case, Eq. (5.4) is used to generate starting values in the recurrence relation, then Eq. (5.5) is used recursively until β_3 and γ_3 are obtained. If $N = 2$, $\beta_3 = 1-e^{-2\alpha_2(l_2+z_{b2})}$ and $\gamma_3 = 1+e^{-2\alpha_2(l_2+z_{b2})}$. For $N = 3$, only Eq. (5.4) is needed to calculate β_3 and γ_3. Presenting the coefficients in terms of exponentially decaying functions prevents numerical overflow in the inverse transforms and increases numerical stability [75].

For solutions in the time-domain, an inverse Laplace transform is performed using the substitution $\mu_a \to \mu_a + \bar{s}/c$ with c being the speed of light in the medium. The time-dependent fluence $\Phi(\rho, t)$ can be expressed by

$$\Phi(\rho, t, z = 0) \approx \Phi^{SI}(\rho, t) + \frac{1}{\pi a'^2}\sum_{n=1}^{\infty}\frac{1}{2\pi i}\left[\int_B e^{\bar{s}t}\hat{G}(s_n, \bar{s})\,d\bar{s}\right] \times J_0(s_n\rho)J_1^{-2}(a's_n) \tag{5.6}$$

where $\Phi^{SI}(\rho, t)$ is the time-domain fluence in a semi-infinite medium [85]. B denotes the Bromwich path where $\bar{s}$ is a complex number along the contour. We use a hyperbola contour as

detailed previously [75, 106]. Such a contour forces rapid decay in the integrand leading to more accurate and faster computation of the inverse time transform [75].

At this point, we need to relate the unnormalized electric field temporal autocorrelation function G_1 to the fluence rates previously derived. In this study, as well as most experimental settings, we are interested in the reflected light intensity at the top boundary ($z = 0$). The diffuse reflectance is typically calculated as the current across the boundary or the flux [85]

$$R_f(\rho) = -D\nabla\Phi(\rho, z) \cdot (-\mathbf{z})|_{z=0} \tag{5.7}$$

Alternatively, the reflectance can be written as a combination of both the fluence and flux terms [85] and for a medium of refractive index 1.4, the combined reflectance can be written as

$$R(\rho) = 0.118\Phi(\rho) + 0.306R_f(\rho) \tag{5.8}$$

The unnormalized temporal autocorrelation of the electric field function G_1 is simply calculated from the reflectance by replacing $\mu_a \rightarrow \mu_a^d$

$$G_1(\rho, \tau, D_b) = R(\rho, \mu_a^d) \tag{5.9}$$

The normalized electric field temporal autocorrelation function g_1 is then calculated by

$$g_1(\rho, \tau, D_b) = G_1(\rho, \tau)/G_1(\rho, \tau = 0) \tag{5.10}$$

For solutions in the time-domain, the TD fluence given in Eq. 5.6 is used to calculate the reflectance in either Eq.5.7 or Eq. 5.8, which are then translated to G_1 using Eq. 5.9.

5.3.2 Baseline flow tissue models using Monte Carlo simulations

To assess the accuracy and robustness of the described diffusion theory model to extract depth-dependent flow parameters, we consider a physiologically relevant 3-layer brain model consisting of the scalp, skull, and brain layer, as reported previously [189]. In this work, we only consider variations in BFi coefficients for scalp blood flow (SBF) and cerebral blood flow (CBF). All other parameters including the optical properties and layer thicknesses were held constant as shown in Figure 5.1. The refractive index of each layer was also kept constant at 1.4 and the external medium's refractive index equal to 1.0 to simulate air. Blood flow in the skull layer was assumed to be negligible (BFi = 0).

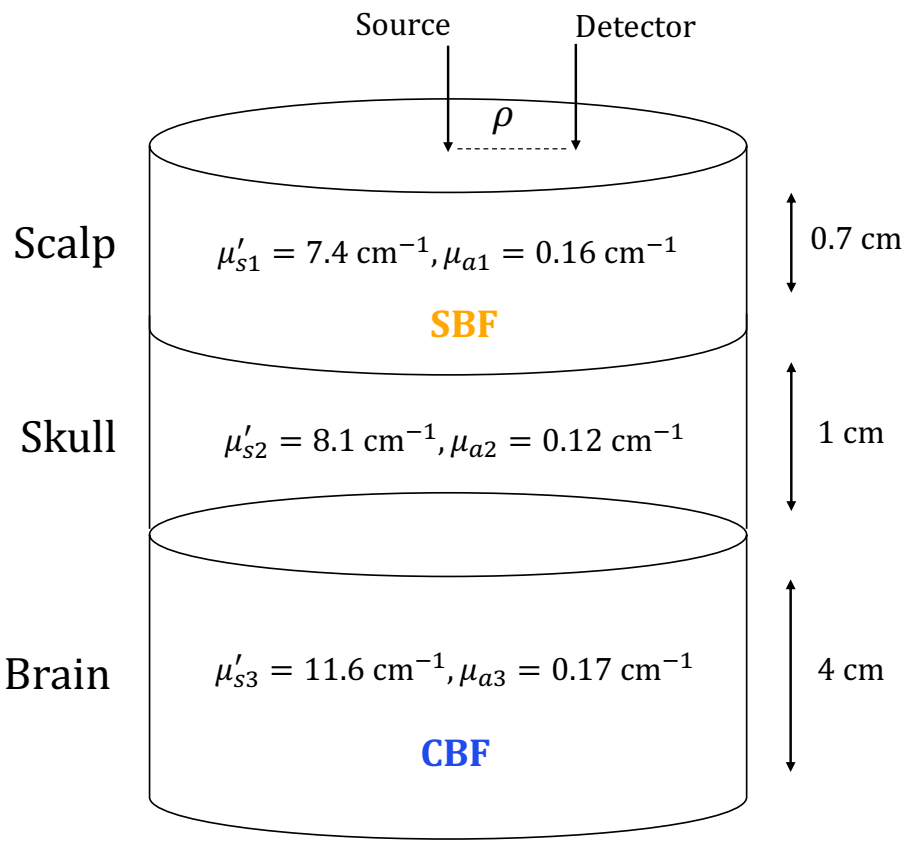

Figure 5.1: Schematic of the optical properties and layer thicknesses of the 3-layer brain model used in the Monte Carlo simulations. The scalp and cerebral blood flow coefficients are varied while keeping all labeled properties constant.

Using the optical properties and layer thicknesses shown in Fig. 5.1, the MC method was used to simulate a set of CW and TD normalized autocorrelation functions g_1. A previously developed MC code for photon propagation in laterally infinite layered media [172] was used to simulate the unnormalized autocorrelation function $G_1(\tau, \rho, t)$. The bin widths for Δt and $\Delta\rho$ were $\pm$ 5 ps and 0.5 mm, respectively. 500 million photons were used for each simulation. For CW-DCS, $G_1(\tau, \rho)$ was obtained by summing $G_1(\tau, t)$ across the total time-of-flight simulated (from 0 ns to 7.5 ns) [160]. Following previous reports [189], we used 10 evenly spaced values for CBF $\in [20, 90]\,\text{cm}^2/\text{Gs}$ and 10 values of SBF $\in [2.5, 30]\,\text{cm}^2/\text{Gs}$ such that SBF $\in [1/8, 1/3]\times$ CBF. For the case when SBF $= 30\,\text{cm}^2/\text{Gs}$, only 6 values of CBF from $20 - 58\,\text{cm}^2/\text{Gs}$ were used. This resulted in 96 total combinations of tissue flow models that were stored for source-detector separations $\rho \in [0.1, 3.05]$ in step sizes of 0.05 cm. The normalized autocorrelation functions $g_1(\tau)$ was obtained by dividing $G_1(\tau, t)$ by $G_1(0, t)$.

Simulated MC $g_1(\tau)$ were then fit to recover the SBF and CBF of the top-most and bottom-most layer using Eq. 5.10 with both reflectance models $R_f(\rho)$ given by Eq. 5.7 and $R(\rho)$ with Eq. 5.8. These fits were performed for varying ρ in the CW domain and for different t values in the TD. Each fit set the range of fitting for τ where $0.02 < g_1(\tau) < 0.98$ as the fit window. Estimates of SBF and CBF were retrieved using a non-linear fitting tool in the Julia programming language [12] based on the Levenberg-Marquardt algorithm [124]. Forward solutions were computed using the numerical model (Eq. 5.7 and Eq. 5.8). The optical properties and layer thicknesses of all the layers were considered known and were required as inputs to the inverse solver.

5.3.3 Noise model and sensitivity analysis

We briefly consider the sensitivity of $g_1(\tau)$ to a change in the analytical model's respective BFi (e.g., SBF and CBF). The effect of noise on the sensitivity metric is considered using a previously accepted noise model [190, 34]. We use a simplified version where the standard deviation of the noise in $g_1(\tau)$ is proportional to

$$\sigma(\tau) \approx \exp(\rho) \cdot \sqrt{\frac{(1 + \exp(-\gamma\tau))}{T_{int}}} \tag{5.11}$$

where T_{int} is a combination of the correlator bin time interval and integration time (i.e., measurement duration), ρ is the source-detector separation, and γ is the decay rate of $g_1(\tau)$ [34]. The noise was added to $g_1(\tau)$ after multiplying the standard deviation with a random number between [-1, 1]. In Fig. 5.2, we show examples of the added noise on $g_1(\tau)$ for two source-detector separations, $\rho = 1$ and 3 cm, with constant optical properties, $\mu_s' = 10\,\text{cm}^{-1}$ and $\mu_a = 0.1\,\text{cm}^{-1}$. We consider homogeneous flow values of 1 and 20 cm^2/Gs in $g_1(\tau)$ and $g_1^*(\tau)$, respectively, for better visualization. Two noise models, $\sigma_1(\tau)$ and $\sigma_2(\tau)$, were calculated using Eq. 5.11 with T_{int} values of 1 and 5. γ was calculated from the decay rate of $g_1(\tau)$.

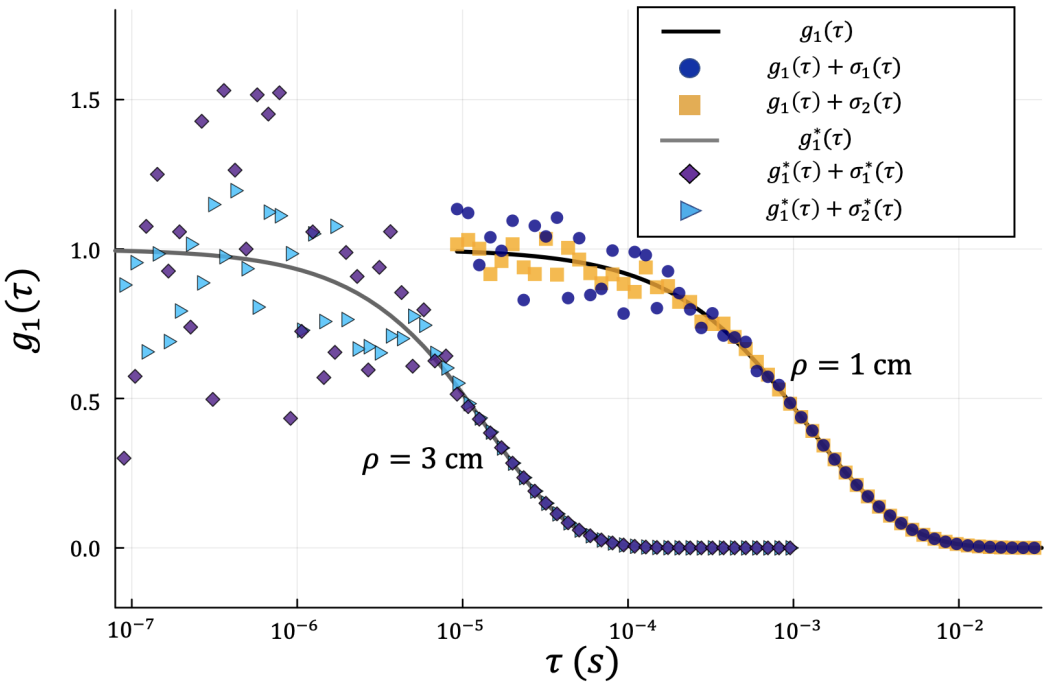

Figure 5.2: Example flow models at two source detector separations, $g_1(\tau, \rho = 1\text{ cm})$ and $g_1^*(\tau, \rho = 3\text{ cm})$, with two levels of added noise, $\sigma_1(\tau)$ and $\sigma_2(\tau)$, computed with Eq. 5.11 using $T_{\text{int}} = 1$ and 5, respectively.

The sensitivity of $g_1(\tau, BFi)$ to a flow change, ΔBFi, was estimated by calculating the relative change in $g_1(\tau)$, $(1 - g_1(\tau, BFi + \Delta BFi)/g_1(\tau, BFi))$, due to the perturbation. This allows for sensitivity estimates of CW- and TD-DCS to separate changes in SBF and CBF with noise. We note that the sensitivity can also be affected by τ, ρ, μ_a, and μ_s'. Here, we compare the sensitivity for $\rho \in (0.1, 3.5)$ cm with fixed optical properties, $\mu_s' = 10\,\text{cm}^{-1}$ and $\mu_a = 0.1\,\text{cm}^{-1}$. The dependence on τ was accounted for by averaging the relative change across a logarithm scaled array of τ values corresponding to $0.05 < g_1(\tau) < 0.95$.

5.4 Results

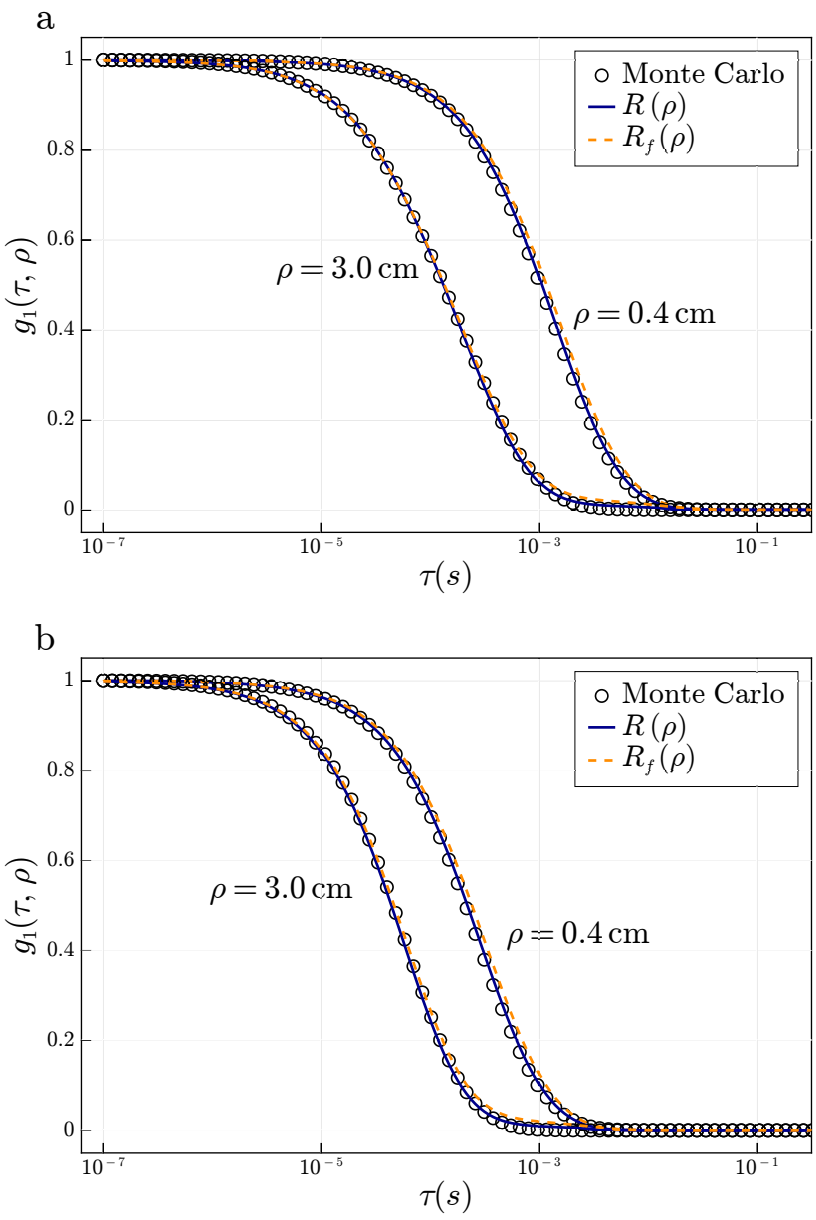

Figure 5.3: Comparison of the continuous-wave normalized autocorrelation function $g_1(\tau, \rho)$ simulated with the (symbols) Monte Carlo method and diffusion theory using the (blue solid line) $R(\rho)$ or (orange dash line) $R_f(\rho)$ reflectance models at two source-detector separations and at flow rates of (a) SBF = 6 $\mathrm{cm}^2/\mathrm{Gs}$; CBF = 20 $\mathrm{cm}^2/\mathrm{Gs}$ and (b) SBF = 27 $\mathrm{cm}^2/\mathrm{Gs}$; CBF = 20 $\mathrm{cm}^2/\mathrm{Gs}$. The model using $R(\rho)$ in Eq. 5.8 showed better agreement relative to $R_f(\rho)$ in Eq. 5.7 for the shorter source-detector separations and larger τ.

In Figure 5.3, we compare the CW normalized autocorrelation function $g_1(\rho, \tau)$ simulated with the MC method and those calculated with diffusion using Eq. 5.7 and Eq. 5.8. Comparisons are shown for two different flow models at two source-detector separations of 0.4 and 3 cm. For Fig. 5.3a, flow parameters of 6 and $20\ \mathrm{cm}^2/\mathrm{Gs}$ were used for the SBF and CBF, respectively whereas a SBF and CBF of 27 and $20\ \mathrm{cm}^2/\mathrm{Gs}$, respectively are shown in Fig. 5.3b. Optical properties and layer thicknesses are as shown in Fig. 5.1.

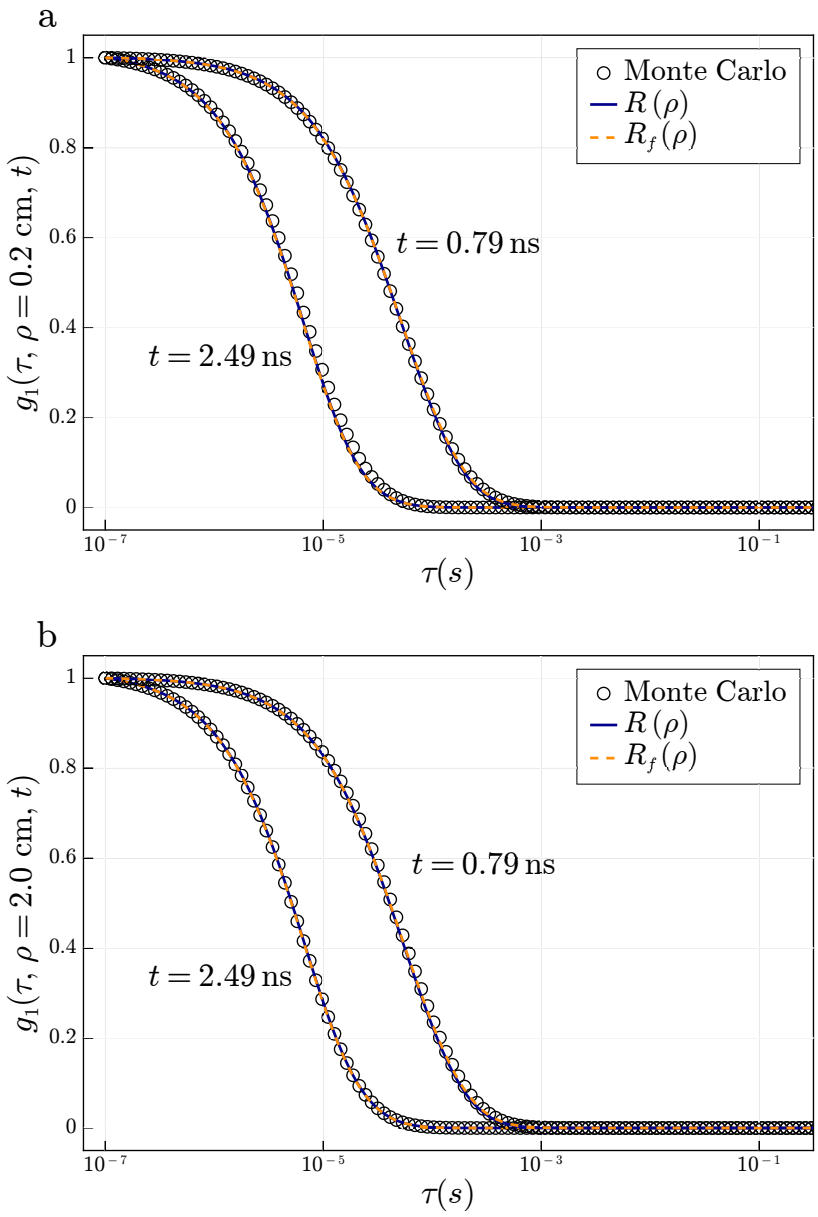

Figure 5.4: Comparison of the time-domain normalized autocorrelation function $g_1(\tau, \rho, t)$ simulated with the (symbols) Monte Carlo method and diffusion theory using the (blue solid line) $R(\rho)$ or (orange dash line) $R_f(\rho)$ reflectance models at two time values and at source-detector separations of (a) $\rho = 0.2$ cm and (b) $\rho = 2$ cm. A single flow model is considered where SBF = 18 $\mathrm{cm}^2/\mathrm{Gs}$ and CBF = 43 $\mathrm{cm}^2/\mathrm{Gs}$. Both reflectance models showed similar accuracy.

The largest difference between the two reflectance models can be observed at the shorter source-detector separations. Excellent agreement between MC and diffusion theory is observed when using Eq. 5.8, even at short distances of $\rho = 4$ mm. A larger difference is observed when using just the flux term described by Eq. 5.7 at short distances, however this expression becomes more

accurate farther away from the source. At the longer distance $\rho = 3$ cm, both expressions show good agreement to the MC method. However, there is a small deviation for small g_1 values (¡0.2) when using R_f whereas R is able to match the MC simulations over the full τ window.

In Figure 5.4, we compare the solutions for the TD-DCS $g_1(\rho, \tau, t)$ when simulated with the MC method and calculated from diffusion theory using both reflectance models R and R_f. Data in each figure are shown for a tissue model that has a SBF and CBF of 18 and $43\ \mathrm{cm}^2/\mathrm{Gs}$, respectively for two time values of 0.79 and 2.49 ns. The figures show these data at two source-detector separations, 0.2 and 2 cm (as noted in axis labels) in Fig. 5.4a and Fig. 5.4b, respectively. In contrast to the CW domain, the choice in using Eq. 5.7 or Eq. 5.8 showed little difference between each other to calculate $g_1(\rho, \tau, t)$. Either calculation had very good agreement to the MC method showing only small deviations from each other when $g_1(\rho, \tau, t) < 0.1$. Larger differences between Monte Carlo and diffusion theory were observed for shorter source-detector distance and longer time gates (Fig. 5.4a, $t = 2.49$ ns). However, it is also useful to note that MC simulations exhibit higher noise for longer times which could be causing these differences.

In Figure 5.5, the results of the inverse fitting procedure for the CW domain are shown. Here, the diffusion model is used as a forward model to fit for both SBF and CBF using the MC method as baseline simulations. In Fig. 5.5a and Fig. 5.5b, the recovered SBF and CBF are shown, respectively for all 96 of the flow tissue models recovered at two source-detector separations of 1 and 2.5 cm. For these figures we show just the fits using the R_f reflectance model as only small differences between the two reflectance models are observed at these two source-detector separations. There was a larger difference from true flow coefficients as determined by the MC simulations (black dashed lines) and recovered coefficients using the diffusion model when SBF was larger, however this did not appear to affect the accuracy of recovered CBF. A larger $\rho = 2.5$ cm was able to better recover CBF, though, both $\rho = 1$ and 2.5 cm showed sensitivity to SBF and CBF.

In Fig. 5.5c and Fig. 5.5d, the average percent error $100 \times ((\mathrm{BFi}_{MC} - \mathrm{BFi}_{DT})/\mathrm{BFi}_{MC})$ between the recovered SBF and CBF, is shown averaged across all 96 tissue models for four source-detector separations when using the two reflectance models. As shown in Fig. 5.3, at short distances ($\rho = 0.5$ cm), $R(\rho)$ produces significantly more accurate results. Interestingly, the reflectance model using just the flux $R_f(\rho)$ produced slightly more accurate results at the longer distances ($\rho > 1$ cm). The error in recovered SBF also slightly increases at longer distances as the sensitivity to the top layer decreases as we move farther away from the source. On the other hand, the recovered CBF significantly improves as we move to larger separations (Fig. 5.5d).

The percent error in recovery of relative SBF and CBF are shown in Fig. 5.5e and Fig. 5.5f, respectively for the two reflectance models at five source-detector separations. The relative error is calculated by normalizing the values of the true and recovered BFi of the first tissue model shown in Fig. 5.5a and Fig. 5.5b (SBF=2.5 $\mathrm{cm}^2/\mathrm{Gs}$; CBF = 20 $\mathrm{cm}^2/\mathrm{Gs}$), and averaging the percent error

across all the tissue models. The choice to normalize to the first tissue model is rather arbitrary, however the best absolute accuracy was observed for low SBF so this resulted in shifting absolute values the least. Good recovery of SBF is observed even at very short distances ($\rho = 2.5$ mm) while error increases after 1 cm due to the decrease in sensitivity to SBF. In this case, using $R(\rho)$ produced more accurate estimates of SBF. For CBF, large errors are observed at short distances ($\rho = 5$ mm) due to the very limited sensitivity to deeper layers at short separations. This error rapidly improves to less than 5% for $\rho > 1$ cm for both reflectance models.

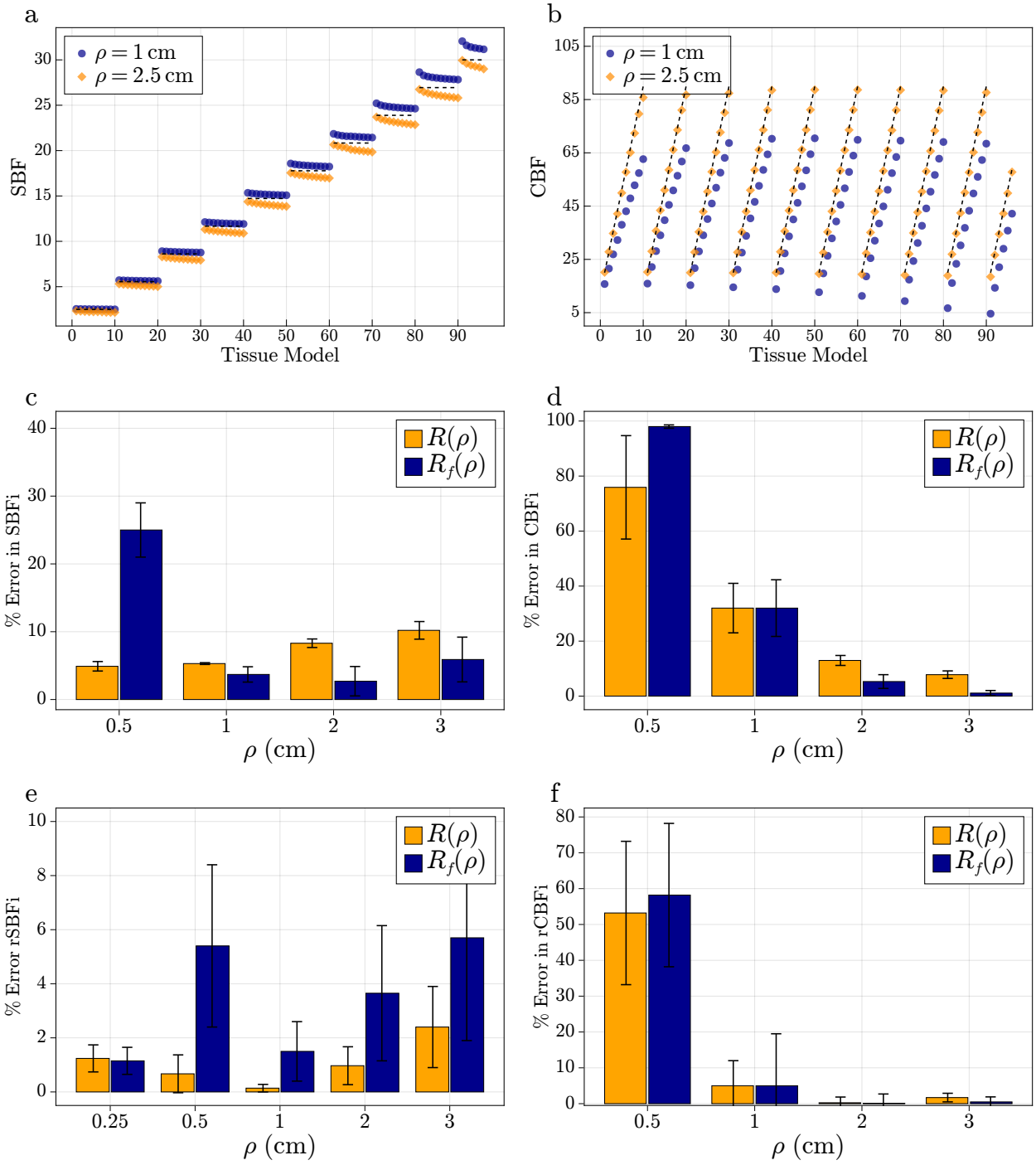

Figure 5.5: Results of inverse fits using CW-DCS diffusion theory fitted to MC simulated $g_1(\tau, \rho)$ curves. The recovered (a) SBF and (b) CBF coefficients are shown for two values of ρ where the black dashed lines represent the true flow values used in the MC simulations, for each tissue model, when recovered with the R_f reflectance model. The percent error between recovered absolute values of (c) SBF and (d) CBF is averaged over all the tissue models at four source-detector separations using both reflectance expressions (Eq. 5.7 and Eq. 5.8). The average error in relative flow changes of (e) SBF and (f) CBF are shown when recovered values of the first tissue model (as shown in (a) and (b)) are normalized to one.

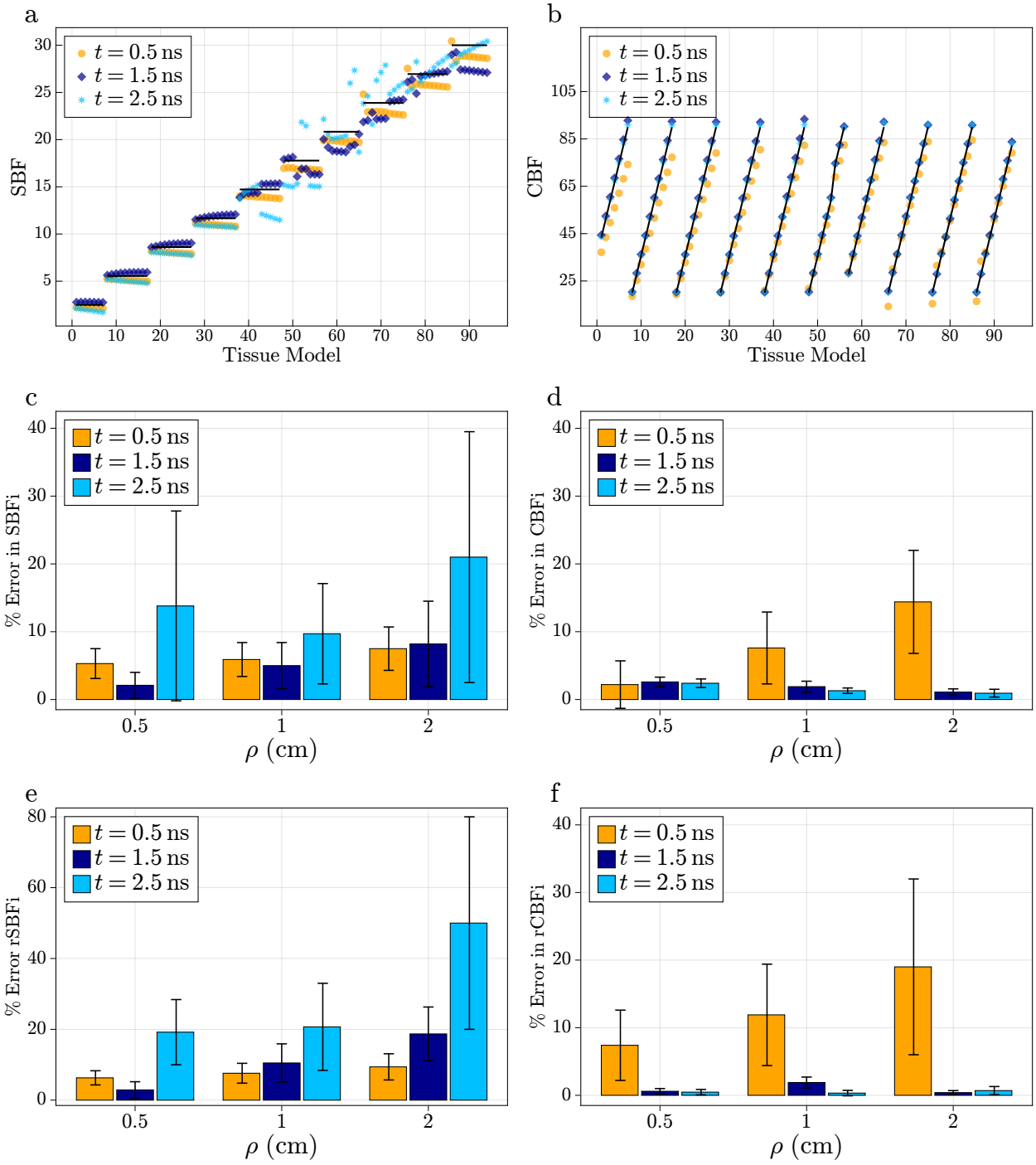

Figure 5.6: Results of the inverse fitting process when fitting the time-domain diffusion theory model to simulated $g_1(\tau, \rho, t)$ with the MC method. The recovered (a) SBF and (b) CBF coefficients are shown for three values of t when $\rho = 1$ cm where the black dashed lines represent the true flow values used in the Monte Carlo simulations. The percent error between recovered absolute values of (c) SBF and (d) CBF is averaged over all the tissue models at three source-detector separations for three t values. We show just the error using the $R_f(\rho, t)$ reflectance model as it was similar to $R(\rho, t)$. Averaged relative error normalized to the first tissue model is shown for values of (e) SBF and (f) CBF.

In Figure 5.6, the results of the inverse fitting procedure for the TD are shown. Similar to the CW domain, the inverse problem fits for two parameters, SBF and CBF. However, we show results using only the flux reflectance model, R_f, as the two reflectance models produced errors within 3% of each other for all simulations. Therefore, we focus on the recovery of the flow coefficients at time values of 0.5, 1.5, and 2.5 ns. In Fig. 5.6a and Fig. 5.6b, we report results for all 96 tissue models at a single source-detector separation of $\rho = 1$ cm for the three time values to recover SBF and CBF, respectively. Similar to the CW results, the recovery of SBF depended on the absolute SBF value as larger SBF values produced larger errors particularly for late time values. However, recovery of CBF was not affected by higher errors in recovery of SBF. As expected, shorter times were able to recover SBF better, while later times were better able to recover CBF. Rather surprisingly, the short time ($t = 0.5$ ns) also showed large sensitivity to CBF.

The resulting percent error shown in Fig. 5.6a and Fig. 5.6b between the true MC values and recovered values using diffusion theory were then averaged across all tissue models for source-detector separation of $\rho = 0.5, 1$ and 2 cm. The average error in recovered SBF and CBF for the three time values are shown in Fig. 5.6c and Fig. 5.6d, respectively. The late time value, $t = 2.5$ ns, showed the highest and most volatile error in recovered SBF. This can be explained by the inconsistent recovery at higher absolute values of SBF as shown in Fig. 5.6a. The error in recovered SBF using $t = 0.5$ and 1.5 ns was less than 10% in all the source-detector separations shown.

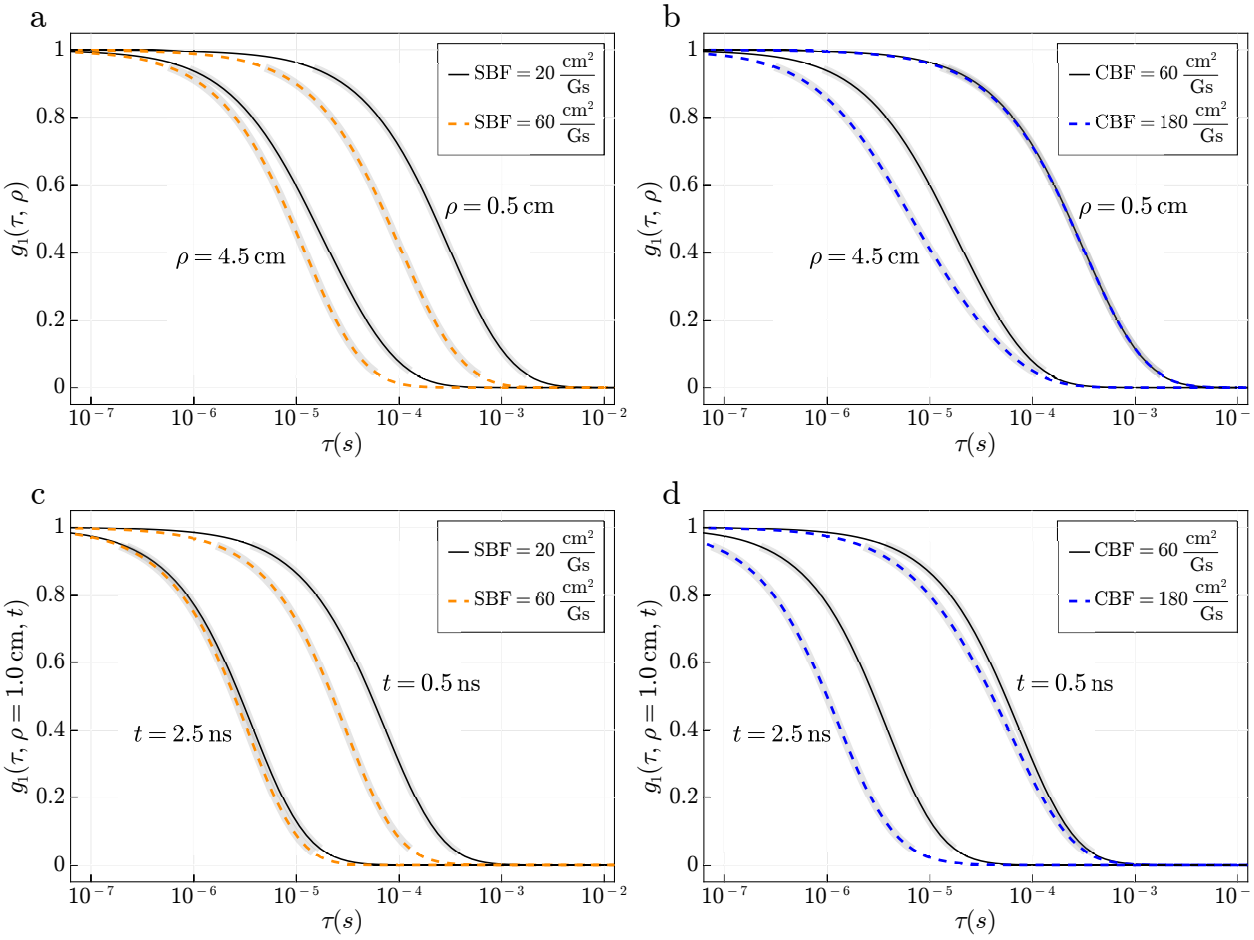

Figure 5.7: The sensitivity of the CW $g_1(\tau)$ to an increase of either (a) SBF or (b) CBF by three times at two source-detector separations. A similar example is shown in (c) and (d) for the TD $g_1(\tau)$ at a single source-detector separation ($\rho = 1$ cm) and two time values for SBF and CBF, respectively.

The recovered CBF was less than 4% at all time values when $\rho = 0.5$ cm, however for $t = 0.5$ ns the error increased at larger source-detector separations to over 10% when $\rho = 2$ cm. In Fig. 5.6e and Fig. 5.6f we show the percent error in relative changes in SBF and CBF, respectively when normalizing the starting values to the first tissue model. In contrast to the CW results, the relative errors were actually worse than absolute recovery due to the much noisier recovery of SBF at faster flow rates. Though, recovery of CBF using $t = 1.5$ and 2.5 ns was less than 2%.

To better understand the results presented in Figures 5.5 and 5.6, in Figure 5.7 we show an example flow model with baseline SBF and CBF of 20 and 60 cm/Gs, respectively in the (Fig. 5.7a and Fig. 5.7b) CW domain at two source-detector separations ($\rho = 0.5$ and 4.5 cm) and in the (Fig. 5.7c and Fig. 5.7d) TD at two delay times ($t = 0.5$ and 2.5 ns) at a single source-detector separation ($\rho = 1$ cm). The baseline optical properties are as shown in Fig. 5.1. We next increase

either SBF or CBF by three times to show the sensitivity of $g_1(\tau)$ on the two flow parameters. In the CW domain, increasing SBF by 3 times has an effect at both short ($\rho = 0.5$ cm) and long ($\rho = 4.5$ cm) source-detector separations. However, the effect is more uniform at shorter distances while longer distances are more affected at later delay times (Fig. 5.7a). On the other hand, the short distances show little effect to changes in CBF (Fig. 5.7b) except at shorter delay times. This effect is more pronounced at the longer source-detector distance where more sensitivity to CBF is observed. In the TD, the shorter delay time ($t = 0.5$ ns) shows a large sensitivity to SBF changes while showing less sensitivity to CBF. The later time ($t = 2.5$ ns) shows a much larger sensitivity to CBF while only showing a minimal though non-negligible sensitivity to SBF.

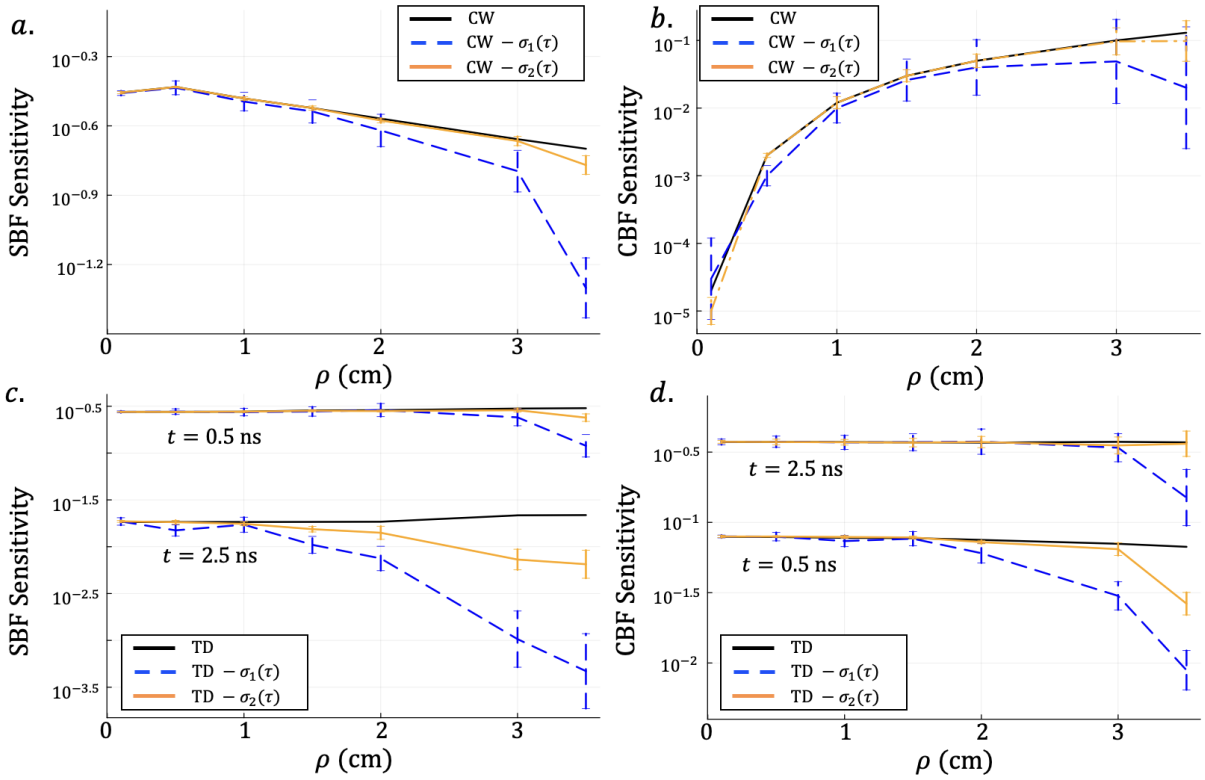

Figure 5.8: The average relative change of $g_1(\tau)$ from increasing the (left column) SBF and (right column) CBF by two times in the (top row) CW and (bottom row) TD at two photon arrival times ($t = 0.5$ and 2.5 ns) as a function of source-detector separation. Two noise models, $\sigma_1(\tau)$ and $\sigma_2(\tau)$, were considered using a collection time, T_{int}, of 1 and 5 seconds, respectively, as computed with Eq. (5.11). The CW domain shows a varying sensitivity to both SBF and CBF as a function of source-detector separation whereas the TD shows a relatively constant sensitivity.

In Fig. 5.8, we quantitatively compared the sensitivity in CW- and TD-DCS from a relative change in $g_1(\tau)$ due to a doubling in the respective flow coefficient of interest (e.g., SBF and CBF)

with other variables constant as a function of source-detector separation $\rho \in [0.1, 3.5]$ cm. The baseline optical properties and flow parameters are as described in Fig. 5.1 and Fig. 5.7. To account for variable sensitivities to SBF and CBF as a function of τ, the relative change was averaged in the window $0.05 < g_1(\tau) < 0.95$. In Fig. 5.8a and Fig. 5.8b we show the sensitivity of CW-DCS to an increase in SBF and CBF, respectively. In addition to the direct calculation of the forward model, we compute the sensitivity metric after adding noise using Eq. 5.11 with two measurement collection times, $T_{\text{int}} = 1$ and 5 labeled as $\sigma_1(\tau)$ and $\sigma_2(\tau)$, respectively. The error bars correspond to the standard deviation after averaging over 50 samples of random noise generation. In Fig. 5.8c and Fig. 5.8d the same is shown considering the sensitivity of TD-DCS to an increase in SBF and CBF at two photon delay times of $t = 0.5$ and 2.5 ns as labeled directly for each group of noise models. We note the black lines represent the sensitivity directly from the analytical model without any added noise and do not have error bars.

For the SBF sensitivity shown in Fig. 5.8a, we can see that the CW model shows the highest sensitivity to SBF at shorter distances while steadily decreasing at longer source-detector separations. However, the TD shows a relatively constant sensitivity to SBF over the whole range of ρ. In fact, the sensitivity slightly increases as we increase the source-detector distance. This can be explained by the fixed photon path length within the medium and that to maintain the same path length in the medium at longer distances from the source the average photon has to travel more in the shallower layers. On the other hand, the CW model shows an increasing sensitivity to CBF as we increase the source-detector separation (Fig. 5.8d). However, the sensitivity appears to have only logarithmic growth. As in the SBF case, the TD CBF sensitivity is relatively independent to the source-detector separation and only decreases slightly at larger distances. It was also worthwhile to observe that the TD sensitivity seems to saturate quickly (for $t > 2.5$ ns), whereby increasing the time gates only marginally increased CBF sensitivity. At larger source-detector separations the added noise model significantly affects the expected sensitivity to both SBF and CBF.

5.5 Discussion

Layered analytical models have been employed with success in CW-DCS applications to recover flow coefficients [57, 95, 168, 189] but are not typically used for TD-DCS analysis due to their increased complexity and computational cost [96]. We have validated a layered diffusion model based on our previous work [75] that allows for solving the inverse problem in both CW- and TD-DCS. The main advantages of this approach is its better numerical stability, ability to provide error tolerances, computational speed, and ability to provide fast gradient information [75]. This allows for forward simulation of the CW and TD autocorrelation function in ≈ 20 and ≈ 150 microseconds, respectively. Typically, the inverse problem for the fits shown here took < 10 and

< 250 milliseconds to fit for both SBF and CBF in the CW and TD, respectively. Although this is orders of magnitude faster than both MC simulations and previously reported layered models [60, 102, 184], using homogeneous models that only fit a single parameter are about 10x and 60x faster in the CW and TD, respectively. These reported times were all done using a single core on a personal laptop. The computational time is also linearly dependent on the number of τ values considered in the inverse problem and should be kept as sparse as possible for faster data processing. Additionally, we only considered fitting two parameters (SBF and CBF) while other coefficients were considered known. The effect of optical property errors have been previously investigated [189, 57, 79]. However, the forward model simultaneously computes both the TD reflectance along with $g_1(\tau)$, allowing it be used with TD near-infrared spectroscopy measurements to fit for optical properties along with DCS measurements to fit for flow coefficients [40, 6] with similar forward computational times.

A disadvantage of the presented model are the limitations given by the validity of diffusion theory [184]. The Monte Carlo method has become more popular as computing resources are more readily available to overcome some of the concerns of diffusion theory at short source-detector separations [184, 185]. However, we have found that the diffusion model can accurately recover absolute flow coefficients at very short separations ($\rho = 4$ mm) in the CW domain while being able to recover relative errors at even shorter separations, which is inline with previous research [172]. We investigated two equations that seek to model the reflectance as just the flux or a combination of the fluence and flux [85]. We have found that for CW measurements, using both the fluence and flux (Eq. 5.8) provides more accurate results at shorter source-detector separations and smaller values of $g_1(\rho, \tau)$. This translated to better recovered error (Fig. 5.5 c and d) at shorter separations, however this did not provide better error for source-detector separations longer than 1 cm. On the other hand, we did not find any significant differences between the two reflectance models when computing the TD autocorrelation. At short source-detector separations (≈ 2 mm), we found the time-domain model could be used more freely to model $g_1(\tau, \rho, t)$ when selecting for later arriving photons $t > 0.5$ ns (Fig. 5.4).

One of the primary reasons to use a layered model is the ability to recover and separate both extracerebral and cerebral flow changes. In the CW domain, the diffusion theory model was able to recover SBF within 10% of the Monte Carlo simulations for source-detector separations between 0.4 and 3 cm (Fig. 5.5c). The error slightly increases as we increase in source-detector separation which can be explained by the decrease in sensitivity to SBF at longer distances (Fig. 5.8a). On the other hand, increasing the source-detector separation rapidly improved the estimates of CBF which was recovered within 10% for $\rho > 2$ cm. Perhaps most interesting is the rate at which the error improves (Fig. 5.5d) in recovered CBF as we increase ρ, which could be explained by the rate at which the sensitivity to CBF increases. In Fig. 5.8b, we see an almost logarithmic

growth in sensitivity in the CW domain where a rapid rise in sensitivity is seen as we increase ρ up to 2 cm with just a smaller marginal increase after. We briefly considered a simplified noise model applied to both the CW and TD in Fig. 5.8. Although we showed steady improvements in recovered CBF at longer distances with no noise, adding noise can significantly affect sensitivities as we increase source-detector separation and decrease the measurement duration. Therefore, the marginal increase in recovered accuracy at longer source-detector separations and the decrease in expected sensitivity due to noise suggests that there is an optimal distance for measurement. In other words, the optimal distance will be after a large gain in sensitivity but short enough to maintain adequate signal to noise.

TD-DCS provides potential for better sensitivity to deeper tissues, and therefore CBF, by selecting for later arriving photons [160]. When considering just $g_1(\tau, \rho, t)$, we also demonstrated the larger sensitivity to CBF when compared to CW $g_1(\tau, \rho)$. Fig. 5.6d shows that the TD is able to recover CBF within less than 5% error between source-detector separations of 0.5 and 2 cm. A primary advantage is even using relatively short time windows of 0.5 and 1.5 ns contrast to CBF is still high. As shown in Fig 5.8b, using very late time windows doesn't substantially increase the CBF sensitivity. This is experimentally important as using shorter time windows improves signal to noise contrast, thus using moderate time gates (1-2 ns) could provide similar sensitivities to very late gates while providing more contrast. Additionally, we found that the sensitivity and CBF recovery accuracy is mostly independent of the source-detector separation. We do note that the data and sensitivities reported here are specific to the tissue geometry considered. Therefore, having a larger extracerebral layer or higher scattering coefficients could influence these results. Finally, making substantial claims on the ability of TD measurements to better quantify CBF compared to CW is difficult [27]. In Fig. 5.8b, we show a theoretical comparison based on $g_1(\tau)$ which does show that TD measurements have a much larger sensitivity to CBF when $\rho < 2.5$ cm. However, experimentally we measure $g_2(\tau)$ which can be related to $g_1(\tau)$ by the Siegert relation [43]. The effect of β in the Siegert relation can dramatically affect the sensitivities of each domain to CBF that we calculate in Fig. 5.8b and Fig. 5.8d [27, 28]. Therefore, comparing the CW and TD for experimental measurements must consider the effects of the instrument response function, coherence length, time gate, and noise. The simplified noise models we discuss in Fig. 5.8 must also consider the effect of photon arrival time and gate width which we did not consider. Future studies will focus on more rigorous noise models and their effect within the inverse problem as well as incorporating instrument response functions and finite coherence to properly compare absolute sensitivity of CW and TD measurements.

We also found that the diffusion model in both the CW and TD showed a slight offset in recovered SBF as the absolute value of SBF approached that of CBF. However, we did not find that this had any effect on recovered values of CBF. This could be explained by a more difficult in-

verse problem when the two flow coefficients have similar values, however we did not observe any crosstalk in the two coefficients as CBF was largely unaffected by these increased errors in SBF. We also note the importance of absolute SBF values in sensitivity calculations. As SBF increases, the sensitivity of both CW and TD $g_1(\tau)$ become more sensitive to changes in SBF. We show a typical physiological flow rate of SBF and CBF in Fig. 5.7 where SBF is a third of the speed of CBF. In Fig. 5.7 we can see that every $g_1(\tau)$ has some sensitivity to SBF even in the CW domain at long source-detector separations ($\rho = 4.5$ cm) and in the time-domain at long delay times ($t = 2.5$ ns). This effect is more pronounced for higher SBF values, though if SBF was much less than a third of CBF we would see less of a sensitivity to SBF. Although this fact is less important when using layered models as they can more robustly model these changes, using homogeneous models will show variable sensitivities to both SBF and CBF depending on their absolute flow rates. These findings suggest that more complicated models might be necessary even when selecting for photons of longer pathlengths and larger source-detector separations.

5.6 Conclusion

We developed and verified a diffusion based layered analytical model that can be used to recover estimates of both scalp and cerebral blood flow in real-time when using either continuous-wave or time-domain diffusion correlation spectroscopy. Utilizing a reflectance model that uses both the fluence and flux allows for absolute recovery of flow parameters at source-detector separations as short as 4 mm whereas relative recovery was demonstrated down to separations of 2 mm for continuous-wave measurements. The verified model was able to simultaneously recover SBF and CBF within 5% of Monte Carlo simulations in under 10 ms and 250 ms in the continuous-wave and time-domains, respectively allowing its use for real-time data analysis. All analysis tools are openly available online [68].

CHAPTER 6

Conclusion

6.1 Prospective and Future work

The broad goal of this thesis was to use noninvasive optical measurements to monitor and analyze hemodynamics of deep biological tissue. Major focus was placed on monitoring the brain and accounting for the contribution of surrounding superficial layers (e.g., scalp, skull, cerebrospinal fluid). This problem is typically overcome in the experimental setup and/or during data analysis. Experimentally, using multiple source-detector separations can vary the sensitivity to superficial and deeper tissues [63]. Specifically, a short source-detector separation can be used that is sensitive to only the extracerebral scalp layers. This channel can be analyzed to subtract out the sensitivity to the shallow layers of the longer separation channel. Although the short channel can be positioned to be strongly sensitive to just the shallow layers, the longer separation will always be composed of the dynamics of all the layers limiting the depth sensitivity of optical measurements.

Alternatively, time-domain measurements can be used to select for later arriving photons that increase sensitivity to deeper tissue [186]. Time-domain depth sensitivity is not dependent on the source-detector separation but the delay time of the measurement. However, both approaches are strongly limited by experimental noise which limits optical measurements to source-detector separations less than several centimeters (< 4 cm) [140]. Additionally, the multi-distance and time-domain approach cannot completely separate the effect of depth dependent optical changes when using a homogeneous model.

Time-domain reflectance spectroscopy

In Chapters 2 and 3, the time-domain approach was given significant consideration. One of the main drawbacks to time-domain systems, excluding cost, size, and setup complexity, is the necessity to account for the system's instrument response function. Theoretically, the detected measurement is simply a convolution of the IRF and the impulse response of the tissue but practically the IRF is difficult to measure. First, the IRF is a function of wavelength and detector channel so must

be independently measured for each wavelength and channel used experimentally. The IRF can change size and temporal position relative to the time the pulse enters the medium which was the focus of both Chapters 2 and 3.

Usually the forward model is developed in relation to a delta function starting at time $t = 0$. Experimentally, $t = 0$ corresponds to the time the pulse enters the medium. To analyze each time-resolved measurement, the time the pulse enters the medium has to be precisely known (within a couple of picoseconds). Practically, it is not possible to measure this for each measurement so a single measurement is taken before the experiment which is used for all subsequent data. The supercontinuum source used in this thesis was measured to be very stable as judged by analyzing IRF time scales before, immediately after, and several months after an experiment. However, even with this assumption holding true, it is difficult to precisely calibrate the start time when the probe is in reflectance geometry. Measurement of the IRF is done by reflecting the pulse from the source fiber into the detecting fiber while making sure to fill all of the modes of the detecting fiber. The finite distance that the pulse has to travel outside of the optical fibers results in a shift of the time scale that does not occur during experimental measurements when the source fiber is in direct contact with the medium. Therefore, this time shift must be accounted for in all measurements when using the measured IRF.

Much of Chapter 2 and 3 focused on the goal of avoiding this direct measurement and assuming that the time scale was unknown. The biggest difficulty with this approach is that the start time and temporal position of the detected signal strongly correlates with the scattering coefficient. In other words, the scattering coefficient determines the width and delay of the pulse where the absorption coefficient determines the slope of the later arriving photons. Removing information about the delay time of the pulse makes the inverse problem more difficult as there are now more combinations of μ_a and μ_s' that could reasonably fit the measured data. Therefore, a different constraint on μ_s' was developed using relative peak time distances.

The challenge is that the photon count rate around the peak is not always smooth and prone to noise so it is difficult to precisely measure. Measurements are collected with a finite time bin width > 10 ps, but the peak time needs to be determined more accurately which requires interpolation of sparse points to a finer grid. Using barycenters of the measured pulse would be more stable but the later arriving photons contain more information about the absorption coefficient so the barycenter becomes a looser constraint on μ_s' than the peak time. Additionally, early photons like the peak time are less accurately modeled with diffusion theory which require the use of MC lookup tables to determine the peak time difference. At this point, the analysis no longer becomes an elegant and simple way to analyze time-resolved measurements.

Other approaches were also considered that avoided lookup tables altogether. Considering an additional parameter that could shift the time scale during the optimization is a promising approach

at the cost of slightly weakening the fits (i.e., fitting for three parameters increases the complexity of the fitting procedure). Ideally, this time shift parameter could be constrained as much as possible considering the setup of the IRF measurement which could improve fit quality. In practice, this method is the simplest as it requires no calibration with other known phantoms, no generation of lookup tables, and can accommodate any uncertainty in the IRF temporal position. An alternative approach, which was not considered, may incorporate the advantages of each approach. It may be expedient to fit all the measured source-detector separations simultaneously. Two different approaches could be used in this process: (a) shift the start time of the shortest separation channel to zero while shifting the longer channels the same amount (b) use the free-fitting time shift when fitting all channels on their absolute time scale. Both approaches operate on the premise that the IRF uncertainty only affects the absolute time scale but the relative time scale between source-detector separations is accurate. However, it is still recommended to measure the temporal position of the IRF as carefully as possible to avoid any of these approaches. These approaches were never shown to match the accuracy of results with no uncertainty in the temporal position.

Multi-layer modeling

In Chapters 4 and 5, accounting for the differences in superficial and deeper tissues using a multi-layered diffusion analytical model was investigated. Multi-layer models have received some attention in the past as they are a natural extension of the widely popular semi-infinite diffusion model [153]. Broad adoption of these analytical models has been limited by their increased implementation complexity, numerical instability, increased computational time, and complex/noisier inverse problem. Some of these issues can be solved by using more computational resources but the benefit of using diffusion based approaches compared to numerical Monte Carlo methods for layered tissues become less enticing when their analysis times approach similar orders of magnitude. This has led other researchers [184] to prefer Monte Carlo modeling to diffusion theory. For example, time-domain diffusion models in layered media are typically reported to take between 0.5-1 seconds where the fastest MC results can be computed in several seconds [59, 183]. Of course, these times compare computing analytical solutions on simple desktops to the highest end GPUs and computing systems. However, the advantage of the MC method is it can handle complex shapes and real anatomical data where analytical methods are limited to planar parallel slabs.

At this point, it is important to consider the potential clinical application of the optical technology. The demand of analysis tools will depend on how long data can be acquired for and how fast the information is needed. Existing clinical optical technologies mostly rely on simpler homogeneous models as they are fast and reasonably accurate for geometries used in pulse oximetry. However, brain monitoring requires the use of more advanced data modeling [153]. Monte Carlo

methods may be adequate when diverse data can be acquired to deliver subject-specific models. For example, complex meshes based on subject's MRI scans allow for the MC method to simulate photon propagation through the subject with a high degree of accuracy [153]. An inverse approach using a multi-layered, Monte Carlo based fitting scheme was used to improve estimates of cerebral blood flow compared to traditional analytical fits [184]. This type of approach is highly advantageous for subject-specific models where the shape and thickness of each optical layer of the patient can be measured before and incorporated in the model. This type of care is slow, costly, and still requires constraints on the tissue optical properties and flow rates of other layers to limit the high dimension inverse problem. The advantage of MC over the layered based model's is primarily the inclusion of head curvature and the ability to simulate light transport in low scattering media such as the cerebrospinal fluid layer. In this work, we have shown that even in the presence of an embedded low scattering layer that diffusion theory can well approximate the RTE. Future research should focus on the degree of approximation necessary to deliver highly accurate and efficient results of brain hemodynamics. The semi-infinite approximation has been shown to be too crude but there has been some evidence that increasing the degree past a multi-layered model to a high dimension mesh may not be needed [153]. Particular focus should be given on the degree of curvature as a function of source-detector separation. All of these approaches should consider the trade off between more accuracy and data processing speed.

Ignoring the approximate geometries, the layered solutions still present some numerical difficulties. Typically they require evaluation of fractions including hyperbolic terms. When designing a numerical algorithm, premature overflows occur when the program returns infinity but the final solution can be represented in the desired precision. For example, dividing two large numbers such as $1 \times 10^{400}/1 \times 10^{200}$ should return 1×10^{200}. However, 1×10^{400} can not be represented in double precision so the program either returns an error or converts it to infinity. The other case is when both numbers in the fraction are infinity which prompts the program to return not a number (NaN) which usually occurs more frequently in the layered solutions as both numerator and denominator go to infinity. This phenomena occurs often because we must numerically transform these functions which require evaluation at large inputs. For example, $\sinh(x)$ overflows for argument $x >\approx 710$. For simple cases like calculating $\exp(x)/\exp(y)$ overflow can usually be avoided by just computing $\exp(x-y)$ instead. This becomes more complicated with more terms that add, subtract, and then divide many exponential terms. The developed programs and mathematical formulas were developed and coded with these considerations in mind while also further simplifying expressions to reduce computational time. Further optimizations are available, however, the largest performance gain will come from the exploration of vector instructions. The summations in the numerical transforms are amendable for vectorization and utilization of single instruction, multiple data (SIMD) instructions. This was partly explored and showed a decrease

of roughly 50 % in the total computational time. However, this approach requires a good vector implementation of the Bessel function which is more difficult. Additionally, more aggressive fast math operations were also investigated that showed minimum improvement in the steady-state domain while giving moderate improvement (10-20 %) in the time-domain. This can be explained by the larger increase in speed of complex arithmetic in fast math mode due to avoiding the handling of over and underflow. These type of optimizations could be further investigated to improve the performance of the algorithms further.

Additionally, future work should focus on the practical utility of the developed models for clinical analysis. The advantage of the described approach is the broad utility and practicality in several existing optical technologies in many domains of high interest (e.g., temporal and spatial domains). Existing commercial systems have primarily focused on increasing signal-to-noise while employing a homogeneous model. These simpler models have been shown to be highly sensitive to superficial tissues [153] but incorporating the presented model into these existing technologies could help improve the depth sensitivity to deeper brain tissues without using more complicated or expensive hardware. Therefore, the model should be embedded into existing technologies to improve contrast to deeper tissues. Chapter 5 demonstrated this capability in a narrow problem without noise considering fitting just two parameters. In practice, the thicknesses and scattering properties of the layers may not be known and incorporating a more complex inverse fitting scheme may be required. Finally, significant consideration to standardization and calibration across optical systems should be considered. All of the data analysis algorithms are provided open-source to help overcome some of the ongoing challenges in optical technologies for gold standard characterization of biological tissues.

6.2 Summary of major contributions

Chapter 2

- Construction of a time-domain diffuse optical spectroscopy system to recover tissue optical properties within 15 % of baselines
- Development of a heuristic approach to quickly quantify μ_s' from turbid media without knowledge of the absolute time scale of measured data

Chapter 3

- Extended analysis method developed in Chapter 2 to estimate both μ_s' and μ_a from time-resolved reflectance measurements on relative time scales within 10 % of baseline values

- Recovered absolute values of optical properties in the presence of errors in the time scale of the instrument response function

Chapter 4

- Developed an open-source and fast numerical routine to compute the steady-state, frequency domain, and time-domain fluence in a layered medium with an arbitrary number of layers
- The routine is an estimated 3 to 4 orders of magnitude faster than previously reported solutions
- Approximate solutions were also developed that can speed up solutions by an additional 10-100 times in high scattering media
- Validated model against Monte Carlo simulations in geometries of high clinical interest showing that the diffusion approximation is a good approach to model light transport through muscle and brain tissue

Chapter 5

- Developed an open-source and fast numerical routine to compute the continuous-wave and time-domain DCS signal in a layered signal
- The model was used in inverse problems to fit data at a rate of 100 Hz and 4 Hz in the CW- and TD-DCS showing for the first time using a layered model to fit TD-DCS data.

6.3 Summary of other published work

This dissertation contained reprints of my first author published peer-reviewed work [70, 75, 72, 74]. In addition, a contribution as coauthor to other peer-reviewed work was also made [92] which focused on developing and combining diffuse correlation spectroscopy and diffuse reflectance spectroscopy in a portable and compact way to quantitatively monitor blood perfusion. My primary contribution to this work was in analysis of the DCS measurements and bench-top validation of the instrument using optical phantoms. Many conference proceedings were also contributed as first author [73, 76, 69, 71] and co-author [117, 179, 135, 136, 91] which contain supporting details to the peer-reviewed work. Finally, much of the developed software is available open-source for diffuse optics (https://github.com/heltonmc/LightPropagation.jl), inverse Laplace transforms (https://github.com/heltonmc/Laplace.jl), and for computing special mathematical functions (https://github.com/JuliaMath/Bessels.jl).

APPENDIX A

Light Diffusion in Homogeneous Medium

The numerical implementations of solutions to the diffusion equation for homogeneous semi-infinite and slab media are discussed. The development of more accurate solutions is required for use in the approximate solutions derived for layered media in Chapter 4. Cancellation can occur when subtracting particular and homogeneous solutions of the layered equations resulting in loss of relative tolerance. Therefore, it is necessary to develop a code to compute the semi-infinite solution with as much accuracy as possible. Some of these techniques were also used in the development of the layered code and have broad applicability to any translation of mathematical formulas to computer implementations.

The following contains just the salient techniques used to code the semi-infinite and slab solutions for steady-state sources. These techniques can also be applied to the time-domain solutions as they have similar structure. Code snippets will be shown for these simpler cases to highlight the technique, however, the full code for time-domain solutions in more domains can be found at https://github.com/heltonmc/LightPropagation.jl.

The Green's function solution to the steady-state diffusion equation [109] in a media bounded by parallel planes (i.e., slab) is

$$\Phi(\vec{r}) = \frac{1}{4\pi D}\sum_{m=-\infty}^{m=+\infty}\left\{\frac{\exp(-\mu_{eff}\sqrt{\rho^2+(z-z_m^+)^2})}{\sqrt{\rho^2+(z-z_m^+)^2}} - \frac{\exp(-\mu_{eff}\sqrt{\rho^2+(z-z_m^-)^2})}{\sqrt{\rho^2+(z-z_m^-)^2}}\right\} \quad \text{(A.1)}$$

where $\vec{r}$ is the position vector, ν is the speed of light in the medium, and t is the time. μ_s', μ_a, and $D \cong 1/(3\mu_s')$ are the reduced scattering coefficient, absorption coefficient, and diffusion coefficient, respectively. The sources are placed along the z-axis with locations $z_m^+ = 2m(s + 2z_b) + z_0$ and $z_m^- = 2m(s + 2z_b) - 2z_b - z_0$ with $z_b = 2AD$ and $z_0 = 1/\mu_s'$. s is the thickness of the slab between the bounded parallel planes.

The solution is obtained through the method of images using an extrapolated boundary condition where we assume the fluence equal to zero on on an extrapolated surface $2AD$. The semi-infinite medium ($s = \infty$) is a special case requiring only the first dipole ($m = 0$). The following code is a naive implementation of the semi-infinite solution.

Listing A.1: Naive implementation for the CW fluence in a semi-infinite medium

```
function fluence_DA_semiinf_CW(r, mua, musp; z = 0.0)
    mueff = sqrt(3 * mua * musp)
    D = 1 / (3 * musp)
    z0, zb = 1 / musp, 2 * D

    phi = exp(-mueff * sqrt(r^2 + (z - z0)^2))
        / (sqrt(r^2 + (z - z0)^2))
    phi -= exp(-mueff * sqrt(r^2 + (z + 2 * zb + z0)^2))
        / (sqrt(r^2 + (z + 2 * zb + z0)^2))

    return phi / (4 * pi * D)
end
```

Numerical implementations of method of image like solutions must be examined to limit floating point errors. In particular, subtracting terms of similar magnitude (the dipole term) can lead to cancellation. This error will increase as the terms z_m^+ and z_m^- become similar and can be examined by comparing the results computed in higher precision to those obtained in double precision. The absolute error can be quantified by taking the absolute difference, $\text{abs. error} = |y_{big} - y_{double}|$, of the computed values while the relative error $\text{rel. error} = |1 - y_{big}/y_{double}|$ can be used to estimate approximately the number of digits of accuracy. In general, we are more interested in the relative errors while absolute error can be useful in functions that oscillate around zeros.

Fig. A.1 shows the computed fluence on the top boundary ($z = 0$) in a semi-infinite medium with constant $\mu_a = 0.1\ \text{cm}^{-1}$ for three $\mu_s' = 10.0, 50.0, 1000.0\ \text{cm}^{-1}$. The absolute and relative errors compared to the computation done in octuple precision are shown in the below plots.

The resulting fluence (top plot on log scale) decreases significantly for larger scattering coefficients while the absolute error (middle plot) decreases proportionally. The main feature is that as the scattering coefficient increases the terms $z_m^+ \approx z_m^-$ become similar leading to potentially more cancellation. This is shown more explicitly in the relative errors (bottom plot) which are between $10^{-14} - 10^{-13}$ and $10^{-10} - 10^{-9}$ for $\mu_s' = 10$ and $1000\ \text{cm}^{-1}$, respectively. The exponent of the relative error corresponds to roughly the number of digits of accuracy retained where a relative error near $\approx 2 \times 10^{-16}$ corresponds to a perfectly rounded result (i.e., the computation suffers from no floating point errors).

It is important to consider what tolerances are desirable for the specific application. Though not always true, any improvement in the numerical accuracy will come at some cost either in development time or computational efficiency. The user only experiences increased runtimes but at the gain of extra precision in the results where the development time is a single upfront cost. In

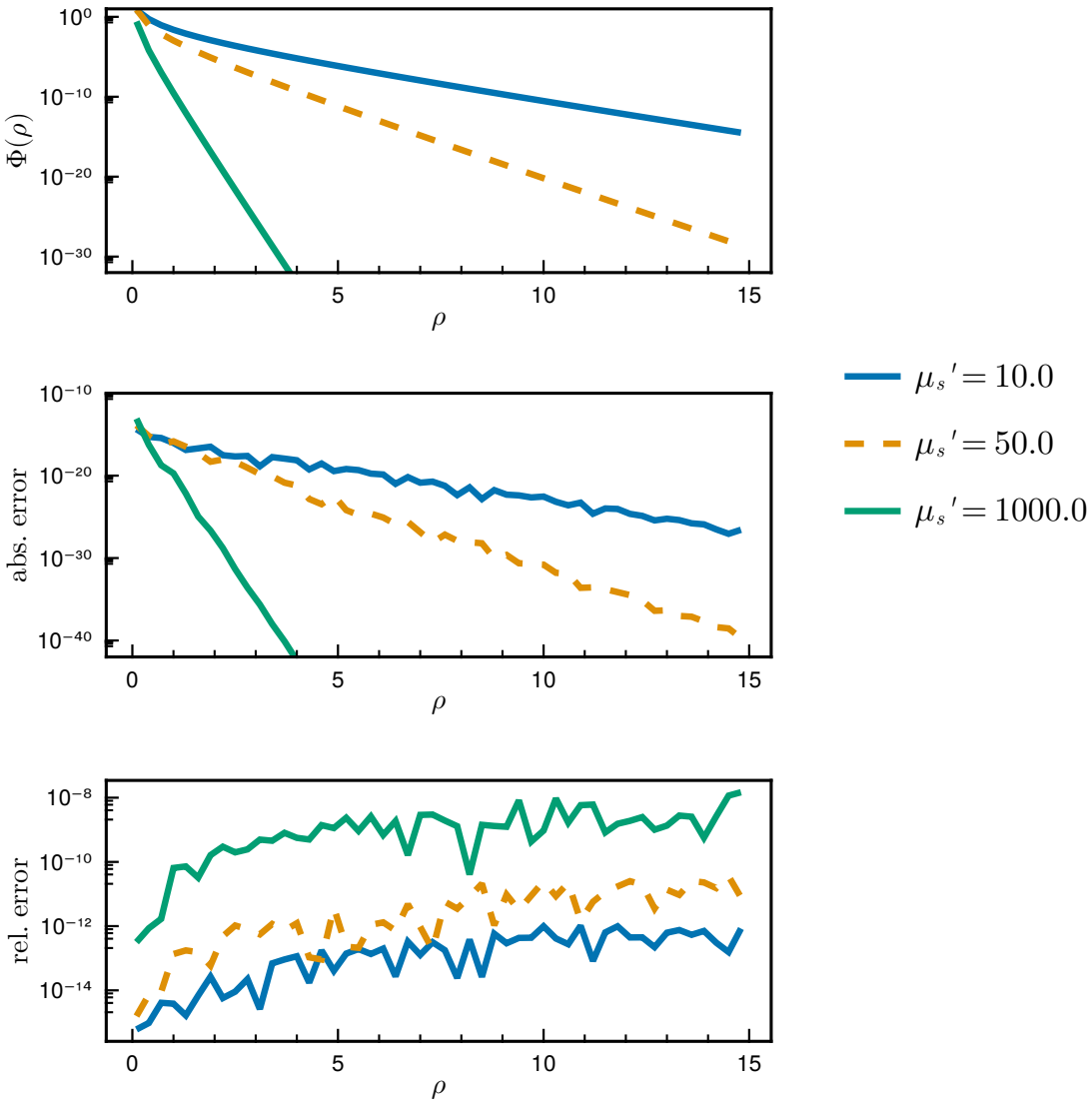

Figure A.1: (top) Steady-state fluence calculated in high precision for a semi-infinite medium with three scattering coefficients. The (middle) absolute and (bottom) relative error between the naive implementation and higher precision routine.

this case, for $\mu_s' = 10\ \mathrm{cm}^{-1}$ the accuracy is better than 1 part per trillion which is vastly superior to any experimental uncertainty. Therefore, the consideration must be at what point does the result become *catastrophic*.

Usually it depends what the results of the computation are used for. Is that the final number? Do we need that number in other computations? A good example of this is when we compute the solution to the slab. Now, many of these dipole sources must be infinitely summed. Of course in practice this sum is rapidly convergent (≈ 5 terms) and cancellation is minimal as each successive

term is orders of magnitude less. The following is a naive implementation of the slab solution.

Listing A.2: Naive implementation for the CW fluence in a slab medium

```
function fluence_DA_slab_CW(r, mua, musp; z = 0.0, s = 1.0, xs = 30)
    D, z0 = 1 / (3 * musp), 1 / musp
    zb = 2*D
    mueff = sqrt(3 * mua * musp)
    return _sum_fluence_DA_slab_CW(xs, s, zb, z0, r, z, mueff, D)
end

function _sum_fluence_DA_slab_CW(xs, s, zb, z0, r, z, mueff, D)
    phi = zero(eltype(mueff))

    for m in -xs:xs
        phi += _kernel_fluence_DA_slab_CW(m, s, zb, z0, r, z, mueff)
    end

    return phi / (4 * pi * D)
end

@inline function _kernel_fluence_DA_slab_CW(m, s, zb, z0, r, z, mueff)
    tmp1 = 2 * m * (s + 2 * zb)
    zmp = tmp1 + z0
    zmm = tmp1 - 2 * zb - z0

    a = sqrt(r^2 + (z - zmp)^2)
    b = sqrt(r^2 + (z - zmm)^2)

    phi = exp(-mueff * a) / a
    phi -= exp(-mueff * b) / b
    return phi
end
```

The implementation is fairly straightforward and just an extension of the semi-infinite solution to sum over many source terms. Following a similar error analysis performed for the semi-infinite medium, we show the fluence, absolute error, and relative error in a slab medium on the top surface ($z = 0$) in a medium of constant absorption $\mu_a = 0.1$ with three scattering coefficients $\mu_s' = 10, 50, 100$. In this case we considered a slab thickness of 0.5 cm and used 50 terms in the

summation.

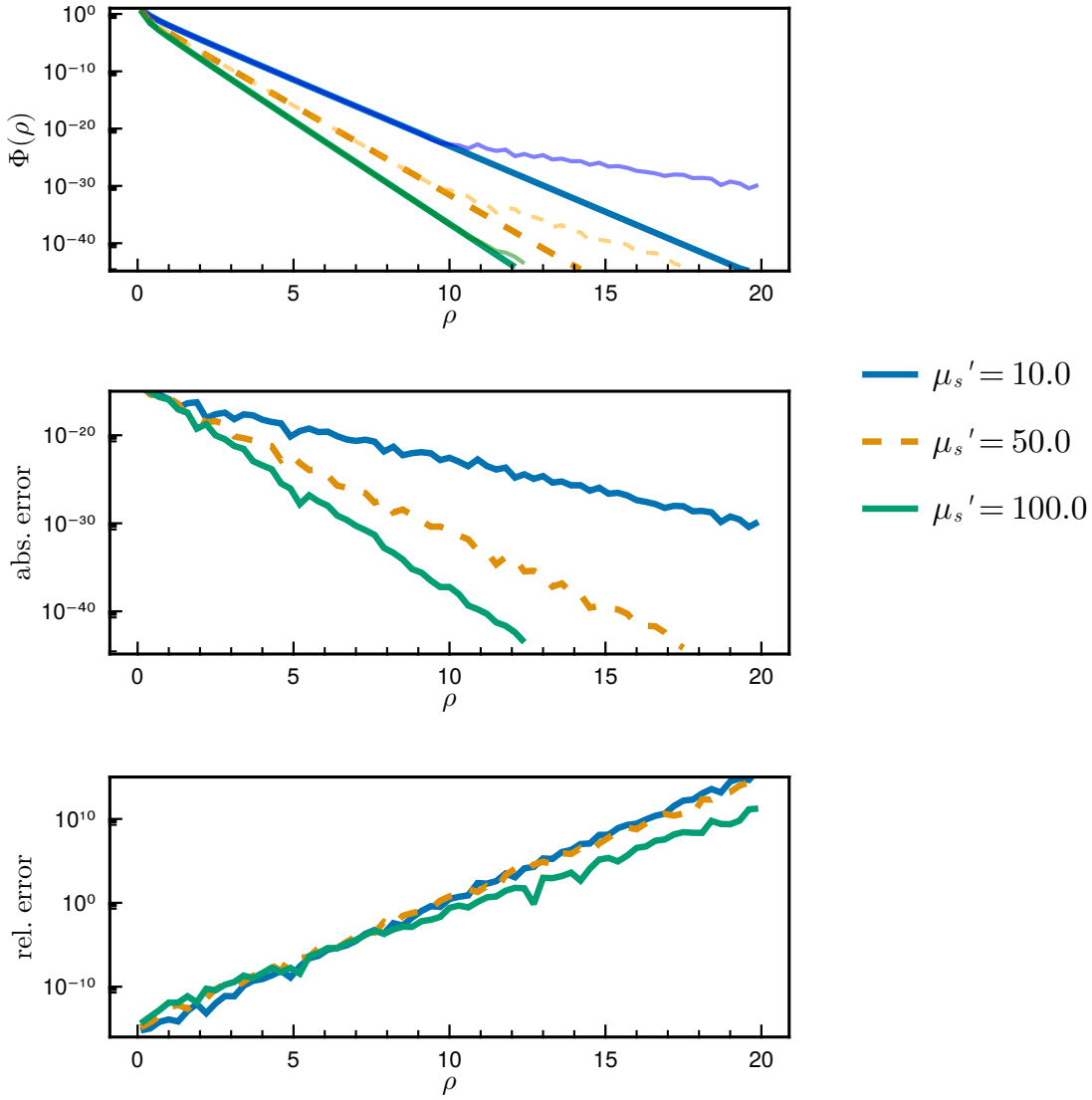

Figure A.2: (top) Steady-state fluence calculated in high precision for a slab medium with three scattering coefficients. Faint lines show the calculation in double precision where solid lines show computation in higher precision. The (middle) absolute and (bottom) relative error between the naive implementation and higher precision routine.

In the top plot of figure, the fluence is shown including both the fluence calculated in higher precision (dark lines) and the fluence calculated in double precision (faint lines). Here, we begin to see a deviation between computed results at smaller values. The absolute error is still decreasing (at a slower rate than the fluence) but the relative errors dramatically increase as a function of source-detector separation. Now instead of errors better than one part per trillion there are instances where

not a single digit of accuracy is retained.

Now, of course, a specific example was chosen to highlight this fact as small slab thicknesses (< 1 cm) are particularly prone to high numerical errors. It may not be obvious why that is the case but it is important to note that the scattering coefficient did not have the same effect on the relative errors as it did in the semi-infinite case. The thickness s only appears in the calculation of the source locations z_m^+ and z_m^- similar to the scattering coefficient but the value does not affect the difference in value of the computed terms like the scattering coefficient. So the original observation that these two terms become similar leading to more cancellation does not apply. In fact, if we are summing positive terms each with their own error of 14 digits and each consecutive term is decreasing we do not expect the error to increase as dramatically shown in the figure.

So what is going on here? Physically, it might help to consider the relation between the semi-infinite model and the slab model. Remember that the semi-infinite model is a special case corresponding to just the $m = 0$ term which has no dependence on the slab thickness s. Therefore, the expression corresponds to computing the semi-infinite solution and then subtracting the loss of light from the finite s. As s gets smaller, the loss of light becomes larger and the medium becomes less semi-infinite. However, because the computed term $m = 0$ doesn't depend on s the value of the summation considering all the terms besides $m = 0$ starts to approach the value of just $m = 0$ which must be subtracted. Even if we can compute the difference of individual dipoles exactly we are still limited by the final subtraction of all the terms from $m = 0$.

Is there anything we can do about this? Bringing the attention back to the semi-infinite case where the problem can be pretty easily simplified. We must essentially compute $e^{-ax}/a - e^{-bx}/b$ as accurately as possible with a and b of similar value. Each individual exponent can be computed fairly exactly so it is the subtraction that must be avoided. However, the rounding of each term before the subtraction leads to the error. We can avoid this by rearranging the formula through factoring into a relation that tries to compute the terms before any rounding occurs. Essentially, we must have some way of looking at the difference of $a - b$ before computing the exponent of individual values. One implementation is as follows by factoring out terms and using the expm1 function along with fused multiply adds.

Listing A.3: Improved implementation for the CW fluence in a semi-infinite medium

```
function fluence_DA_semiinf_CW(r, mua, musp; z = 0.0)
    mueff = sqrt(3 * mua * musp)
    D = 1 / (3 * musp)
    z0, zb = 1 / musp, 2 * D
    return _kernel_fluence_DA_semiinf_CW(mueff, r, z, z0, zb, D)
end
function _kernel_fluence_DA_semiinf_CW(mueff, r, z, z0, zb, D)
```

```
    a = hypot(r, z - z0)
    b = hypot(r, z + 2 * zb + z0)

    # the following tries to compute phi = exp(-mueff * a) / a - exp(-
   mueff * b) / b more accurately
    # h also tries to compute h = b - a more accurately
    h = 4 * (z0 * z + z0 * zb + z * zb + zb^2) / (a + b)
    phi = exp(-b * mueff) * fma(b, expm1(h * mueff), h) / (b * a)
    return phi / (4 * pi * D)
end
```

The previous code listing contains some key differences from the first implementation of the semi-infinite fluence. One is the particular absence of any subtractions. The subtraction is embedded within the expm1 function which computes $e^x - 1$ with a polynomial approximation avoiding any loss of significance from the subtraction for small values of x. Another difference is using the hypot function to compute $\sqrt{|x|^2 + |y|^2}$ more accurately while avoiding underflow. This change affects the final outcome less because we are only using it to compute the product and sum of two hypotenuses which is not a major source of error. However, this is due to being able to analytically compute the difference of hypotenuses (through conjugation) analytically as a sum of different terms instead of having to compute the differences of square roots. Fig. A.3 shows a comparison between the improved version and initial naive implementation considering a similar setup with $\mu_s' = 100.0$.

This method suffers from almost no cancellation giving results that are between 4-5 digits more accurate. It is important to note the performance differences as the naive and improved version run in roughly 110 and 135 clock cycles which takes roughly 30 and 37 nanoseconds, respectively, to compute the fluence at a single time point. This is roughly 23 % slower to gain around 4-5 digits more accuracy. This trade off is most of the time worth it.

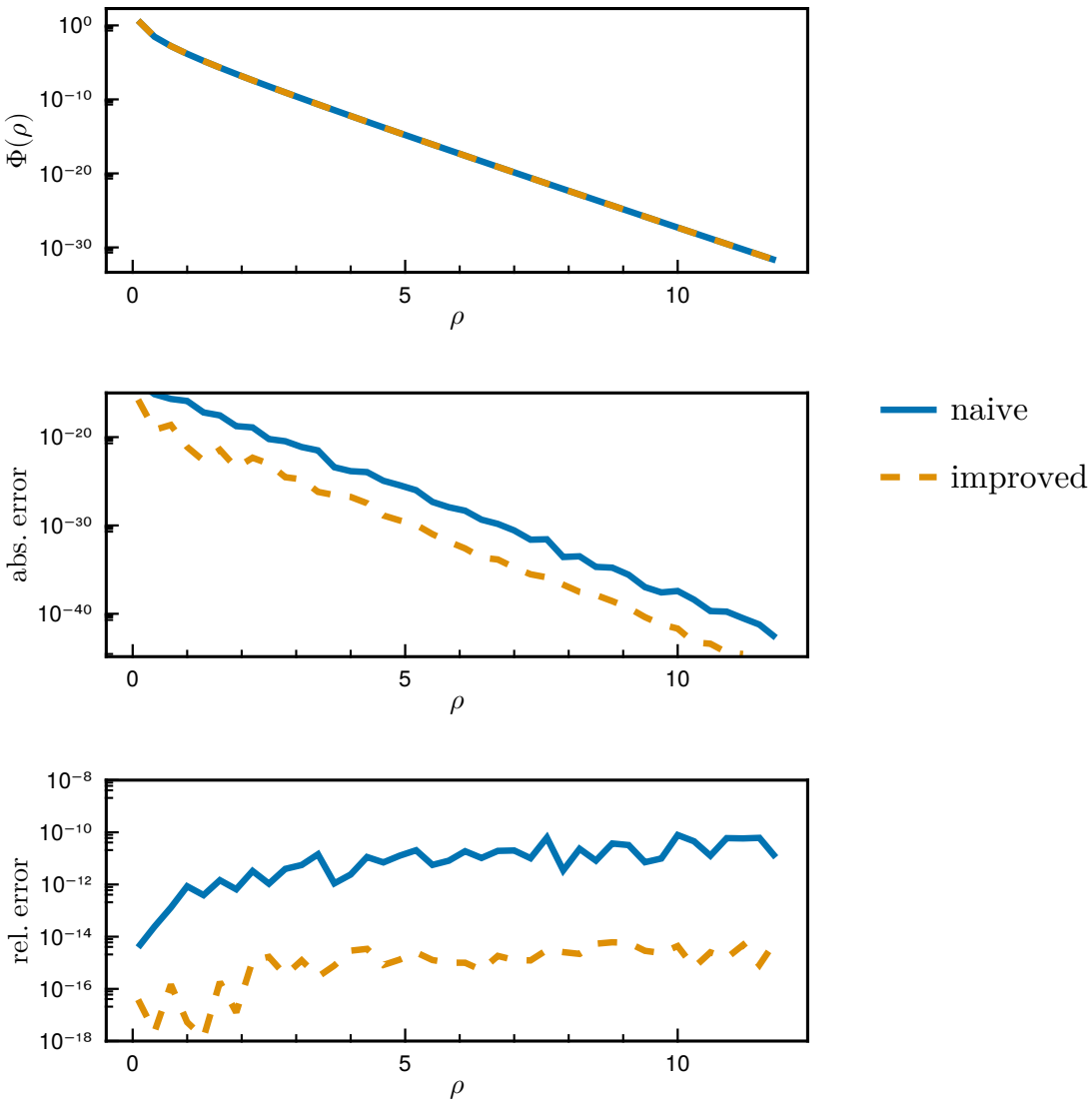

Figure A.3: (top) Steady-state fluence calculated in a semi-infinite medium computed with the improved and naive implementation. The (middle) absolute and (bottom) relative error between the naive and improved implementation compared to the higher precision routine.

APPENDIX B

Inverse Laplace Transforms

A brief comparison of the Fourier and Laplace transform will be presented using the infinite space Green's function. This function is used because the numerical inversion can be directly compared to its known analytical form. Additionally, solutions in other geometries such as the semi-infinite and layered solutions present similarly.

The significance of this discussion is that analytical solutions in the time-domain are limited to relatively simple geometries such as infinite, semi-infinite, and slab geometries. In layered media or in higher order solutions to the radiative transport equation, analytic solutions are not easily derived relying on numerical transforms for computation given a known solution in the spatial or spatial-frequency domain.

The predominate way to perform the transform from the frequency domain to the time-domain is of course the Fourier transform given below.

$$f(t) = \frac{1}{2\pi} \int_{-\infty}^{\infty} F(\omega) e^{i\omega t} d\omega \tag{B.1}$$

Therefore, the time-domain infinite space Green's function can be calculated by numerically performing the Fourier transform of the frequency domain solution. A simple computer code to compute this using adaptive 1-D Gauss-Kronrod quadrature is as follows.

Listing B.1: Code to compute the Fourier transform with adaptive numerical integration

```
fluence_DA_inf_CW(rho, mua, musp) = 3 * musp * exp(-sqrt(3 * musp * mua
   ) * rho) / (4 * pi * rho)
function fluence_DA_inf_FD(rho, mua, musp; omega = 0.0)
    mua_complex = mua + omega * im / 29.9792458
    return fluence_DA_inf_CW(rho, mua_complex, musp)
end

# using the external library QuadGK.jl
using QuadGK
```

```
TD_fluence_fourier(t, rho::T, mua::T, musp::T; rtol=sqrt(eps(T)),
   maxevals=1e7) where T = real.(quadgk(omega -> 1/pi * exp(im*omega*t)
    * fluence_DA_inf_FD(rho, mua, musp; omega = omega), zero(T), T(Inf)
   , rtol=rtol, maxevals=maxevals)[1])
```

Considering a simple example with $\rho = 1$ cm, $\mu_a = 0.2\ \mathrm{cm}^{-1}$, and $\mu_s' = 12.0\ \mathrm{cm}^{-1}$, we can compare the absolute and relative error of the numerical inversion of the Fourier transform to the exact analytical solution in Fig. B.1

In this example we considered the error as a function of time $t \in (0.01, 5.0)$ using different numbers of Fourier space evaluations during the numerical transform $N = 500, 5000, 50000, 5000000$. First, a large number of evaluations ($N > 5,000$) are required to reach absolute errors below 1×10^{-8} whereas over $50,000$ evaluations are needed to reach absolute errors below 1×10^{-15}. The nature of these transforms which evaluate functions at many different orders of magnitude in inputs limit the absolute error to a minimum of the machine precision. Therefore, to achieve absolute errors below $\approx 2 \times 10^{-16}$, higher precision is needed.

Alternatively, the inverse Laplace transform can be used which has the promise of forcing a more rapid decay of the integrand [89].

$$F(s) := \int_0^\infty e^{-st} f(t) dt, \qquad Re(s) > \sigma_0 \tag{B.2}$$

where $F(s)$ is computable on the real axis only and σ_0 is the abscissa of convergence of $F(s)$. Using a Bromwhich contour along a hyperbola, we can compute the time-domain signal from the Laplace space [106].

Listing B.2: Code to compute the inverse Laplace transform along a hyperbola contour

```
function hyperbola(f::Function, t::T; N::Int = 16) where T
    a =  zero(Complex{T})
    h = T(1.081792140) / N
    for k in 0:N-1
        sk, dsk = s((k + T(0.5)) * h, N, t)
        a += f(sk) * exp(sk * t) * dsk
    end
    return imag(a) * h / pi
end

function s(theta, N, t::T) where T
    mu = T(4.492075287) * N / t
```

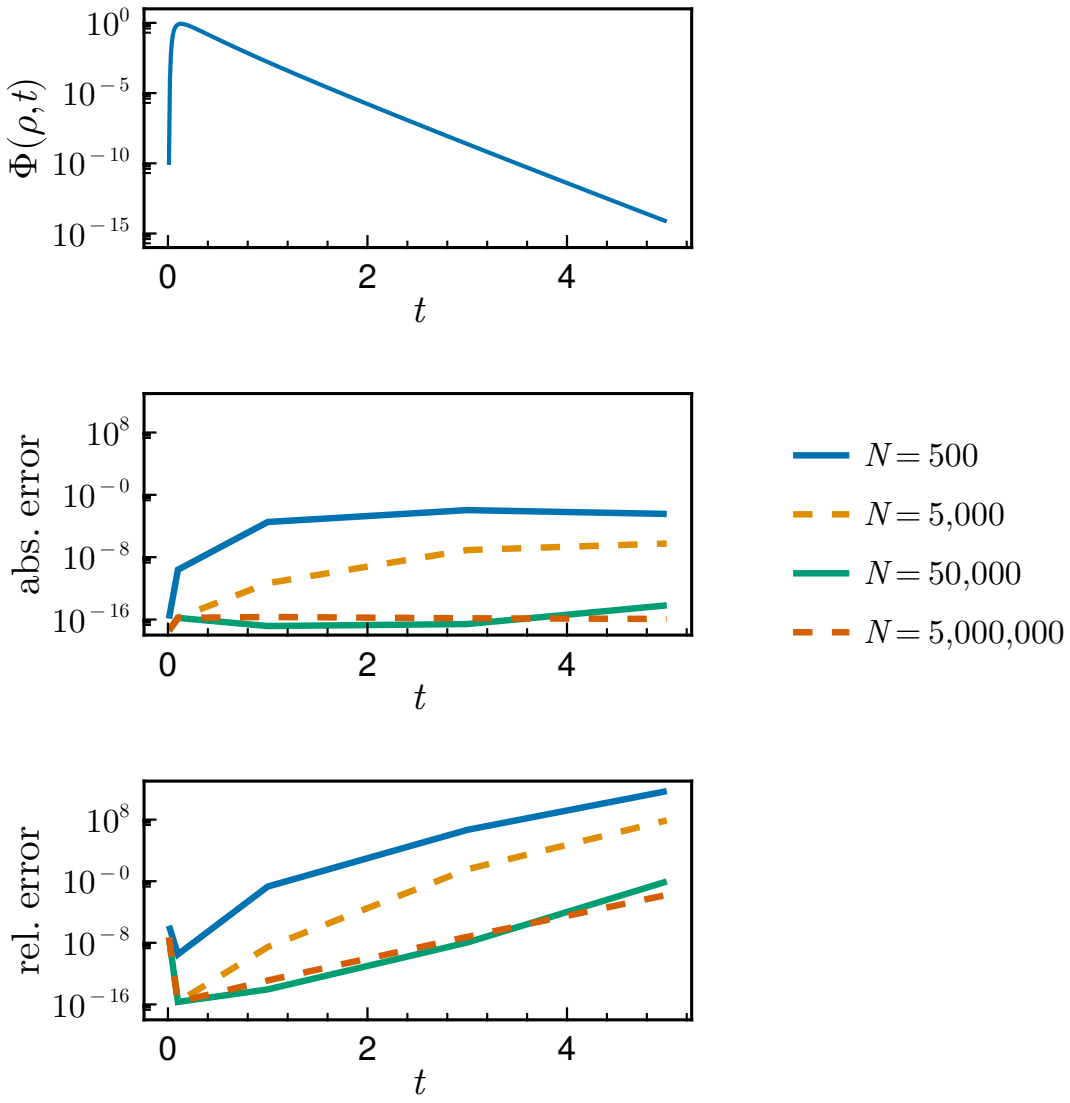

Figure B.1: (top) Time-domain fluence computed with the exact analytical solution. The (middle) absolute and (bottom) relative error between the numerical Fourier transform using a different number (N) of terms and the exact analytical solution computed in higher precision.

```
    phi = T(1.172104229)
    a = theta + im * phi
    s = mu + im * mu * sinh(a)
    ds = im * mu * cosh(a) # derivitive of hyperbola contour
    return s, ds
end

# use the solution in the steady-state space
```

```
t = 0.5:0.5:5.0
y1 =map(t -> hyperbola(s -> fluence_DA_inf_CW(rho, mua + s /
   29.9792458, musp), t, N=12), t)
```

In Fig. B.2, the example used for the Fourier transform is repeated but this time only using $N = 4, 8, 16, 24$ Laplace space evaluations for the numerical inversion of the Laplace transform.

In this case, the absolute error is relatively flat across all time points while being a function of the number of evaluations used. Similarly to the Fourier transform a the absolute error is lower bounded by the machine precision of the calculation. Increasing the number of evaluations beyond this point does not improve the error. In general, there is an optimal number of evaluations and increasing past this point actually increases the error. The big difference is that the Fourier transform requires over 3,000 times more evaluations than the inverse Laplace transform to reach the same minimum absolute error.

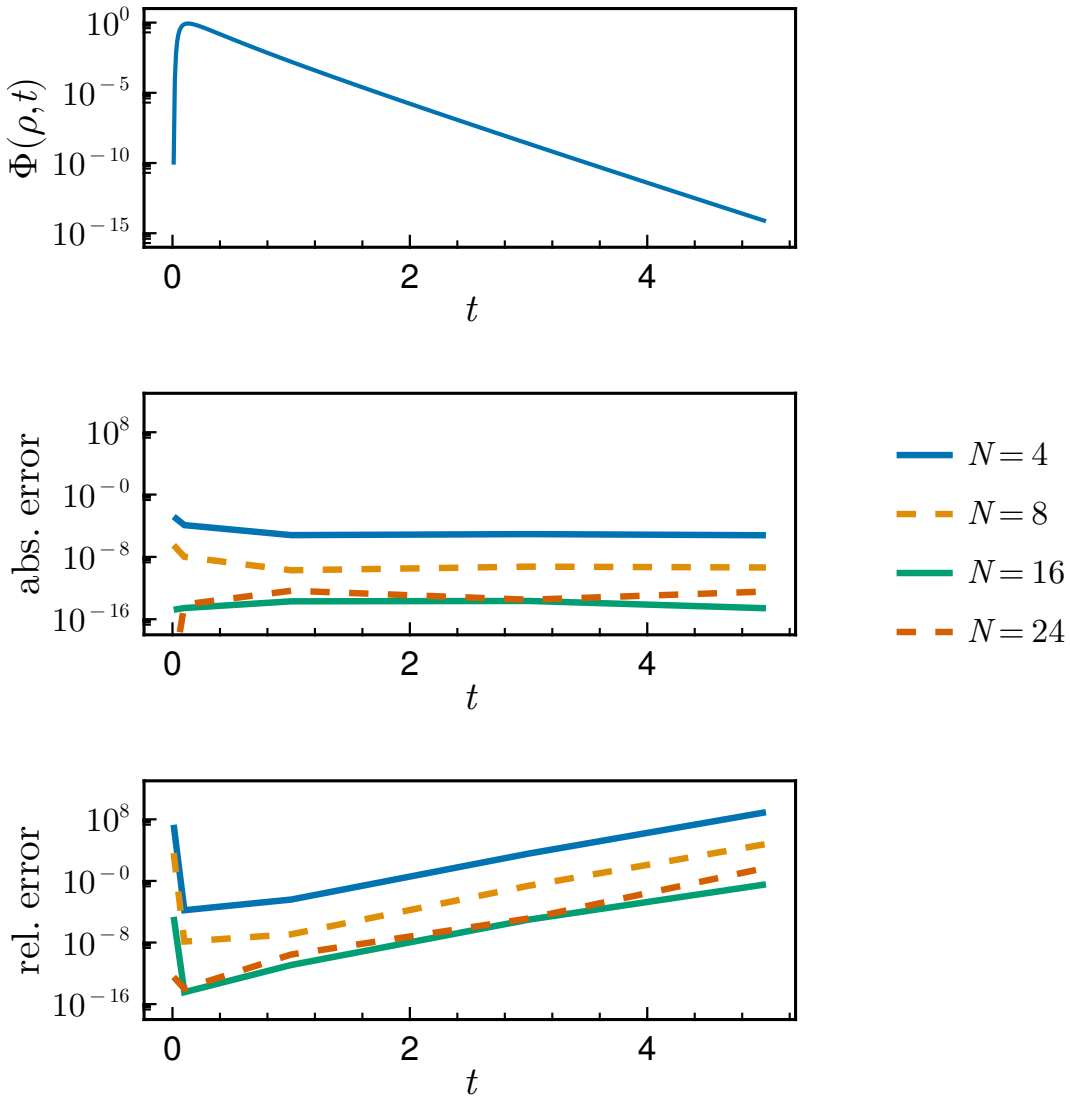

Figure B.2: (top) Time-domain fluence computed with the exact analytical solution. The (middle) absolute and (bottom) relative error between the numerical inverse Laplace transform using a different number (N) of terms and the exact analytical solution computed in higher precision.

APPENDIX C

Bessel Functions of the First Kind

The implementation of the layered diffusion approximation included a custom routine to compute the Bessel function of the first kind and zero order, $J_0(x)$, which is available at https://github.com/JuliaMath/Bessels.jl. As mentioned in Chapter 4, this function must be computed several hundreds to thousands of times and can require over 60 % of the total runtime. The original implementation of $J_0(x)$ was derived from FDLIBM and was accessed through openlibm (https://github.com/JuliaMath/openlibm).

A new implementation of $J_0(x)$ was developed following the methods given in [66]. This approach works by using asymptotic expansions for large arguments and custom minimax polynomials around the function zeros for moderate arguments. In Fig. C.1, the absolute error between the two routines is shown when compared to an arbitrary precision routine for 100,000 random points between 0 and 200. The error is normalized by the machine precision (eps). The absolute error here is relevant as the function oscillates around zero and is always less than 1. This routine maintains better absolute error criteria than FDLIBM with a maximum error of $\approx 1.06 \times 10^{-16}$. The full distribution of the errors for all 200 points is shown in Fig. C.1. For all these comparisons Julia v1.8.2, Bessels.jl v0.2.7, and SpecialFunctions.jl v1.8.7 were used with a Linux (x86-64-linux-gnu) operating system and a CPU of an Intel Core i7-8700k 3.70 GHz.

As mentioned in Chapter 4, the computation of the Bessel function limits the routine to absolute errors approaching the machine precision. This is not indicative of a poor quality implementation of the Bessel function but that rounding of arguments before computing the Bessel function limits the overall accuracy. This can not be avoided unless all computations are done in higher precision as the loss of relative accuracy in the Bessel function propagates through the result.

Next, we compare the runtime to compute a Bessel function for each implementation. The benchmarking code is included in the following listing which mimics the structure of the layered diffusion code by accumulating a sum of random Bessel function computations. There are two instances that should be checked as it can be controlled in what order the arguments of the Bessel function are computed in. For example, the roots of the Bessel function are stored in order, therefore the argument will always be increasing. This is important as the Bessel function has different

routines depending on the argument range where the asymptotic expansion for large arguments is much more efficient. This consideration is important to improve the accuracy of branch prediction in the algorithm

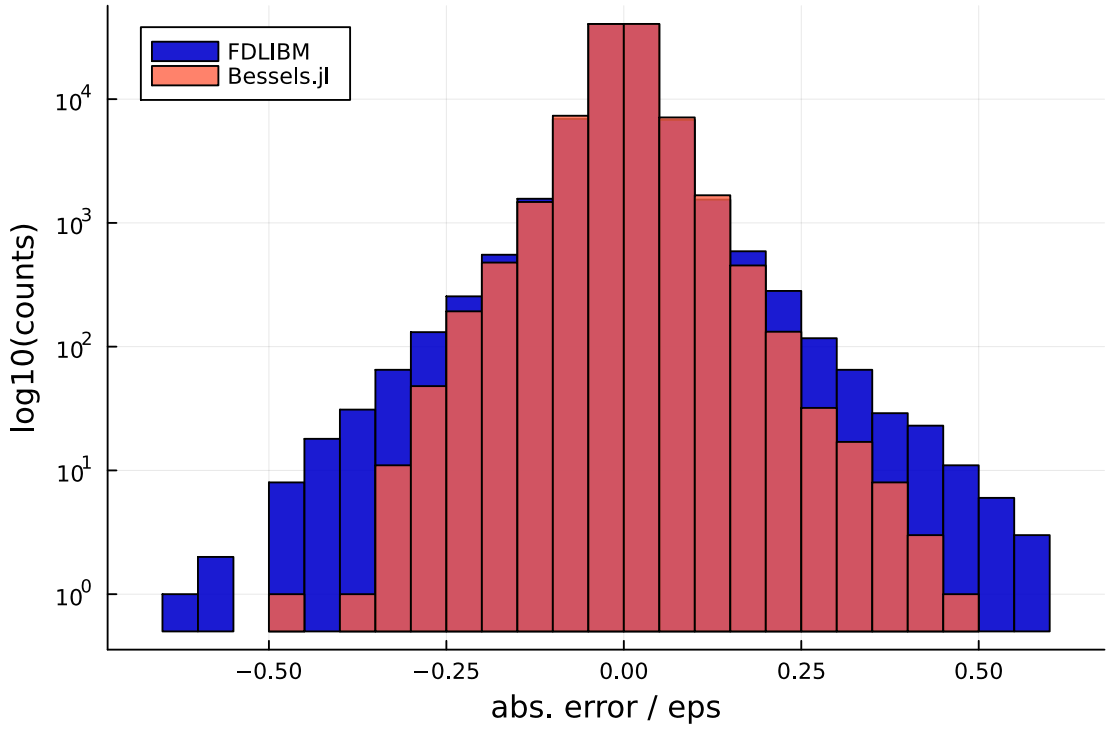

Figure C.1: Comparison of the error between a custom implementation (Bessels.jl) and the implementation provided by FDLIBM for computation of the Bessel function of the first kind and zero order, $J_0(x)$.

Listing C.1: Benchmark for $J_0(x)$

```
function bench(f; N=50000000, Order=false)
    v = rand(N)*200
    if Order
        v = sort(v)
    end
    a = 0.0

    tstart = time()
    for _x in v
        a += f(_x)
    end
```

```
    tend = time()
    t = (tend-tstart) / N * 1e9
    return t, a
end

julia> bench(Bessels.besselj0)
(26.881136894226074, 235817.69395194543)

julia> bench(SpecialFunctions.besselj0)
(59.89438056945801, 238316.6774025267)

julia> bench(Bessels.besselj0, Order=true)
(16.909656524658203, 235914.11526594945)

julia> bench(SpecialFunctions.besselj0, Order=true)
(52.68270015716553, 235795.06369727102)
```

Averaging the results, its takes approximately 27 nanoseconds and 17 nanoseconds on average to compute a single Bessel function over an unsorted and sorted array, respectively. For comparison the FDLIBM routine takes approximately 60 and 53 nanoseconds corresponding to the custom implementation being 2.2 times and 3.1 times faster.

BIBLIOGRAPHY

[1] Marvin L Adams and Edward W Larsen. Fast iterative methods for discrete-ordinates particle transport calculations. *Progress in nuclear energy*, 40(1):3–159, 2002.

[2] Erik Alerstam, Stefan Andersson-Engels, and Tomas Svensson. Improved accuracy in time-resolved diffuse reflectance spectroscopy. *Optics express*, 16(14):10440–10448, 2008.

[3] DEv Amos. Algorithm 644: A portable package for bessel functions of a complex argument and nonnegative order. *ACM Transactions on Mathematical Software (TOMS)*, 12(3):265–273, 1986.

[4] Simon R Arridge, M Cope, and DT Delpy. The theoretical basis for the determination of optical pathlengths in tissue: temporal and frequency analysis. *Physics in Medicine & Biology*, 37(7):1531, 1992.

[5] Peter Atkins and Julio De Paula. *Physical chemistry*. Macmillan, 2002.

[6] Wesley B Baker, Ramani Balu, Lian He, Venkaiah C Kavuri, David R Busch, Olivia Amendolia, Francis Quattrone, Suzanne Frangos, Eileen Maloney-Wilensky, Kenneth Abramson, Elizabeth Mahanna Gabrielli, Arjun G Yodh, and W Andrew Kofke. Continuous non-invasive optical monitoring of cerebral blood flow and oxidative metabolism after acute brain injury. *Journal of Cerebral Blood Flow & Metabolism*, 39(8):1469–1485, 2019.

[7] Wesley B Baker, Ashwin B Parthasarathy, Tiffany S Ko, David R Busch, Kenneth Abramson, Shih-Yu Tzeng, Rickson C Mesquita, Turgut Durduran, Joel H Greenberg, David K Kung, and Arjun G Yodh. Pressure modulation algorithm to separate cerebral hemodynamic signals from extracerebral artifacts. *Neurophotonics*, 2(3):035004, 2015.

[8] Alex H Barnett. A fast numerical method for time-resolved photon diffusion in general stratified turbid media. *Journal of Computational Physics*, 201(2):771–797, 2004.

[9] Anurag Behera, Laura Di Sieno, Antonio Pifferi, Fabrizio Martelli, and Alberto Dalla Mora. Study of optimal measurement conditions for time-domain diffuse optics systems. In *Biophotonics: Photonic Solutions for Better Health Care VI*, volume 10685, pages 156–163. SPIE, 2018.

[10] Janelle E Bender, Karthik Vishwanath, Laura K Moore, J Quincy Brown, Vivide Chang, Gregory M Palmer, and Nirmala Ramanujam. A robust monte carlo model for the extraction of biological absorption and scattering in vivo. *IEEE transactions on biomedical engineering*, 56(4):960–968, 2008.

[11] Jeff Bezanson, Alan Edelman, Stefan Karpinski, and Viral B Shah. Julia: A fresh approach to numerical computing. *SIAM review*, 59(1):65–98, 2017.

[12] Jeff Bezanson, Alan Edelman, Stefan Karpinski, and Viral B Shah. Julia: A fresh approach to numerical computing. *SIAM Review*, 59(1):65–98, 2017.

[13] Giles Blaney, Phillip Curtsmith, Angelo Sassaroli, Cristianne Fernandez, and Sergio Fantini. Broadband absorption spectroscopy of heterogeneous biological tissue. *Applied Optics*, 60(25):7552–7562, 2021.

[14] David A Boas, LE Campbell, and Arjun G Yodh. Scattering and imaging with diffusing temporal field correlations. *Physical review letters*, 75(9):1855, 1995.

[15] David A Boas, Sava Sakadžić, Juliette J Selb, Parisa Farzam, Maria Angela Franceschini, and Stefan A Carp. Establishing the diffuse correlation spectroscopy signal relationship with blood flow. *Neurophotonics*, 3(3):031412, 2016.

[16] Craig F Bohren and Donald R Huffman. *Absorption and scattering of light by small particles*. John Wiley & Sons, 2008.

[17] Gianluca Boso, Alberto Dalla Mora, Adriano Della Frera, and Alberto Tosi. Fast-gating of single-photon avalanche diodes with 200 ps transitions and 30 ps timing jitter. *Sensors and Actuators A: Physical*, 191:61–67, 2013.

[18] Jean-Pierre Bouchard, Israël Veilleux, Rym Jedidi, Isabelle Noiseux, Michel Fortin, and Ozzy Mermut. Reference optical phantoms for diffuse optical spectroscopy. part 1–error analysis of a time resolved transmittance characterization method. *Optics express*, 18(11):11495–11507, 2010.

[19] Sabrina Brigadoi and Robert J Cooper. How short is short? optimum source–detector distance for short-separation channels in functional near-infrared spectroscopy. *Neurophotonics*, 2(2):025005, 2015.

[20] Erin M Buckley, Ashwin B Parthasarathy, P Ellen Grant, Arjun G Yodh, and Maria Angela Franceschini. Diffuse correlation spectroscopy for measurement of cerebral blood flow: future prospects. *Neurophotonics*, 1(1):011009, 2014.

[21] SA Carp, GP Dai, David A Boas, Maria Angela Franceschini, and YR Kim. Validation of diffuse correlation spectroscopy measurements of rodent cerebral blood flow with simultaneous arterial spin labeling mri; towards mri-optical continuous cerebral metabolic monitoring. *Biomedical optics express*, 1(2):553–565, 2010.

[22] Horatio Scott Carslaw and John Conrad Jaeger. Conduction of heat in solids. *Conduction of heat in solids*, 1947.

[23] Kenneth M Case. *Linear transport theory*. Addison-Wesley Publishing Company, 1967.

[24] Moustafa T Chahine. Inverse problems in radiative transfer: Determination of atmospheric parameters. *Journal of Atmospheric Sciences*, 27(6):960–967, 1970.

[25] Malavika Chandra, Karthik Vishwanath, Greg D Fichter, Elly Liao, Scott J Hollister, and Mary-Ann Mycek. Quantitative molecular sensing in biological tissues: an approach to non-invasive optical characterization. *Optics Express*, 14(13):6157–6171, 2006.

[26] Subrahmanyan Chandrasekhar. *Radiative transfer*. Courier Corporation, 2013.

[27] Xiaojun Cheng, Hui Chen, Edbert J Sie, Francesco Marsili, and David A Boas. Development of a monte carlo-wave model to simulate time domain diffuse correlation spectroscopy measurements from first principles. *Journal of Biomedical Optics*, 27(8):083009, 2022.

[28] Xiaojun Cheng, Davide Tamborini, Stefan A Carp, Oleg Shatrovoy, Bernhard Zimmerman, Danil Tyulmankov, Andrew Siegel, Megan Blackwell, Maria Angela Franceschini, and David A Boas. Time domain diffuse correlation spectroscopy: modeling the effects of laser coherence length and instrument response function. *Optics letters*, 43(12):2756–2759, 2018.

[29] Lorenzo Colombo, Marco Pagliazzi, Sanathana Konugolu Venkata Sekar, Davide Contini, Alberto Dalla Mora, Lorenzo Spinelli, Alessandro Torricelli, Turgut Durduran, and Antonio Pifferi. Effects of the instrument response function and the gate width in time-domain diffuse correlation spectroscopy: model and validations. *Neurophotonics*, 6(3):035001, 2019.

[30] Daniele Contini, Fabrizio Martelli, and Giovanni Zaccanti. Photon migration through a turbid slab described by a model based on diffusion approximation. i. theory. *Applied optics*, 36(19):4587–4599, 1997.

[31] Robert J Cooper, Matteo Caffini, Jay Dubb, Qianqian Fang, Anna Custo, Daisuke Tsuzuki, Bruce Fischl, William Wells III, Ippeita Dan, and David A Boas. Validating atlas-guided dot: a comparison of diffuse optical tomography informed by atlas and subject-specific anatomies. *NeuroImage*, 62(3):1999–2006, 2012.

[32] Robert J Cooper, Elliott Magee, Nick Everdell, Salavat Magazov, Marta Varela, Dimitrios Airantzis, Adam P Gibson, and Jeremy C Hebden. Monstir ii: a 32-channel, multispectral, time-resolved optical tomography system for neonatal brain imaging. *Review of Scientific Instruments*, 85(5):053105, 2014.

[33] Alper Corlu, Regine Choe, Turgut Durduran, Kijoon Lee, Martin Schweiger, Simon R Arridge, Elizabeth MC Hillman, and Arjun G Yodh. Diffuse optical tomography with spectral constraints and wavelength optimization. *Applied optics*, 44(11):2082–2093, 2005.

[34] Lorenzo Cortese, Giuseppe Lo Presti, Marco Pagliazzi, Davide Contini, Alberto Dalla Mora, Hamid Dehghani, Fabio Ferri, Jonas B Fischer, Martina Giovannella, Fabrizio Martelli, et al. Recipes for diffuse correlation spectroscopy instrument design using commonly utilized hardware based on targets for signal-to-noise ratio and precision. *Biomedical Optics Express*, 12(6):3265–3281, 2021.

[35] Rinaldo Cubeddu, M Musolino, A Pifferi, Paola Taroni, and Gianluca Valentini. Time-resolved reflectance: a systematic study for application to the optical characterization of tissues. *IEEE Journal of quantum electronics*, 30(10):2421–2430, 1994.

[36] Rinaldo Cubeddu, Antonio Pifferi, Paola Taroni, Alessandro Torricelli, and Gianluca Valentini. Experimental test of theoretical models for time-resolved reflectance. *Medical physics*, 23(9):1625–1633, 1996.

[37] Anna Custo, William M Wells Iii, Alex H Barnett, Elizabeth MC Hillman, and David A Boas. Effective scattering coefficient of the cerebral spinal fluid in adult head models for diffuse optical imaging. *Applied optics*, 45(19):4747–4755, 2006.

[38] Alberto Dalla Mora, Davide Contini, Simon Arridge, Fabrizio Martelli, Alberto Tosi, Gianluca Boso, Andrea Farina, Turgut Durduran, Edoardo Martinenghi, Alessandro Torricelli, et al. Towards next-generation time-domain diffuse optics for extreme depth penetration and sensitivity. *Biomedical optics express*, 6(5):1749–1760, 2015.

[39] David T Delpy, Mark Cope, Pieter van der Zee, Simon Arridge, Susan Wray, and JS Wyatt. Estimation of optical pathlength through tissue from direct time of flight measurement. *Physics in Medicine & Biology*, 33(12):1433, 1988.

[40] Mamadou Diop, Kyle Verdecchia, Ting-Yim Lee, and Keith St Lawrence. Calibration of diffuse correlation spectroscopy with a time-resolved near-infrared technique to yield absolute cerebral blood flow measurements. *Biomedical optics express*, 2(7):2068–2081, 2011.

[41] Craig Donner and Henrik Wann Jensen. Light diffusion in multi-layered translucent materials. *ACM Transactions on Graphics (ToG)*, 24(3):1032–1039, 2005.

[42] Arlene Duncan, Judith H Meek, Matthew Clemence, Clare E Elwell, Lidia Tyszczuk, Mark Cope, and D Delpy. Optical pathlength measurements on adult head, calf and forearm and the head of the newborn infant using phase resolved optical spectroscopy. *Physics in Medicine & Biology*, 40(2):295, 1995.

[43] Turgut Durduran, Regine Choe, Wesley B Baker, and Arjun G Yodh. Diffuse optics for tissue monitoring and tomography. *Reports on progress in physics*, 73(7):076701, 2010.

[44] Turgut Durduran and Arjun G Yodh. Diffuse correlation spectroscopy for non-invasive, micro-vascular cerebral blood flow measurement. *Neuroimage*, 85:51–63, 2014.

[45] Turgut Durduran, Guoqiang Yu, Mark G Burnett, John A Detre, Joel H Greenberg, Jiongjiong Wang, Chao Zhou, and Arjun G Yodh. Diffuse optical measurement of blood flow, blood oxygenation, and metabolism in a human brain during sensorimotor cortex activation. *Optics letters*, 29(15):1766–1768, 2004.

[46] Cosimo D'Andrea, Lorenzo Spinelli, Andrea Bassi, Arianna Giusto, Davide Contini, J Swartling, Alessandro Torricelli, and Rinaldo Cubeddu. Time-resolved spectrally constrained method for the quantification of chromophore concentrations and scattering parameters in diffusing media. *Optics express*, 14(5):1888–1898, 2006.

[47] Adam T Eggebrecht, Silvina L Ferradal, Amy Robichaux-Viehoever, Mahlega S Hassanpour, Hamid Dehghani, Abraham Z Snyder, Tamara Hershey, and Joseph P Culver. Mapping distributed brain function and networks with diffuse optical tomography. *Nature photonics*, 8(6):448–454, 2014.

[48] Dirk J Faber, Maurice CG Aalders, Egbert G Mik, Brett A Hooper, Martin JC van Gemert, and Ton G van Leeuwen. Oxygen saturation-dependent absorption and scattering of blood. *Physical review letters*, 93(2):028102, 2004.

[49] Qianqian Fang. Mesh-based monte carlo method using fast ray-tracing in plücker coordinates. *Biomedical optics express*, 1(1):165–175, 2010.

[50] Qianqian Fang and David A Boas. Monte carlo simulation of photon migration in 3d turbid media accelerated by graphics processing units. *Optics express*, 17(22):20178–20190, 2009.

[51] Thomas J Farrell, Michael S Patterson, and Matthias Essenpreis. Influence of layered tissue architecture on estimates of tissue optical properties obtained from spatially resolved diffuse reflectometry. *Applied optics*, 37(10):1958–1972, 1998.

[52] Thomas J Farrell, Michael S Patterson, and Brian Wilson. A diffusion theory model of spatially resolved, steady-state diffuse reflectance for the noninvasive determination of tissue optical properties in vivo. *Medical physics*, 19(4):879–888, 1992.

[53] Marco Ferrari, Leonardo Mottola, and Valentina Quaresima. Principles, techniques, and limitations of near infrared spectroscopy. *Canadian journal of applied physiology*, 29(4):463–487, 2004.

[54] Stephen T Flock, Steven L Jacques, Brian C Wilson, Willem M Star, and Martin JC van Gemert. Optical properties of intralipid: a phantom medium for light propagation studies. *Lasers in surgery and medicine*, 12(5):510–519, 1992.

[55] Maria Angela Franceschini, Sergio Fantini, L Adelina Paunescu, John S Maier, and Enrico Gratton. Influence of a superficial layer in the quantitative spectroscopic study of strongly scattering media. *Applied optics*, 37(31):7447–7458, 1998.

[56] Yuich Fukui, Yusaku Ajichi, and Eiji Okada. Monte carlo prediction of near-infrared light propagation in realistic adult and neonatal head models. *Applied optics*, 42(16):2881–2887, 2003.

[57] Louis Gagnon, Michèle Desjardins, Julien Jehanne-Lacasse, Louis Bherer, and Frédéric Lesage. Investigation of diffuse correlation spectroscopy in multi-layered media including the human head. *Optics express*, 16(20):15514–15530, 2008.

[58] Héctor A García, Demián A Vera, María V Waks Serra, Guido R Baez, Daniela I Iriarte, and Juan A Pomarico. Theoretical investigation of photon partial pathlengths in multilayered turbid media. *Biomedical Optics Express*, 13(4):2516–2529, 2022.

[59] Héctor Alfredo García, Daniela Ines Iriarte, Juan Antonio Pomarico, D Grosenick, and R Macdonald. Retrieval of the optical properties of a semiinfinite compartment in a layered scattering medium by single-distance, time-resolved diffuse reflectance measurements. *Journal of Quantitative Spectroscopy and Radiative Transfer*, 189:66–74, 2017.

[60] Simeon Geiger, Dominik Reitzle, André Liemert, and Alwin Kienle. Determination of the optical properties of three-layered turbid media in the time domain using the p 3 approximation. *OSA Continuum*, 2(6):1889–1899, 2019.

[61] Freija Geldof, Behdad Dashtbozorg, Benno HW Hendriks, Henricus JCM Sterenborg, and Theo JM Ruers. Layer thickness prediction and tissue classification in two-layered tissue structures using diffuse reflectance spectroscopy. *Scientific Reports*, 12(1):1–12, 2022.

[62] Martina Giovannella, Davide Contini, Marco Pagliazzi, Antonio Pifferi, Lorenzo Spinelli, Rainer Erdmann, Roger Donat, Ignacio Rocchetti, Matthias Rehberger, Niels König, et al. Babylux device: a diffuse optical system integrating diffuse correlation spectroscopy and time-resolved near-infrared spectroscopy for the neuromonitoring of the premature newborn brain. *Neurophotonics*, 6(2):025007, 2019.

[63] Nicholas M Gregg, Brian R White, Benjamin W Zeff, Andrew J Berger, and Joseph P Culver. Brain specificity of diffuse optical imaging: improvements from superficial signal regression and tomography. *Frontiers in neuroenergetics*, 2:14, 2010.

[64] Zhixiong Guo, Slew Kan Wan, Kyunghan Kim, and Chakravarthi Kosaraju. Comparing diffusion approximation with radiation transfer analysis for light transport in tissues. *Optical review*, 10(5):415–421, 2003.

[65] Bertan Hallacoglu, Angelo Sassaroli, and Sergio Fantini. Optical characterization of two-layered turbid media for non-invasive, absolute oximetry in cerebral and extracerebral tissue. *PloS one*, 8(5):e64095, 2013.

[66] John Harrison. Fast and accurate bessel function computation. In *2009 19th IEEE Symposium on Computer Arithmetic*, pages 104–113. IEEE, 2009.

[67] Carole K Hayakawa, Lisa Malenfant, Janaka Ranasinghesagara, David J Cuccia, Jerome Spanier, and Vasan Venugopalan. Mccl: an open-source software application for monte carlo simulations of radiative transport. *Journal of biomedical optics*, 27(8):083005, 2022.

[68] Michael Helton. Lightpropagation.jl. https://github.com/heltonmc/LightPropagation.jl, 2021.

[69] Michael Helton, Carter McMaster, Mary-Ann Mycek, and Karthik Vishwanath. Calibration free, time-resolved diffuse optical spectroscopy using combined monte-carlo and diffusion theory. In *Biomedical Applications of Light Scattering XI*, volume 11657, pages 15–20. SPIE, 2021.

[70] Michael Helton, Mary-Ann Mycek, and Karthik Vishwanath. Direct estimation of the reduced scattering coefficient from experimentally measured time-resolved reflectance via monte carlo based lookup tables. *Biomedical Optics Express*, 11(8):4366–4378, 2020.

[71] Michael Helton, Mary-Ann Mycek, and Karthik Vishwanath. Directly extracting the optical transport coefficients of a turbid medium via time-resolved diffuse reflectance: a monte carlo study. In *Biomedical Applications of Light Scattering X*, volume 11253, pages 11–16. SPIE, 2020.

[72] Michael Helton, Mary-Ann Mycek, and Karthik Vishwanath. Reconstruction of optical coefficients in turbid media using time-resolved reflectance and calibration-free instrument response functions. *Biomedical Optics Express*, 13(3):1595–1608, 2022.

[73] Michael Helton, Suraj Rajasekhar, Samantha Zerafa, Karthik Vishwanath, and Mary-Ann Mycek. Reconstruction of flow coefficients in layered media using continuous-wave vs. time-domain diffuse correlation spectroscopy. In *Optical Tomography and Spectroscopy*, pages OW4D–6. Optica Publishing Group, 2022.

[74] Michael Helton, Suraj Rajasekhar, Samantha Zerafa, Karthik Vishwanath, and Mary-Ann Mycek. Numerical approach to quantify depth-dependent blood flow changes in real-time using the diffusion equation with continuous-wave and time-domain diffuse correlation spectroscopy. *Biomed. Opt. Express*, 14(1):367–384, Jan 2023.

[75] Michael Helton, Samantha Zerafa, Karthik Vishwanath, and Mary-Ann Mycek. Efficient computation of the steady-state and time-domain solutions of the photon diffusion equation in layered turbid media. *Scientific Reports*, 12(1):1–14, 2022.

[76] Michael Helton, Samantha Zerafa, Karthik Vishwanath, and Mary-Ann Mycek. Robust numerical simulation of the diffusion equation in layered media in the steady-state and time-domains. In *Optics and the Brain*, pages JM3A–21. Optica Publishing Group, 2022.

[77] HGE Hentschel and Itamar Procaccia. Relative diffusion in turbulent media: the fractal dimension of clouds. *Physical Review A*, 29(3):1461, 1984.

[78] Brett H Hokr and Joel N Bixler. Machine learning estimation of tissue optical properties. *Scientific Reports*, 11(1):1–7, 2021.

[79] Daniel Irwin, Lixin Dong, Yu Shang, Ran Cheng, Mahesh Kudrimoti, Scott D Stevens, and Guoqiang Yu. Influences of tissue absorption and scattering on diffuse correlation spectroscopy blood flow measurements. *Biomedical optics express*, 2(7):1969–1985, 2011.

[80] Steven L Jacques. Optical properties of biological tissues: a review. *Physics in Medicine & Biology*, 58(11):R37, 2013.

[81] Franck Jaillon, Sergey E Skipetrov, Jun Li, Gregor Dietsche, Georg Maret, and Thomas Gisler. Diffusing-wave spectroscopy from head-like tissue phantoms: influence of a non-scattering layer. *Optics express*, 14(22):10181–10194, 2006.

[82] Henrik Wann Jensen, Stephen R Marschner, Marc Levoy, and Pat Hanrahan. A practical model for subsurface light transport. In *Proceedings of the 28th annual conference on Computer graphics and interactive techniques*, pages 511–518, 2001.

[83] Alwin Kienle and Thomas Glanzmann. In vivo determination of the optical properties of muscle with time-resolved reflectance using a layered model. *Physics in Medicine & Biology*, 44(11):2689, 1999.

[84] Alwin Kienle, Thomas Glanzmann, Georges Wagnieres, and Hubert van den Bergh. Investigation of two-layered turbid media with time-resolved reflectance. *Applied optics*, 37(28):6852–6862, 1998.

[85] Alwin Kienle and Michael S. Patterson. Improved solutions of the steady-state and the time-resolved diffusion equations for reflectance from a semi-infinite turbid medium. *JOSA A*, 14(1):246–254, 1997.

[86] Alwin Kienle, Michael S Patterson, Nora Dögnitz, Roland Bays, Georges Wagnieres, and Hubert van Den Bergh. Noninvasive determination of the optical properties of two-layered turbid media. *Applied optics*, 37(4):779–791, 1998.

[87] Boris Korzh, Qing-Yuan Zhao, Jason P Allmaras, Simone Frasca, Travis M Autry, Eric A Bersin, Andrew D Beyer, Ryan M Briggs, Bruce Bumble, Marco Colangelo, et al. Demonstration of sub-3 ps temporal resolution with a superconducting nanowire single-photon detector. *Nature Photonics*, 14(4):250–255, 2020.

[88] William J Koshak, Richard J Solakiewicz, Dieudonne D Phanord, and Richard J Blakeslee. Diffusion model for lightning radiative transfer. *Journal of Geophysical Research: Atmospheres*, 99(D7):14361–14371, 1994.

[89] Kristopher L Kuhlman. Review of inverse laplace transform algorithms for laplace-space numerical approaches. *Numerical Algorithms*, 63(2):339–355, 2013.

[90] Seung Yup Lee, William R Lloyd, Malavika Chandra, Robert H Wilson, Barbara McKenna, Diane Simeone, James Scheiman, and Mary-Ann Mycek. Characterizing human pancreatic cancer precursor using quantitative tissue optical spectroscopy. *Biomedical Optics Express*, 4(12):2828–2834, 2013.

[91] Seung Yup Lee, Julia M Pakela, Taylor L Hedrick, Karthik Vishwanath, Michael C Helton, Yooree Chung, Noah J Kolodziejski, Christopher J Stapels, Daniel R McAdams, Daniel E Fernandez, et al. Novel diffuse optics system for continuous tissue viability monitoring: extended recovery in vivo testing in a porcine flap model. In *Advanced Biomedical and Clinical Diagnostic and Surgical Guidance Systems XV*, volume 10054, pages 148–155. SPIE, 2017.

[92] Seung Yup Lee, Julia M Pakela, Michael C Helton, Karthik Vishwanath, Yooree G Chung, Noah J Kolodziejski, Christopher J Stapels, Daniel R McAdams, Daniel E Fernandez, James F Christian, Jameson O'Reilly, Dana Farkas, Brent B Ward, Stephen E Feinberg, and Mary-Ann Mycek. Compact dual-mode diffuse optical system for blood perfusion monitoring in a porcine model of microvascular tissue flaps. *Journal of Biomedical Optics*, 22(12):121609, 2017.

[93] Jacqueline Lenoble. *Atmospheric radiative transfer*. A. Deepak Pub., 1993.

[94] Changqing Li, Stephen R Grobmyer, Lin Chen, Qizhi Zhang, Laurie L Fajardo, and Huabei Jiang. Multispectral diffuse optical tomography with absorption and scattering spectral constraints. *Applied optics*, 46(34):8229–8236, 2007.

[95] Jun Li, Gregor Dietsche, Diana Iftime, Sergey E Skipetrov, Georg Maret, Thomas Elbert, Brigitte Rockstroh, and Thomas Gisler. Noninvasive detection of functional brain activity with near-infrared diffusing-wave spectroscopy. *Journal of biomedical optics*, 10(4):044002, 2005.

[96] Jun Li, Lina Qiu, Chien-Sing Poon, and Ulas Sunar. Analytical models for time-domain diffuse correlation spectroscopy for multi-layer and heterogeneous turbid media. *Biomedical optics express*, 8(12):5518–5532, 2017.

[97] A. Liebert, H. Wabnitz, D. Grosenick, and R. Macdonald. Liebert, adam, et al. "fiber dispersion in time domain measurements compromising the accuracy of determination of optical properties of strongly scattering media. *Biomedical Optics Express*, 8(3):512–516, 2003.

[98] Adam Liebert, Heidrun Wabnitz, and Clemens Elster. Determination of absorption changes from moments of distributions of times of flight of photons: optimization of measurement conditions for a two-layered tissue model. *Journal of Biomedical Optics*, 17(5):057005, 2012.

[99] Adam Liebert, Heidrun Wabnitz, Dirk Grosenick, Michael Möller, Rainer Macdonald, and Herbert Rinneberg. Evaluation of optical properties of highly scattering media by moments of distributions of times of flight of photons. *Applied optics*, 42(28):5785–5792, 2003.

[100] Adam Liebert, Heidrun Wabnitz, Jens Steinbrink, Hellmuth Obrig, Michael Möller, Rainer Macdonald, Arno Villringer, and Herbert Rinneberg. Time-resolved multidistance near-infrared spectroscopy of the adult head: intracerebral and extracerebral absorption changes from moments of distribution of times of flight of photons. *Applied optics*, 43(15):3037–3047, 2004.

[101] André Liemert and Alwin Kienle. Light diffusion in a turbid cylinder. i. homogeneous case. *Optics Express*, 18(9):9456–9473, 2010.

[102] André Liemert and Alwin Kienle. Light diffusion in a turbid cylinder. ii. layered case. *Optics Express*, 18(9):9266–9279, 2010.

[103] André Liemert and Alwin Kienle. Light diffusion in n-layered turbid media: frequency and time domains. *Journal of biomedical optics*, 15(2):025002, 2010.

[104] André Liemert and Alwin Kienle. Light diffusion in n-layered turbid media: steady-state domain. *Journal of biomedical optics*, 15(2):025003, 2010.

[105] André Liemert and Alwin Kienle. Exact and efficient solution of the radiative transport equation for the semi-infinite medium. *Scientific reports*, 3(1):1–7, 2013.

[106] André Liemert and Alwin Kienle. Application of the laplace transform in time-domain optical spectroscopy and imaging. *Journal of biomedical optics*, 20(11):110502, 2015.

[107] André Liemert, Dominik Reitzle, and Alwin Kienle. Analytical solutions of the radiative transport equation for turbid and fluorescent layered media. *Scientific reports*, 7(1):1–9, 2017.

[108] Jonathan Malsan, Rajan Gurjar, David Wolf, and Karthik Vishwanath. Extracting optical properties of turbid media using radially and spectrally resolved diffuse reflectance. In *Design and Quality for Biomedical Technologies Vii*, volume 8936, pages 182–190. SPIE, 2014.

[109] Fabrizio Martelli. *Light propagation through biological tissue and other diffusive media: theory, solutions, and software*. SPIE press, 2009.

[110] Fabrizio Martelli. An abc of near infrared photon migration in tissues: the diffusive regime of propagation. *Journal of Near Infrared Spectroscopy*, 20(1):29–42, 2012.

[111] Fabrizio Martelli, Angelo Sassaroli, Samuele Del Bianco, Yukio Yamada, and Giovanni Zaccanti. Solution of the time-dependent diffusion equation for layered diffusive media by the eigenfunction method. *Physical Review E*, 67(5):056623, 2003.

[112] Fabrizio Martelli, Angelo Sassaroli, Samuele Del Bianco, and Giovanni Zaccanti. Solution of the time-dependent diffusion equation for a three-layer medium: application to study photon migration through a simplified adult head model. *Physics in Medicine & Biology*, 52(10):2827, 2007.

[113] Fabrizio Martelli, Federico Tommasi, Angelo Sassaroli, Lorenzo Fini, and Stefano Cavalieri. Verification method of monte carlo codes for transport processes with arbitrary accuracy. *Scientific reports*, 11(1):1–12, 2021.

[114] Fabrizio Martelli and Giovanni Zaccanti. Calibration of scattering and absorption properties of a liquid diffusive medium at nir wavelengths. cw method. *Optics express*, 15(2):486–500, 2007.

[115] Dibbyan Mazumder, Melissa M Wu, Nisan Ozana, Davide Tamborini, Maria Angela Franceschini, and Stefan A Carp. Optimization of time domain diffuse correlation spectroscopy parameters for measuring brain blood flow. *Neurophotonics*, 8(3):035005, 2021.

[116] M Mazurenka, A Jelzow, H Wabnitz, Davide Contini, Lorenzo Spinelli, A Pifferi, Rinaldo Cubeddu, Alberto Dalla Mora, Alberto Tosi, Franco Zappa, et al. Non-contact time-resolved diffuse reflectance imaging at null source-detector separation. *Optics Express*, 20(1):283–290, 2012.

[117] Carter McMaster, Michael Helton, Boyd Colbrunn, Mary-Ann Mycek, and Karthik Vishwanath. Time-gated diffuse reflectance to discriminate optical properties of two-layered tissue phantoms. In *Biomedical Applications of Light Scattering XII*, volume 11974, pages 69–79. SPIE, 2022.

[118] Hakan Okyay Menges and Can Ertekin. Mathematical modeling of thin layer drying of golden apples. *Journal of Food Engineering*, 77(1):119–125, 2006.

[119] Rickson C Mesquita, Steven S Schenkel, David L Minkoff, Xiangping Lu, Christopher G Favilla, Patrick M Vora, David R Busch, Malavika Chandra, Joel H Greenberg, John A Detre, and Arjun G Yodh. Influence of probe pressure on the diffuse correlation spectroscopy

blood flow signal: extra-cerebral contributions. *Biomedical optics express*, 4(7):978–994, 2013.

[120] René Michels, Florian Foschum, and Alwin Kienle. Optical properties of fat emulsions. *Optics express*, 16(8):5907–5925, 2008.

[121] Gustav Mie. Beiträge zur optik trüber medien, speziell kolloidaler metallösungen. *Annalen der physik*, 330(3):377–445, 1908.

[122] Daniel Milej, Androu Abdalmalak, Dariusz Janusek, Mamadou Diop, Adam Liebert, and Keith St Lawrence. Time-resolved subtraction method for measuring optical properties of turbid media. *Applied Optics*, 55(7):1507–1513, 2016.

[123] Michael I Mishchenko, Larry D Travis, and Andrew A Lacis. *Multiple scattering of light by particles: radiative transfer and coherent backscattering*. Cambridge University Press, 2006.

[124] Patrick Kofod Mogensen and Asbjørn Nilsen Riseth. Optim: A mathematical optimization package for Julia. *Journal of Open Source Software*, 3(24):615, 2018.

[125] Sara Mosca, Pranav Lanka, Nick Stone, Sanathana Konugolu Venkata Sekar, Pavel Matousek, Gianluca Valentini, and Antonio Pifferi. Optical characterization of porcine tissues from various organs in the 650–1100 nm range using time-domain diffuse spectroscopy. *Biomedical optics express*, 11(3):1697–1706, 2020.

[126] Judith R Mourant, Murat Canpolat, C Brocker, O Esponda-Ramos, Tamara M Johnson, A Matanock, K Stetter, and James P Freyer. Light scattering from cells: the contribution of the nucleus and the effects of proliferative status. *Journal of biomedical optics*, 5(2):131–137, 2000.

[127] Judith R Mourant, James P Freyer, Andreas H Hielscher, Angelia A Eick, Dan Shen, and Tamara M Johnson. Mechanisms of light scattering from biological cells relevant to noninvasive optical-tissue diagnostics. *Applied optics*, 37(16):3586–3593, 1998.

[128] Judith R Mourant, Tamika Fuselier, James Boyer, Tamara M Johnson, and Irving J Bigio. Predictions and measurements of scattering and absorption over broad wavelength ranges in tissue phantoms. *Applied optics*, 36(4):949–957, 1997.

[129] Meghdoot Mozumder and Tanja Tarvainen. Time-domain diffuse optical tomography utilizing truncated fourier series approximation. *JOSA A*, 37(2):182–191, 2020.

[130] Goro Nishimura and Mamoru Tamura. Simple peak shift analysis of time-of-flight data with a slow instrumental response function. *Journal of Biomedical Optics*, 10(1):014016, 2005.

[131] Vasilis Ntziachristos and Britton Chance. Accuracy limits in the determination of absolute optical properties using time-resolved nir spectroscopy. *Medical physics*, 28(6):1115–1124, 2001.

[132] Vasilis Ntziachristos, XuHui Ma, AG Yodh, and Britton Chance. Multichannel photon counting instrument for spatially resolved near infrared spectroscopy. *Review of Scientific Instruments*, 70(1):193–201, 1999.

[133] Eiji Okada and David T Delpy. Near-infrared light propagation in an adult head model. ii. effect of superficial tissue thickness on the sensitivity of the near-infrared spectroscopy signal. *Applied optics*, 42(16):2915–2921, 2003.

[134] M Pagliazzi, S Konugolu Venkata Sekar, L Colombo, E Martinenghi, J Minnema, R Erdmann, D Contini, A Dalla Mora, A Torricelli, A Pifferi, and Turgut Durduran. Time domain diffuse correlation spectroscopy with a high coherence pulsed source: in vivo and phantom results. *Biomedical optics express*, 8(11):5311–5325, 2017.

[135] Julia M Pakela, Taylor L Hedrick, Seung Yup Lee, Karthik Vishwanath, Sara Zanfardino, Yooree G Chung, Michael C Helton, Noah J Kolodziejski, Christopher J Stapels, Daniel R McAdams, et al. Design verification of a compact system for detecting tissue perfusion using bimodal diffuse optical technologies. In *Optical Diagnostics and Sensing XVII: Toward Point-of-Care Diagnostics*, volume 10072, pages 226–232. SPIE, 2017.

[136] Julia M Pakela, Seung Yup Lee, Taylor L Hedrick, Karthik Vishwanath, Michael C Helton, Yooree G Chung, Noah J Kolodziejski, Christopher J Staples, Daniel R McAdams, Daniel E Fernandez, et al. In vivo preclinical verification of a multimodal diffuse reflectance and correlation spectroscopy system for sensing tissue perfusion. In *Optical Diagnostics and Sensing XVII: Toward Point-of-Care Diagnostics*, volume 10072, page 144. SPIE, 2017.

[137] Michael S Patterson, Britton Chance, and Brian C Wilson. Time resolved reflectance and transmittance for the noninvasive measurement of tissue optical properties. *Applied optics*, 28(12):2331–2336, 1989.

[138] Qiyu Peng, Woon-Seng Choong, and W William Moses. Evaluation of the timing properties of a high quantum efficiency photomultiplier tube. *IEEE transactions on nuclear science*, 60(5):3212–3219, 2013.

[139] Johan Philip and Kjell Carlsson. Theoretical investigation of the signal-to-noise ratio in fluorescence lifetime imaging. *JOSA A*, 20(2):368–379, 2003.

[140] Antonio Pifferi, Davide Contini, Alberto Dalla Mora, Andrea Farina, Lorenzo Spinelli, and Alessandro Torricelli. New frontiers in time-domain diffuse optics, a review. *Journal of biomedical optics*, 21(9):091310, 2016.

[141] Antonio Pifferi, Alessandro Torricelli, Andrea Bassi, Paola Taroni, Rinaldo Cubeddu, Heidrun Wabnitz, Dirk Grosenick, Michael Möller, Rainer Macdonald, Johannes Swartling, et al. Performance assessment of photon migration instruments: the medphot protocol. *Applied optics*, 44(11):2104–2114, 2005.

[142] Antonio Pifferi, Alessandro Torricelli, Paola Taroni, Daniela Comelli, Andrea Bassi, and Rinaldo Cubeddu. Fully automated time domain spectrometer for the absorption and scattering characterization of diffusive media. *Review of scientific instruments*, 78(5):053103, 2007.

[143] Ileana Pirovano, Rebecca Re, Alessia Candeo, Davide Contini, Alessandro Torricelli, and Lorenzo Spinelli. Instrument response function acquisition in reflectance geometry for time-resolved diffuse optical measurements. *Biomedical Optics Express*, 11(1):240–250, 2020.

[144] Agathe Puszka, Laura Di Sieno, Alberto Dalla Mora, Antonio Pifferi, Davide Contini, Anne Planat-Chrétien, Anne Koenig, Gianluca Boso, Alberto Tosi, Lionel Hervé, et al. Spatial resolution in depth for time-resolved diffuse optical tomography using short source-detector separations. *Biomedical optics express*, 6(1):1–10, 2015.

[145] Michael Raju and Sujatha Narayanan Unni. Concentration-dependent correlated scattering properties of intralipid 20% dilutions. *Applied Optics*, 56(4):1157–1166, 2017.

[146] Rebecca Re, Davide Contini, Lucia Zucchelli, Alessandro Torricelli, and Lorenzo Spinelli. Effect of a thin superficial layer on the estimate of hemodynamic changes in a two-layer medium by time domain nirs. *Biomedical Optics Express*, 7(2):264–278, 2016.

[147] Rolf B Saager and Andrew J Berger. Measurement of layer-like hemodynamic trends in scalp and cortex: implications for physiological baseline suppression in functional near-infrared spectroscopy. *Journal of biomedical optics*, 13(3):034017, 2008.

[148] Saeed Samaei, Piotr Sawosz, Michał Kacprzak, Żanna Pastuszak, Dawid Borycki, and Adam Liebert. Time-domain diffuse correlation spectroscopy (td-dcs) for noninvasive, depth-dependent blood flow quantification in human tissue in vivo. *Scientific reports*, 11(1):1–10, 2021.

[149] Julia L Sandell and Timothy C Zhu. A review of in-vivo optical properties of human tissues and its impact on pdt. *Journal of biophotonics*, 4(11-12):773–787, 2011.

[150] Sanathana Konugolu Venkata Sekar, Alberto Dalla Mora, Ilaria Bargigia, Edoardo Martinenghi, Claus Lindner, Parisa Farzam, Marco Pagliazzi, Turgut Durduran, Paola Taroni, Antonio Pifferi, et al. Broadband (600–1350 nm) time-resolved diffuse optical spectrometer for clinical use. *IEEE Journal of Selected Topics in Quantum Electronics*, 22(3):406–414, 2015.

[151] Juliette Selb, Kuan-Cheng Wu, Pei-Yi Ivy Lin, Jason Sutin, Parisa Farzam, Sophia Bechek, Apeksha Shenoy, Aman B Patel, David A Boas, Maria Angela Franceschini, and Eric S Rosenthal. Prolonged monitoring of cerebral blood flow and autoregulation with diffuse correlation spectroscopy in neurocritical care patients. *Neurophotonics*, 5(4):045005, 2018.

[152] Juliette J Selb, David A Boas, Suk-Tak Chan, Karleyton C Evans, Erin M Buckley, and Stefan A Carp. Sensitivity of near-infrared spectroscopy and diffuse correlation spectroscopy to brain hemodynamics: simulations and experimental findings during hypercapnia. *Neurophotonics*, 1(1):015005, 2014.

[153] Juliette J Selb, Tyler M Ogden, Jay Dubb, Qianqian Fang, and David A Boas. Comparison of a layered slab and an atlas head model for monte carlo fitting of time-domain near-infrared spectroscopy data of the adult head. *Journal of biomedical optics*, 19(1):016010, 2014.

[154] Juliette J Selb, Jonathan J Stott, Maria Angela Franceschini, A Gregory Sorensen, and David A Boas. Improved sensitivity to cerebral hemodynamics during brain activation with a time-gated optical system: analytical model and experimental validation. *Journal of biomedical optics*, 10(1):011013, 2005.

[155] Zhenqi Shi and Carl A Anderson. Pharmaceutical applications of separation of absorption and scattering in near-infrared spectroscopy (nirs). *Journal of pharmaceutical sciences*, 99(12):4766–4783, 2010.

[156] Curt Da Silva and Felix Herrmann. A unified 2d/3d large-scale software environment for nonlinear inverse problems. *ACM Transactions on Mathematical Software (TOMS)*, 45(1):1–35, 2019.

[157] Lorenzo Spinelli, Marcin Botwicz, Norbert Zolek, Michal Kacprzak, Daniel Milej, Piotr Sawosz, Adam Liebert, U Weigel, Turgut Durduran, Florian Foschum, et al. Determination of reference values for optical properties of liquid phantoms based on intralipid and india ink. *Biomedical optics express*, 5(7):2037–2053, 2014.

[158] Lorenzo Spinelli, Fabrizio Martelli, Andrea Farina, Antonio Pifferi, Alessandro Torricelli, Rinaldo Cubeddu, and Giovanni Zaccanti. Calibration of scattering and absorption properties of a liquid diffusive medium at nir wavelengths. time-resolved method. *Optics Express*, 15(11):6589–6604, 2007.

[159] Subhadra Srinivasan, Brian W Pogue, Shudong Jiang, Hamid Dehghani, Christine Kogel, Sandra Soho, Jennifer J Gibson, Tor D Tosteson, Steven P Poplack, and Keith D Paulsen. In vivo hemoglobin and water concentrations, oxygen saturation, and scattering estimates from near-infrared breast tomography using spectral reconstruction1. *Academic radiology*, 13(2):195–202, 2006.

[160] Jason Sutin, Bernhard Zimmerman, Danil Tyulmankov, Davide Tamborini, Kuan Cheng Wu, Juliette Selb, Angelo Gulinatti, Ivan Rech, Alberto Tosi, David A Boas, and Maria Angela Franceschini. Time-domain diffuse correlation spectroscopy. *Optica*, 3(9):1006–1013, 2016.

[161] Davide Tamborini, Kimberly A Stephens, Melissa M Wu, Parya Farzam, Andrew M Siegel, Oleg Shatrovoy, Megan Blackwell, David A Boas, Stefan A Carp, and Maria Angela Franceschini. Portable system for time-domain diffuse correlation spectroscopy. *IEEE Transactions on Biomedical Engineering*, 66(11):3014–3025, 2019.

[162] Gary E Thomas and Knut Stamnes. *Radiative transfer in the atmosphere and ocean*. Cambridge University Press, 2002.

[163] Alessandro Torricelli, Davide Contini, Antonio Pifferi, Matteo Caffini, Rebecca Re, Lucia Zucchelli, and Lorenzo Spinelli. Time domain functional nirs imaging for human brain mapping. *Neuroimage*, 85:28–50, 2014.

[164] Alessandro Torricelli, Antonio Pifferi, Lorenzo Spinelli, Rinaldo Cubeddu, Fabrizio Martelli, Samuele Del Bianco, and Giovanni Zaccanti. Time-resolved reflectance at null

source-detector separation: improving contrast and resolution in diffuse optical imaging. *Physical review letters*, 95(7):078101, 2005.

[165] Lloyd N Trefethen and JAC Weideman. The exponentially convergent trapezoidal rule. *siam REVIEW*, 56(3):385–458, 2014.

[166] Jean-Michel Tualle, Jérôme Prat, Eric Tinet, and Sigrid Avrillier. Real-space green's function calculation for the solution of the diffusion equation in stratified turbid media. *JOSA A*, 17(11):2046–2055, 2000.

[167] Valery V Tuchin et al. *Tissue optics*. Society of Photo-Optical Instrumentation Engineers (SPIE) Bellingham, WA, USA, 2015.

[168] Kyle Verdecchia, Mamadou Diop, Albert Lee, Laura B Morrison, Ting-Yim Lee, and Keith St Lawrence. Assessment of a multi-layered diffuse correlation spectroscopy method for monitoring cerebral blood flow in adults. *Biomedical optics express*, 7(9):3659–3674, 2016.

[169] Karthik Vishwanath, Kevin Chang, Daniel Klein, Yu Feng Deng, Vivide Chang, Janelle E Phelps, and Nimmi Ramanujam. Portable, fiber-based, diffuse reflection spectroscopy (drs) systems for estimating tissue optical properties. *Applied spectroscopy*, 65(2):206–215, 2011.

[170] Karthik Vishwanath and Mary-Ann Mycek. Time-resolved photon migration in bi-layered tissue models. *Optics Express*, 13(19):7466–7482, 2005.

[171] Karthik Vishwanath, Brian Pogue, and Mary-Ann Mycek. Quantitative fluorescence lifetime spectroscopy in turbid media: comparison of theoretical, experimental and computational methods. *Physics in Medicine & Biology*, 47(18):3387, 2002.

[172] Karthik Vishwanath and Sara Zanfardino. Diffuse correlation spectroscopy at short source-detector separations: Simulations, experiments and theoretical modeling. *Applied Sciences*, 9(15):3047, 2019.

[173] Heidrun Wabnitz, Davide Contini, Lorenzo Spinelli, Alessandro Torricelli, and Adam Liebert. Depth-selective data analysis for time-domain fnirs: moments vs. time windows. *Biomedical Optics Express*, 11(8):4224–4243, 2020.

[174] Heidrun Wabnitz, Dieter R Taubert, Mikhail Mazurenka, Oliver Steinkellner, Alexander Jelzow, Rainer Macdonald, Daniel Milej, Piotr Sawosz, Michał Kacprzak, Adam Liebert, et al. Performance assessment of time-domain optical brain imagers, part 1: basic instrumental performance protocol. *Journal of biomedical optics*, 19(8):086010, 2014.

[175] Lihong V Wang and Hsin-i Wu. *Biomedical optics: principles and imaging*. John Wiley & Sons, 2012.

[176] XC Wang and SM Wang. Light transport model in an-layered mismatched tissue. *Waves in Random and Complex Media*, 16(2):121–135, 2006.

[177] J Weideman and L Trefethen. Parabolic and hyperbolic contours for computing the bromwich integral. *Mathematics of Computation*, 76(259):1341–1356, 2007.

[178] Gerald Wilemski and Marshall Fixman. Diffusion-controlled intrachain reactions of polymers. i theory. *The Journal of Chemical Physics*, 60(3):866–877, 1974.

[179] Maeve Willen, Michael Helton, Samantha A Zerafa, Alisha B Diggs, James R Young, Susan V Brooks, Lisa M Larkin, and Mary-Ann Mycek. Non-invasive label-free assessment of contraction induced damage to skeletal muscle structure using second harmonic generation (shg) microscopy. In *Imaging, Manipulation, and Analysis of Biomolecules, Cells, and Tissues XIX*, volume 11647, page 1164704. SPIE, 2021.

[180] Brian C Wilson, Eva M Sevick, Michael S Patterson, and Britton Chance. Time-dependent optical spectroscopy and imaging for biomedical applications. *Proceedings of the IEEE*, 80(6):918–930, 1992.

[181] Robert H Wilson, Karthik Vishwanath, and Mary-Ann Mycek. Optical methods for quantitative and label-free sensing in living human tissues: principles, techniques, and applications. *Advances in Physics: X*, 1(4):523–543, 2016.

[182] Stanislaw Wojtkiewicz, Anna Gerega, Marta Zanoletti, Aleh Sudakou, Davide Contini, Adam Liebert, Turgut Durduran, and Hamid Dehghani. Self-calibrating time-resolved near infrared spectroscopy. *Biomedical optics express*, 10(5):2657–2669, 2019.

[183] Stanislaw Wojtkiewicz and Adam Liebert. Parallel, multi-purpose monte carlo code for simulation of light propagation in segmented tissues. *Biocybernetics and Biomedical Engineering*, 41(4):1303–1321, 2021.

[184] Melissa M Wu, Suk-Tak Chan, Dibbyan Mazumder, Davide Tamborini, Kimberly A Stephens, Bin Deng, Parya Farzam, Joyce Yawei Chu, Maria Angela Franceschini, Jason Zhensheng Qu, et al. Improved accuracy of cerebral blood flow quantification in the presence of systemic physiology cross-talk using multi-layer monte carlo modeling. *Neurophotonics*, 8(1):015001, 2021.

[185] Melissa M Wu, Katherine Perdue, Suk-Tak Chan, Kimberly A Stephens, Bin Deng, Maria Angela Franceschini, and Stefan A Carp. Complete head cerebral sensitivity mapping for diffuse correlation spectroscopy using subject-specific magnetic resonance imaging models. *Biomedical Optics Express*, 13(3):1131–1151, 2022.

[186] Yukio Yamada, Hiroaki Suzuki, and Yutaka Yamashita. Time-domain near-infrared spectroscopy and imaging: A review. *Applied Sciences*, 9(6):1127, 2019.

[187] Shijie Yan, Steven L Jacques, Jessica C Ramella-Roman, and Qianqian Fang. Graphics-processing-unit-accelerated monte carlo simulation of polarized light in complex three-dimensional media. *Journal of Biomedical Optics*, 27(8):083015, 2022.

[188] Tanner Young-Schultz, Stephen Brown, Lothar Lilge, and Vaughn Betz. Fullmontecuda: a fast, flexible, and accurate gpu-accelerated monte carlo simulator for light propagation in turbid media. *Biomedical optics express*, 10(9):4711–4726, 2019.

[189] Hongting Zhao, Eashani Sathialingam, and Erin M Buckley. Accuracy of diffuse correlation spectroscopy measurements of cerebral blood flow when using a three-layer analytical model. *Biomedical Optics Express*, 12(11):7149–7161, 2021.

[190] Chao Zhou, Guoqiang Yu, Daisuke Furuya, Joel H Greenberg, Arjun G Yodh, and Turgut Durduran. Diffuse optical correlation tomography of cerebral blood flow during cortical spreading depression in rat brain. *Optics express*, 14(3):1125–1144, 2006.

[191] Caigang Zhu and Quan Liu. Review of monte carlo modeling of light transport in tissues. *Journal of biomedical optics*, 18(5):050902, 2013.